Improvement of Image Quality of Transcranial Doppler Ultrasound

by

Shreyank GUPTA

THESIS PRESENTED TO ÉCOLE DE TECHNOLOGIE SUPÉRIEURE
IN PARTIAL FULFILLMENT FOR THE DEGREE OF
DOCTOR OF PHILOSOPHY
Ph.D.

MONTREAL, APRIL 30, 2021

ÉCOLE DE TECHNOLOGIE SUPÉRIEURE
UNIVERSITÉ DU QUÉBEC

BOARD OF EXAMINERS

THIS THESIS HAS BEEN EVALUATED

BY THE FOLLOWING BOARD OF EXAMINERS

Mr. Pierre Belanger, Thesis Supervisor
Department of Mechanical Engineering, École de Technologie Supérieure

Mrs. Catherine Laporte, Co-Supervisor
Department of Electrical Engineering, École de Technologie Supérieure

Mr. Rachid Aissaoui, President of the Board of Examiners
Department of Systems Engineering, École de Technologie Supérieure

Mr. Jean-Marc Lina, Member of the Jury
Department of Electrical Engineering, École de Technologie Supérieure

Mr. Jean Provost, External Independent Examiner
Department of Engineering Physics, École Polytechnique de Montréal

Mr. Francis Bernard, External Examiner
Department of Medicine, Université de Montréal

Mr. Guillaume Haïat, External Examiner
Laboratoire MSME, CNRS UMR 8208, Univ Paris Est Creteil, Univ Gustave Eiffel, F-94010 Creteil, France

THIS THESIS WAS PRESENTED AND DEFENDED

IN THE PRESENCE OF A BOARD OF EXAMINERS AND THE PUBLIC

ON APRIL 14, 2021

AT ÉCOLE DE TECHNOLOGIE SUPÉRIEURE

FOREWORD

This Ph.D. thesis was supervised by Professor Pierre Belanger and co-supervised by Professor Catherine Laporte, and it was completed between 2016 and 2020 at Ecole de Technologie Supérieure and Centre de recherche l'Hôpital du Sacré-Coeur. The original motivation behind this research was my desire to develop better technologies in the field of medical ultrasound. I have spent some beautiful time at the Centre de recherche du Sacré-Coeur where I was exposed to a multi-disciplinary research environment that gave me a broader perspective regarding medical technologies. In truth, I could not have accomplished my current success without a strong support base. First and foremost were my parents, and my wife who supported me with love and understanding. The second thing I should mention is that my professors never missed a single weekly meeting to see the progress of my work, which is quite commendable. Therefore, thank you from the bottom of my heart for spending your valuable time.

ACKNOWLEDGEMENTS

Firstly, I would like to extend my sincere gratitude to my advisors Prof. Pierre Belanger and Prof. Catherine Laporte for their continuous support of my Ph.D study and related research, for their patience, motivation, and immense knowledge. I could not imagine having a better advisor for my Doctoral studies. Their guidance helped me in all phases of research and writing of this thesis.

I am grateful to my fellow lab mates for inspiring discussions and feedback during my Ph.D work, for all the fun we had in the last five years. I would also like to express my gratitude to my friends back in Canada, who were always supportive and kept me motivated no matter what.

Last but not least, I wish to thank my family: my parents and my wife for being supportive emotionally throughout the writing process of this thesis and my life in general.

I am grateful for the grant from NSERC-CREATE program for conducting this research in collaboration with Centre de recherche l'Hôpital du Sacré-Coeur de Montréal and École de technologie supérieure.

Amélioration de la qualité d’image de l’échographie Doppler transcrânienne

Shreyank GUPTA

RÉSUMÉ

L’échographie Doppler transcrânienne (TCD) est une méthode échographique qui mesure la vitesse du flux sanguin (FV) des vaisseaux cérébraux. L’utilisation de l’échographie TCD est très intéressante en raison de sa nature non invasive et de sa portabilité. Bien que le TCD soit recommandé dans les cliniques, son utilisation est entravée dans des cas comme le vasospasme puisque le calcul du débit sanguin est requis. Le calcul du débit sanguin nécessite une mesure précise du diamètre du vaisseau sanguin, et il ne peut être calculé que lorsque la qualité de l’image est bonne. Le problème avec le TCD réside dans la faible énergie ultrasonore qui pénètre à l’intérieur du cerveau, ce qui conduit à un faible rapport signal / bruit. Cela est dû à plusieurs effets, notamment l’aberration de phase, les variations de la vitesse du son dans le crâne, la diffusion, la discordance d’impédance acoustique et l’absorption du milieu à trois couches. Cette thèse cherche à pallier ces limitations dans un premier temps à travers le développement d’un modèle analytique qui étudie l’effet des pertes par transmission du aux variations impédance acoustique. Ce modèle calcule le coefficient de transmission dépendant de la fréquence pour une couche de peau et une épaisseur osseuse données. Cette approche a été validée expérimentalement en comparant les résultats analytiques avec des mesures obtenues à partir d’une plaque fantôme osseuse imitant le crâne. Les résultats ont montré qu’il était possible de choisir une fréquence d’excitation optimisée en fonction de la peau et des épaisseurs osseuses améliorant la qualité d’image du TCD. Sur la base de ces résultats, des expériences Doppler ont été réalisées sur la plaque fantôme osseuse plate en tenant compte de l’effet de désadaptation d’impédance acoustique. Les résultats ont permis la aux fréquences ayant un SNR élevé de la FV aux fréquences ayant un SNR élevé. Les débits sanguins ont été calculés, ce qui a montré une grande cohérence entre les différentes expériences. L’adaption de l’émission ultrasonore à une surface irrégulière telle qu’utilisée en contrôle nondestructif a par la suite été investigué pour la fenêtre temporale. Un modèle éléments finis a été utilisé pour démontrer le concept. Des expériences ont été réalisées sur cinq fantômes d’os temporal différents ayant des épaisseurs, une atténuation et une texture différentes. Les résultats disponibles de ces expériences ont montré une énergie transmise plus élevée avec une onde compensée en surface. Dans l’ensemble, les résultats obtenus à partir de ces travaux ont jeté les bases d’une étude in vivo afin de quantifier le taux de réussite du TCD à l’aide des méthodes proposées.

Mots-clés: Échographie médicale, ondes ultrasonores massives, échographie Doppler, traitement du signal, impédance acoustique

Improvement of Image Quality of Transcranial Doppler Ultrasound

Shreyank GUPTA

ABSTRACT

Transcranial Doppler (TCD) sonography is an ultrasound method that measures blood flow velocity (FV) from the cerebral vessels. The use of TCD sonography is highly attractive as a modality because of its non-invasive nature and portability. Although TCD is recommended in the clinics, its usage is hindered in cases like vasospasm, which requires blood flow rate calculation. Blood flow rate calculation requires accurate measurement of the diameter of the blood vessel, and it can only be calculated when the image quality is good. The problem with TCD lies in the low ultrasonic energy penetrating inside the brain through the skull which leads to a low signal-to-noise ratio. This is because of several effects including phase aberration, variations in the speed of sound in the skull, scattering, the acoustic impedance mismatch, and absorption of the three-layer medium made up of soft tissues, the skull, and the brain. Secondly, there is also an energy loss because of the texture of the temporal bone. This thesis seeks to mitigate such limitations firstly through the development of an analytical model that studies the effect of transmission losses because of the acoustic impedance mismatch on the transmitted energies as a function of frequency. To do so, the wave propagation model will be shown from the ultrasonic transducer into the brain. This model calculates frequency-dependent transmission coefficient for a given skin and bone thickness. This approach was validated experimentally by comparing the analytical results with measurements obtained from a bone phantom plate mimicking the skull. The results showed that there is a possibility to choose an optimized excitation frequency based on the skin and the bone thicknesses improving the image quality of TCD. Based on these results, Doppler experiments were performed on the flat bone phantom plate considering the acoustic impedance mismatch effect. The results allowed the visualization of FV in the blood vessel phantom for the selected frequencies for which there is a high SNR. It was also shown in the results that there were some frequencies for which Doppler measurement was not possible because of low SNR. Blood mimicking fluid flow rates were calculated, which showed great consistency across different experiments. Doppler experimental results showed a major dependency on acoustic impedance mismatch. Surface adaptive ultrasound (SAUL) method, a well-known method in non-destructive testing (NDT) was proposed to mitigate the effect of transmitted energy losses due to the irregular surface of the temporal bone phantom. Firstly, a finite element model (FEM) using POGO is proposed, which implemented the SAUL method to calculate the difference in the transmitted energy with a plane wave and surface compensated wave. The results got from FEM laid a proof of concept for the experiments. Experiments were performed using five different temporal bone phantoms having different thicknesses, attenuation, and texture. The results available from these experiments showed higher transmitted energy with a surface compensated wave. Overall, the results obtained from this work laid a strong background to do an in-vivo study for larger samples to quantify the success rate in TCD using the proposed methods.

Keywords: Medical Ultrasound, Ultrasonic Bulk Waves, Doppler ultrasonography, Signal Processing, Acoustic impedance

TABLE OF CONTENTS

LIST OF TABLES

Page

LIST OF FIGURES

Page

LIST OF ABREVIATIONS

TCD	Transcranial Doppler Ultrasound
CT	Computed Tomography
US	Ultrasound
ACA	Anterior Cerebral Artery
MCA	Middle Cerebral Artery
PCA	Posterior Cerebral Artery
ICA	Interior Cerebral Artery
OA	Opthalmic Artery
VA	Vertebral Arteries
BA	Basilar Artery
PSV	Peak Systolic Velocity
EDV	End-Diastolic Velocity
FV	Flow Velocity
SNR	Signal-to-noise Ratio
MRI	Magnetic Resonance Imaging
1D	One-Dimensional
2D	Two-Dimensional
3D	Three-Dimensional
A-SCAN	Amplitude Scan

B-SCAN	Brightness Scan
B-MODE	Brightness Mode
F	Focal Number
DAS	Delay And Sum
SAUL	Surface Adaptive Ultrasound
FMC	Full Matrix Capture
TFM	Total Focusing Method
IQ	In-phase And Quadrature
ROI	Region Of Interest
FEM	Finite Element Method
CAD	Computer Aided Design
NDT	Nondestructive Testing
FFT	Fast Fourier Transform

LIST OF SYMBOLS AND UNITS OF MEASUREMENTS

MHz	Megahertz
kHz	Kilohertz
Hz	Hertz
p	Pressure
t	Time
c	Velocity of the medium
v	Doppler velocity
ρ_0	Mean density
k	Adiabatic compressibility
α	Attenuation
f	Frequency
Z	Acoustic impedance
u	Acoustic flow
θ	Angle
R	Reflection coefficient
T	Transmission coefficient
μm	Micrometer
m	Meter
mm	Millimeter

cm	Centimeter
Δ	Difference
λ	Wavelength
d_0	Distance
R_{axial}	Axial resolution
MRayl	MegaRayl
Rayl/m^2	Rayl per square meter
t_x	Layer thickness
T_x	Transmission matrix
dB	Decibel
m/s	Meter per second
cm/s	Centimeter per second
kg/m^3	Kilogram per cubic meter
$\bar{x}$	Mean
S	Standard deviation
$\sum$	Summation
ms	Millisecond
μs	Microsecond
ns	Nanosecond
s	Second

τ	Emission time
d	Diameter
Q	Flow rate
ml/min	Millimeter per minute
δ	Derivative
v_{max}	Maximum velocity
I	Image
Pa	Pascal
GPa	Giga Pascal
E	Modulus of elasticity

INTRODUCTION

Stroke is the second leading cause of death in developed nations, and in fact, in Canada, one person dies every seven minutes from stroke (Donkor, 2018). There are other diseases like sickle disease and vasospasm which further add to the statistics of the death rate caused by cerebrovascular disease. At present, doctors mainly rely on X-ray computed tomography (CT) for diagnosis (Smith, Roberts, Chuang, Ong, Lee, Johnston & Dillon, 2003). The problem with diagnosis using CT scans is that they cannot be performed repeatedly because of the exposure to harmful radiation. There is therefore a need for a system which can be used often for monitoring while also providing reliable information about a patient's health. Transcranial Doppler (TCD) may provide an answer to this challenge. TCD uses ultrasonic waves which are non-ionizing and safer to use than CT. TCD currently helps in diagnosing cerebrovascular diseases of the brain by detecting variations in blood flow velocity (FV). It is also inexpensive and portable. The other important advantage of TCD is that, it can be repeated multiple times in a day and can also be used for monitoring the blood velocity. TCD was first introduced by (Aaslid, 1986). A frequency in the range of 2-2.5 MHz is, nowadays typically used. The reflections of the moving red blood cells measure the blood velocity through the Doppler effect. A typical image captured by a TCD system is shown in Fig. 0.1 using focused US waves. The captured image is reconstructed using the color Doppler technique which shows FV as well as the direction of blood flow. To determine blood flow information, this image is often superimposed on a B mode image (Moorthy, 1993). In a color Doppler image, the particles moving towards the probe are shown in red. This phenomenon is happening in the middle cerebral artery (MCA). The particles moving away from the probe are shown in blue. This phenomenon is happening in the anterior cerebral artery (ACA). There is also an area within the image where mixing of red and blue occurs. This mixing is contained inside the white circle and is because of aliasing which will be discussed in Section 1.6.1. There are also different techniques to capture Doppler data such as power Doppler, continuous wave Doppler, pulsed wave Doppler and spectral Doppler as mentioned in (Moorthy, 1993). However, in this thesis, color Doppler was chosen as the primary method to determine blood flow. This method was preferred since the FV and the flow direction can be calculated. Moreover, the diameter of the vessel can be estimated from a B-Mode image therefore resulting in an estimation of the blood flow.

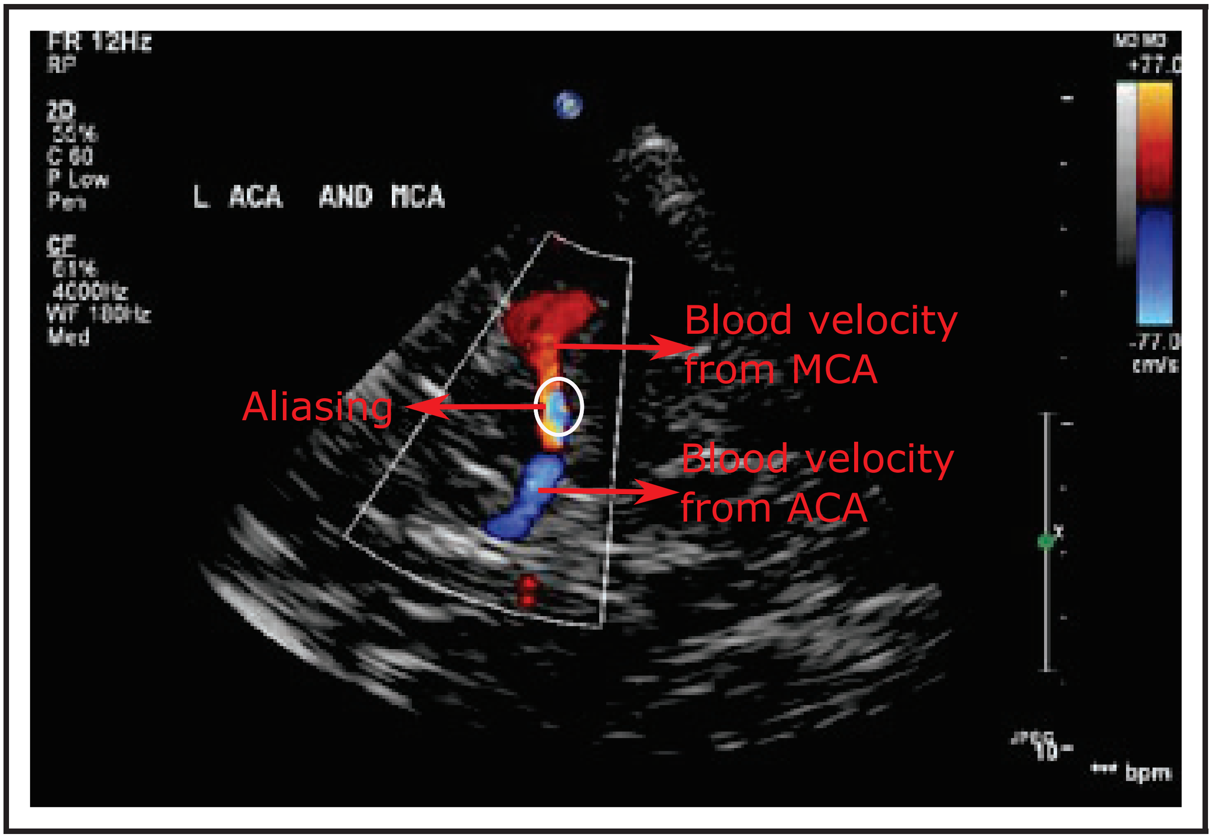

Figure 0.1 A TCD image showing blood FV in red and blue. Red pixels show blood particles flowing towards the transducer in the middle cerebral artery (MCA). Blue pixels show blood particles flowing away from the transducer, in the anterior cerebral artery (ACA). There is also blue color mixed with red color shown in the white circle which is due to aliasing. The low contrast of the image masks the internal features of the brain including the vessel boundaries (Ultrasound, 2012)

.

The first step to perform a TCD measurement is to find an area of the skull where it is easy for the ultrasounds (US) to penetrate. These areas are called windows. The three main windows for accessing the cerebral arteries are shown in Fig. 0.2a. The transtemporal (temporal) window is used to expose the MCA, the ACA, and the posterior cerebral artery (PCA), and the terminal portion of the internal carotid artery (ICA). The transorbital (orbital) window exposes the ophthalmic artery (OA) as well as the ICA. The transforaminal (occipital) window exposes vertebral arteries (VA) and the basilar artery (BA) (Sarkar, Ghosh, Ghosh & Collier, 2007). TCD aims to detect the blood flow velocity (FV) in the insonated arteries and to display information as a velocity-time waveform as shown in Fig. 0.2b. The peak point of this curve is called peak systolic velocity (PSV) and the bottom valley is called end-diastolic velocity (EDV). Clinicians use the measured PSV and EDV to help in the diagnosis of cerebral vasospasm, intracranial pressure and stroke.

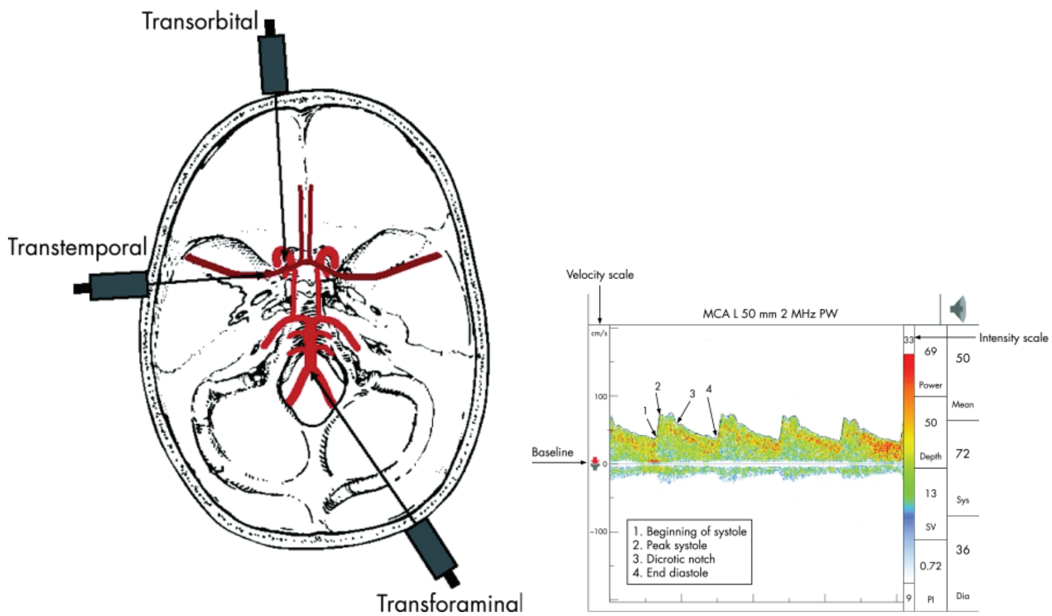

a) Transcranial brain vessels

b) Doppler spectra

Figure 0.2 (a) Transorbital, transtemporal and transforaminal windows are the parts of the skull from where TCD measurements can be performed (Sarkar *et al.*, 2007) (b) Received Doppler spectrum from the MCA showing the blood flow towards the emitter because it is on the positive velocity scale, a Doppler spectrum with negative velocity scale reflects blood flowing away from the emitting device (Sarkar *et al.*, 2007).

0.1 Challenges faced by TCD

One of the key challenges which TCD faces is to detect vasospasm. Measuring flow rate (rather than just blood FV) is important for the detection of vasospasm. Blood flow rate can be determined if the diameter of the vessel is known. It is proportional to blood FV and the square of the vessel diameter. The contrast in current TCD images is too low to measure it accurately. Conventionally, the blood FV of the MCA increases to more than 120 cm/s in the case of vasospasm and it keeps increasing up to a critical point as the artery narrows down. After that critical point, the blood FV decreases drastically, as shown in the Fig. 0.3. At points A and B of the Fig. 0.3, the blood FV is the same despite a narrowing of the vessel. Misinterpretations about vasospasm can occur if the diameter is not known. This is the reason vasospasm is more strongly correlated with the blood flow than the blood FV.

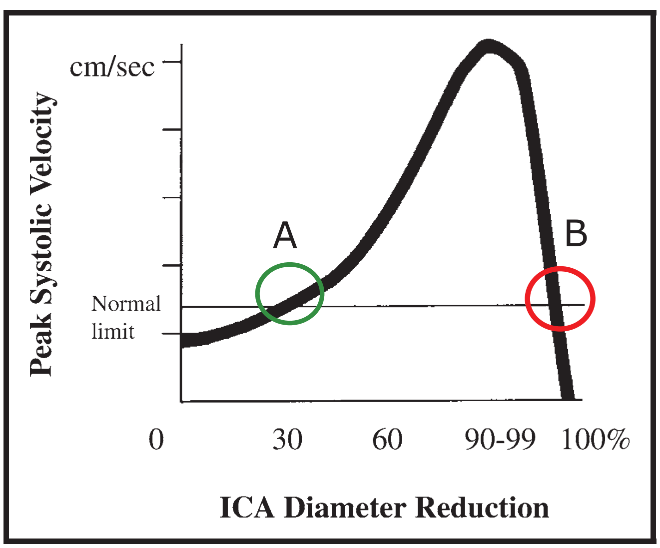

Figure 0.3 This figure shows the FV variation as the diameter of the vessel reduces. The x-axis shows the reduction of the diameter, and the y-axis shows the peak systolic velocity. Points A and B in the image produce ambiguity in detecting vasospasm since at both points the FV remain the same despite narrowing of the vessel (Alexandrov *et al.*, 1997).

0.2 Motivation

Though TCD many advantages in diagnostic applications, including, for example, the estimation of intracranial pressure, the use of TCD is often limited in the clinical environment. The reliability of the TCD velocity profile is not generally accepted by the medical community (White & Venkatesh, 2006) because some diseases are more correlated to the blood flow as compared to the blood FV. Adding to that, less than 10% of stroke patients are treated accurately because the current TCD systems have poor image quality which makes blood flow measurement difficult for early detection (Thomas, 2017). So, the primary motivation behind this work is the successful measurement of the blood flow through the skull. Successful measurement of blood flow might be possible by improving the image quality of TCD systems.

In TCD, poor image quality is basically because too little US is transmitted to the brain. Poor transmission in the brain is because of the presence of the skull in the ultrasonic wave propagation path. Two effects which make ultrasonic transmission poor are: (1) attenuation and (2) acoustic impedance mismatch. The acoustic impedance mismatch has a complex relationship with the frequency whereby there is a loss in the transmitted energy at the different interfaces along the ultrasonic wave propagation path. This effect is shown in Fig. 0.4, which was obtained via an analytical model described in the section 2.2.1 and shows how much acoustic energy is transmitted through the skin and bone at 2 MHz.

For many combinations of skin and bone thickness, the model predicts near-zero energy transmission because of the acoustic impedance mismatch between the skin and the bone. Image formation would not be feasible with such low energies. There is also a strong loss of signal because the attenuation in the skull is high and is a function of frequency. This causes a low signal-to-noise ratio (SNR) which directly correlates to the contrast in the images. Because of this low contrast, clinicians are not always able to see the vessels in images, making blood flow measurements difficult. However, on might argue that poor transmission can be solved by providing higher voltages to ultrasonic emitting device. However, the U.S. Food and Drug Administration (FDA) recommends a maximum spatial-peak temporal-average intensity of 90 mW/cm^2 for applications in the brain. The maximum transmitted intensity is directly related to the voltage transmitted by the ultrasound system and the design of the probe (Alder, 2002).

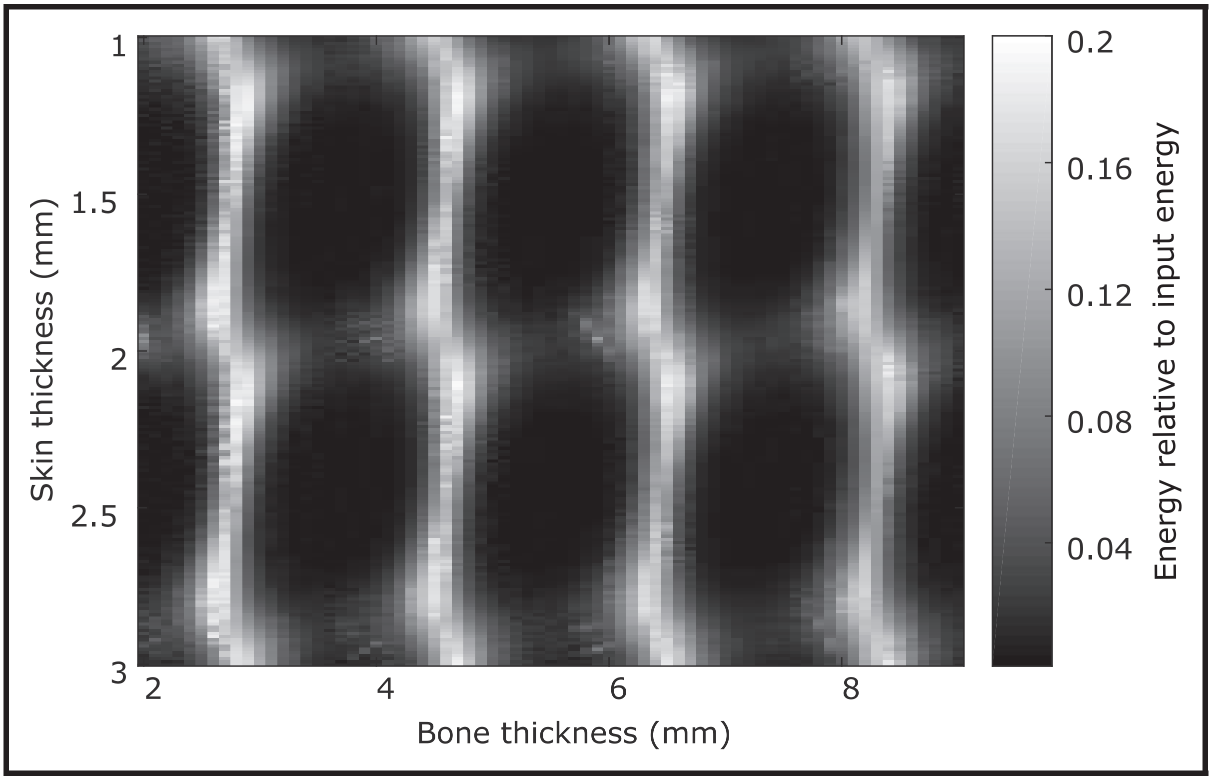

Figure 0.4 Transmitted energy as a function of skin and bone thickness. The figure shows a simulated map of the ultrasonic energy transmitted to the brain using a center frequency of 2 MHz.

0.3 Objectives

The purpose of this thesis is to develop a method which allows visualization of blood vessels beneath the bone and therefore successfully measure the blood flow. The measurement of the blood flow requires the blood FV as well as the blood vessel diameter. Thus, the objectives of this thesis are to:

1. Optimize and design a probe specifically for TCD measurements based on matching acoustic impedance. Using designed probe, perform a simulation and an in vitro experimental study to identify the optimal frequency as a function of the soft tissue and bone thicknesses in a flat bone phantom plate.

2. Validate the feasibility of Doppler imaging using the optimal frequencies identified in objective 1

3. Reduce the distortion of plane waves as they propagate through a bone with an irregular surface to enhance the transmission of ultrasonic waves.

0.4 Thesis Organization

Chapter 2 begins with a general description of ultrasonic waves propagation which is followed by a literature review of ultrasonic probe characterization, different kinds of image formation using ultrasonic waves, Doppler blood FV estimation and its relation to blood flow.

Chapter 3 presents an analytical model for the effect of frequency on acoustic impedance mismatch, taking into account skin and bone thickness. It also presents an experimental validation of the model, and results that suggest optimal frequencies to be used for given skin and bone thicknesses.

Chapter 4 presents the validation of the optimized frequencies found in chapter 3 when applied to Doppler ultrasonography. Thereafter, blood flow is calculated for the selected optimized frequency for a flat bone phantom.

Chapter 5 presents the concept of using surface compensated ultrasonic waves compared with conventional plane wave imaging. The chapter ends with results demonstrating that combining acoustic impedance matching and surface compensated ultrasonic waves does improve transcranial B-Scan images compared to the conventional methods.

Lastly, this work is summarized in Chapter 6. Discussion of the two approaches (acoustic impedance mismatch and improving distorted plane waves), as well as future avenues towards improvement of the TCD imaging, are discussed. The necessary future work and the identification of shortcomings of the current approaches are also presented.

CHAPTER 1

LITERATURE REVIEW

This chapter first gives information about the general theory of ultrasonic wave propagation relevant to this thesis. The topics which are covered in the literature review are probe design, image formation typically used with US, Doppler processing, and lastly ultrasonic wave propagation through irregular bone surfaces.

1.1 Brief introduction

US is an acoustic wave with a frequency that is above the upper limit of human hearing at 20 kHz. US are mechanical waves that transmit the energy of a particle step by step to other parts of the medium. The propagation of the energy can be parallel or transverse relative to the direction of propagation as shown in Fig. 1.1. The waves which travel parallel to the direction of propagation are called longitudinal waves and those travelling perpendicular to the direction of propagation are called transverse waves. All materials support longitudinal waves. However, transverse waves can travel only in solids and viscoelastic fluids. This thesis considers only the propagation of longitudinal waves. Acoustic waves are fundamentally non-linear waves, but usage of linear theory for diagnostic US is normally accepted as it captures all the important information without going into complex analysis (Pietrangelo, 2013). For this thesis, linear wave propagation was considered.

Mathematically 1-D plane wave propagation (Ludwig & Levin, 1995) can be represented by Eq. 1.1

$$\frac{\partial^2 p(z,t)}{\partial^2 z} = \frac{1}{c^2}\left(\frac{\partial^2 p(z,t)}{\partial t^2}\right) \tag{1.1}$$

where p is the acoustic pressure, c is the velocity of the medium in which the US travels, z is the direction of travel and t is the time. The speed of sound c in Eq. 1.1 depends on the mechanical

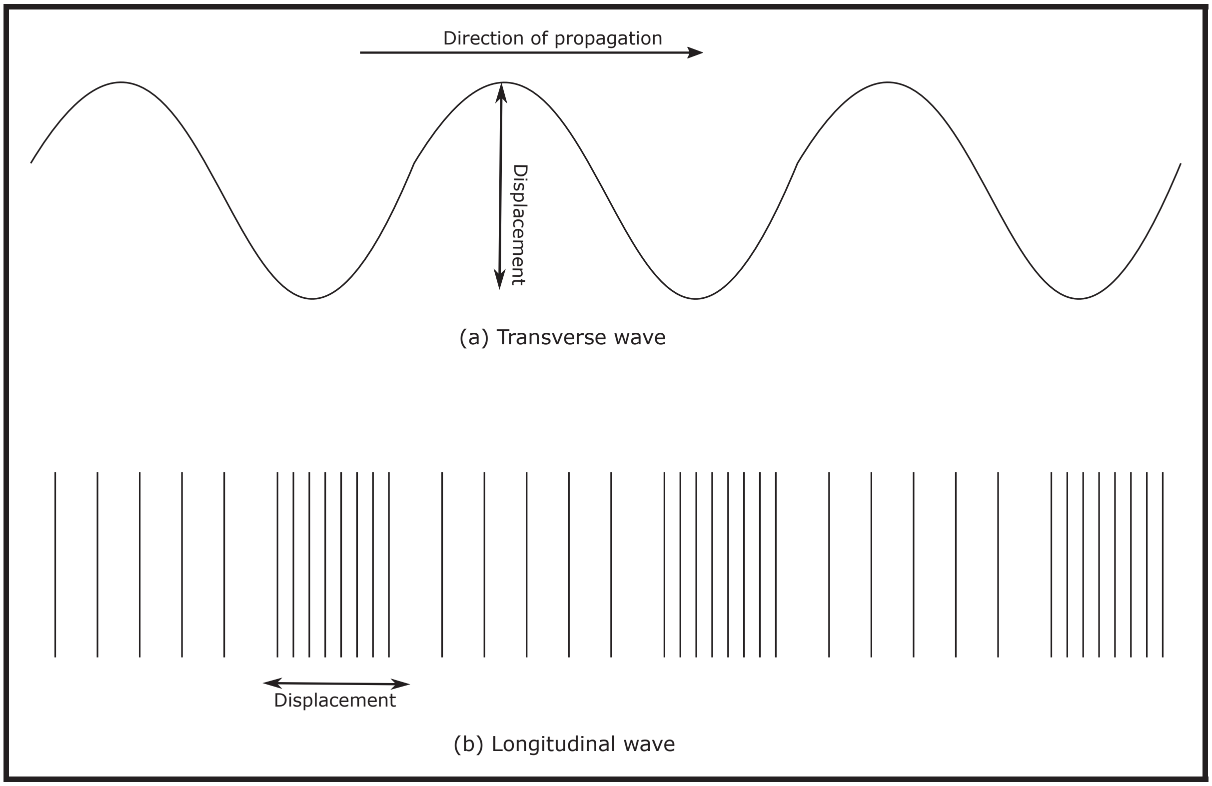

Figure 1.1 Diagram showing different types of ultrasonic wave in nature. Transverse wave travel perpendicular and longitudinal wave travels parallel to the direction of propagation.

properties of the medium as given in Eq. 1.2

$$c = \sqrt{\frac{1}{\rho_0 k}} \tag{1.2}$$

where ρ_0 is the mean density of particles, and k is the adiabatic compressibility of the material (Jensen, 1996).

When ultrasonic wave travels, it loses its energy as it propagates through attenuation. Attenuation in bones and soft tissue can arise from several complex phenomena and is difficult to explain solely from the fundamental equations. But the three primary sources of attenuation are: (1) absorption, (2) scattering, (3) mode conversion (Hoskins, Martin & Thrush, 2010). There are several models which combine various energy loss to give a single equation based on frequency

(Pietrangelo, 2013) as given by Eq. 1.3

$$\alpha(f) = \alpha_1 f \tag{1.3}$$

,where α_1 is dependent for a specific medium in which an ultrasonic wave travels and f is the frequency of oscillation. Typically $\alpha(f)$ is expressed in dB.

Another important component in which there is a loss of energy is the characteristic acoustic impedance Z. Acoustic impedance measures the extent to which a system opposes an acoustic flow when an acoustic pressure is applied to it as shown in Eq. 1.4 where p is the pressure applied and u is the acoustic flow. Using Eq. 1.4, another definition of acoustic impedance (Z) can be derived which depends directly on the density (ρ) and speed of sound (v) in the material as shown in Eq. 1.5 (Randall, 2012). Once the US travels through the interface between two media, the transmission of energy is reduced because of acoustic impedance mismatch along the propagation path.

$$Z = \frac{p}{u} \tag{1.4}$$

$$Z = \rho v \tag{1.5}$$

Whenever ultrasonic wave interacts with the interface between two media, there is a reflection and transmission of energy through the examined medium. This reflection and transmission occur because of the change in acoustic impedance. The higher the acoustic impedance difference between US emitting device and medium under examination, the higher the reflection will be. Reflection from the medium can be specular or diffusive depending on the ratio of US wavelength and interaction size. Specular reflection happens where boundaries are much larger than the acoustic wavelength and can be analyzed using basic ray theory. In ray theory, when an ultrasonic wave is incident with an angle of θ_i, a part of it gets transmitted with an angle of θ_t.

This interaction between two media follows Snell's law (Glassner, 1989) as described in Eq. 1.6

$$\frac{c_1}{\sin(\theta_i)} = \frac{c_2}{\sin(\theta_t)} \tag{1.6}$$

where c_1 and c_2 are the sound velocities for the medium where ultrasonic wave was generated and transmitted. θ_i and θ_t are the angles of incidence and transmission respectively. The reflection coefficient, which describes the magnitude of the reflection when there is an interaction between the US and a medium is given by Eq. 1.7 and transmission coefficient by Eq. 1.8 (Cheeke, 2002)

$$R = \frac{Z_1 \cos\theta_i - Z_2 \cos\theta_t}{Z_1 \cos\theta_i + Z_2 \cos\theta_t} \tag{1.7}$$

$$T = \frac{2Z_1 \cos\theta_i}{Z_1 \cos\theta_i + Z_2 \cos\theta_t} \tag{1.8}$$

where Z_n is the acoustic impedance of the medium. Often the unit used for acoustic impedance is the Rayl per square meter (Rayl$/m^2$). The coefficient corresponding to the ratio of energy reflected from the medium is the square of R in Eq. 1.7 and since energy is conserved transmitted energy coefficient would be $1 - R^2$. Typical Z value for bone is 7 MRayl and for soft tissue it is 1.5 MRayl (Hoskins *et al.*, 2010). Loss because of acoustic impedance mismatch is a challenge in TCD imaging. This loss is in addition to the losses due to the attenuation through the bone.

Another kind of reflection is diffusive reflection, in which the dimension of the interacting boundaries is much smaller than the acoustic wavelength. When the incoming ultrasonic wave interacts with the boundary, it scatters in multiple directions as shown in Fig. 1.3

Because of diffusive reflection incoming wave gets scattered in different directions. The usage of diffusive reflection is very important in medical ultrasound when calculating blood FV. Blood is an inhomogeneous fluid which contains small particles of size approximately 5μm which is

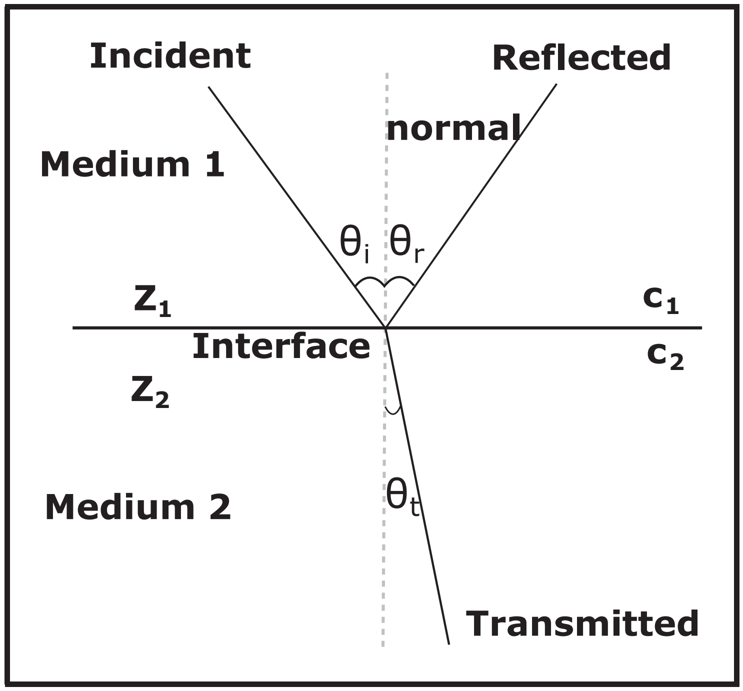

Figure 1.2 Diagram showing the concept of Snell law and an example of specular reflection. An incident ray from medium 1 with incidence angle of θ_i upon interacting with medium 2 gets reflected with angle θ_r and transmitted with angle θ_t. The amount of energy distributed in reflection and transmission depends on acoustic impedances Z_1 and Z_2.

much less than the wavelength (λ) typically used in TCD. When ultrasonic wave interacts with small particles, information from the scattered wave is captured and processed using Doppler theory to estimate blood FV.

1.1.1 Concept and principle of Doppler effect

The primary aim of TCD is to diagnose cerebrovascular disease based on the calculation of blood flow, which is related to blood FV. To compute blood FV, TCD uses the Doppler effect illustrated in Fig. 1.4. The basic principle behind this phenomenon is: when a source is stationary, a stationary observer hears the same frequency as the source, but if the source is moving, then the observer in front of the source hears a higher frequency and an observer behind the source

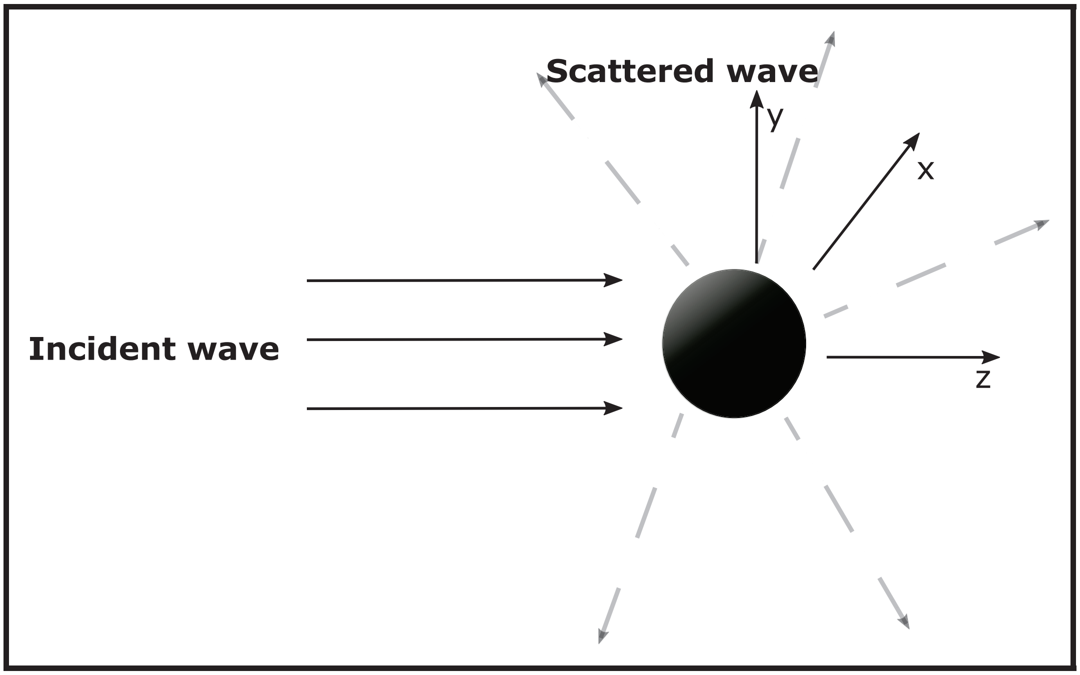

Figure 1.3 Diffusive scattering from a particle whose size is much less than the incoming wavelength

hears a lower frequency. The relationship between the frequency f_r heard by the observer and frequency f_t emitted by a source is approximately.

$$\textbf{Received frequency:} \qquad f_r = (1 + \frac{\Delta v}{c}) \cdot f_t \tag{1.9}$$

$$\textbf{Change in frequency:} \qquad \Delta f = (\frac{\Delta v}{c}) \cdot f_t, \tag{1.10}$$

where $\Delta f = f_r - f_t$ is called the Doppler shift, where c is the speed of sound in the medium in which US travels and Δv is the velocity of the receiver relative to the source: it is positive when the source and the receiver are moving towards each other and negative when they are moving away from each other

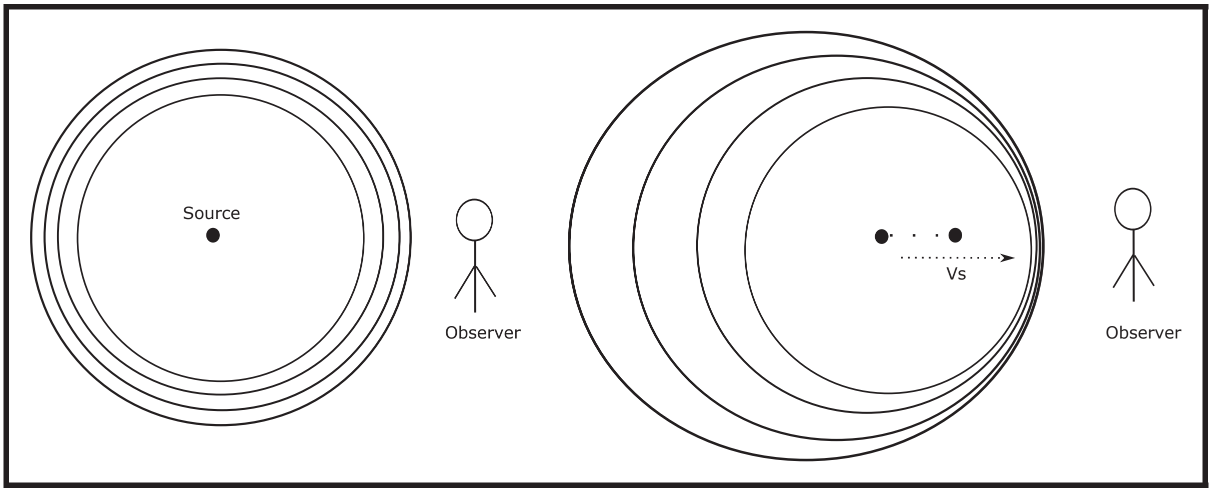

Figure 1.4 Left: when the source is stationary, all the observers will hear the same frequency. Right: when the source is moving at velocity v_s resulting in shifts of the wavefronts, an observer to the right hears the sound with higher frequency as compared to the observer to the left of the source.

In this thesis, the primary focus is on blood FV and blood flow measurements. The Doppler effect enables the US to be used to detect the motion of blood. When the ultrasonic probe emits, it acts a stationary source, and the red blood cells are moving observers. When the ultrasonic probe receives a signal, it is a stationary observer, and the red blood cells are moving sources as shown in Fig. 1.5. Depending on the movement of the blood cells, there is a change in the frequency with respect to the frequency transmitted by the ultrasonic probe. This change depends on whether the blood particle is stationary, moving towards the transducer, or moving away from the transducer. This interaction causes ultrasonic waves to scatter in different directions, some of which coincide with the direction towards the probe and is detected. So a Doppler shift occurs twice between transmission and reception (Hoskins *et al.*, 2010). Finally, the velocity of the moving blood particles is calculated according to the formula:

$$v = \frac{c \cdot \Delta f}{2 \cdot f_t \cdot cos\theta}, \tag{1.11}$$

where $\Delta f = f_r - f_t$, f_t is the emitted frequency, f_r is the reflected frequency, c is the speed of sound in the medium in which ultrasonic wave travels, Δf is the Doppler shift, and θ is the angle between the device and moving particle.

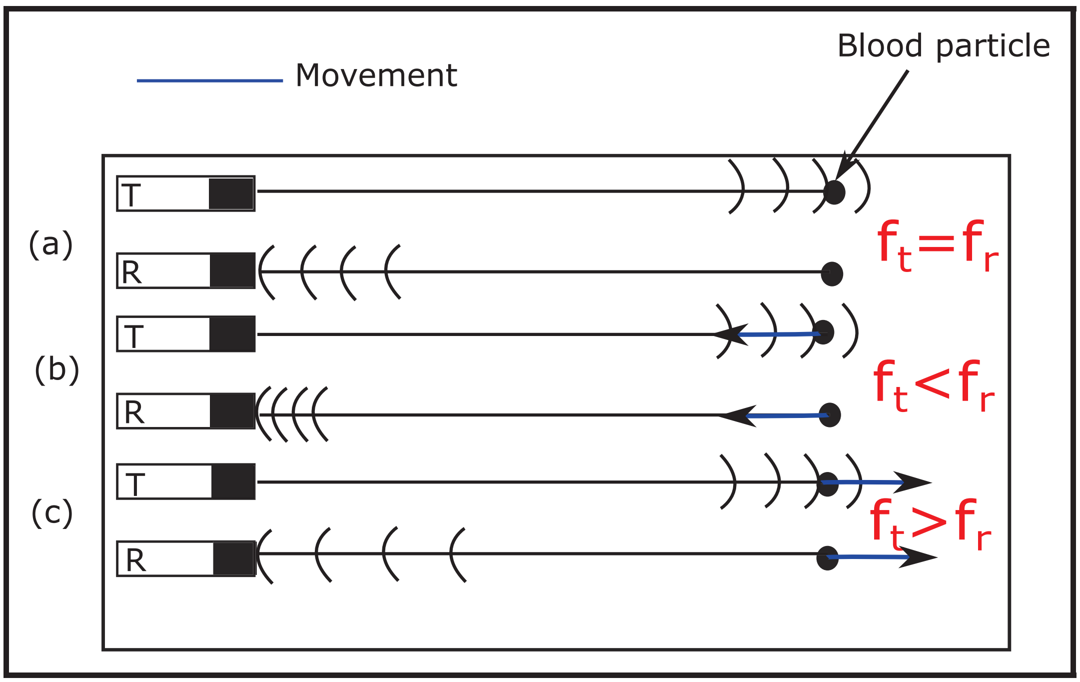

Figure 1.5 T and R represents transmitter and receiver respectively of a probe, blue lines show the movement of blood particles (a) The probe and blood are not moving; the transmitted and received frequency are equal. (b) The blood particle is moving towards the probe, the frequency of the received US by the transducer is greater than the transmitted frequency. (c) The blood particle is moving away from the probe, the frequency of the received US by the transducer is lower than the transmitted frequency (Hoskins *et al.*, 2010).

1.2 Probe design, Image formation and Irregular surface compensation

A TCD system can be divided into three key parts as shown in Fig. 1.6. In this figure, the front end is the part that is operated by a clinician and comprises an ultrasonic probe. The signal processing block performs signal acquisition and processing, and lastly, the back end transfer these signals to an image reconstruction algorithm to form the images. The final image is seen again by a clinician through a display monitor.

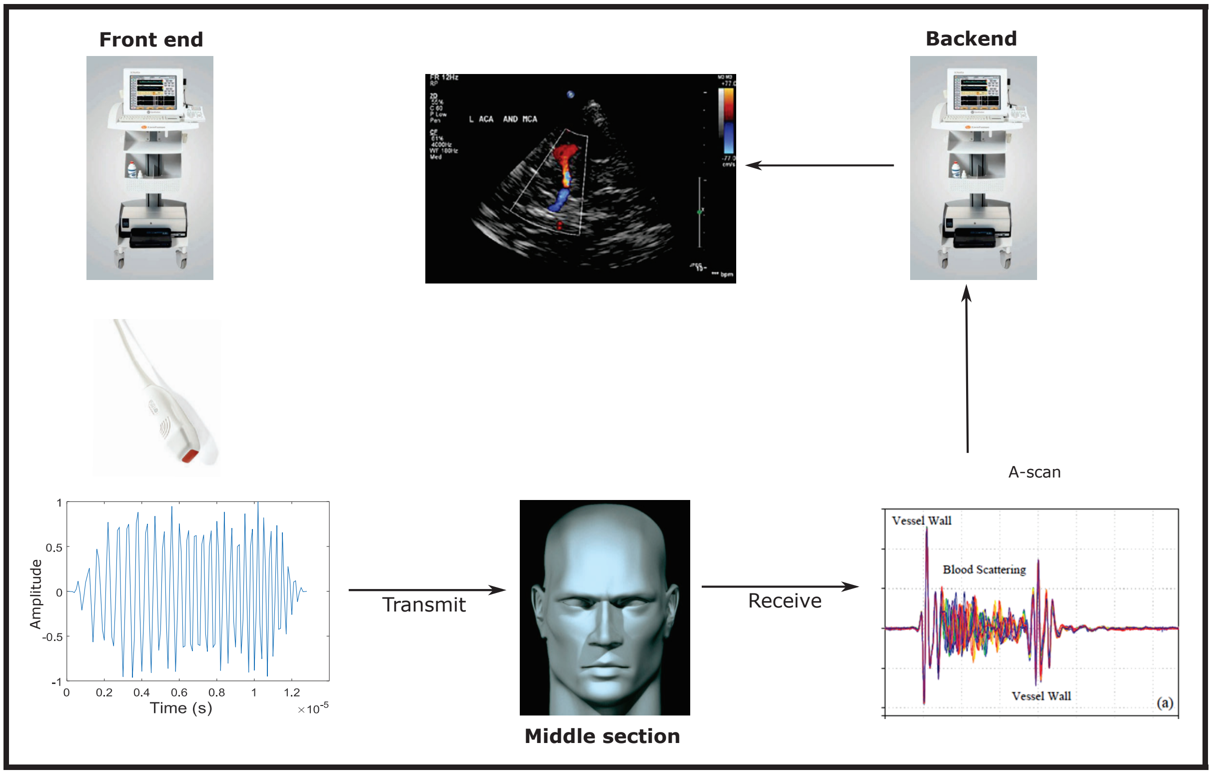

Figure 1.6 Figure shows an abstract diagram of a TCD system which can be divided into three parts: the front end, is operated by a clinician, the middle section acquire and process the signals, the backend forms and diplays the images

1.3 Ultrasonic probe

A device emitting and receiving ultrasonic waves is called an ultrasonic probe or an ultrasonic transducer as shown in Fig. 1.7a. When it is placed between two electrodes and external voltage is applied, it vibrates and mechanical oscillations occur. These oscillations are emitted as ultrasonic waves, as illustrated in Fig. 1.7b. Conversely, when mechanical oscillations are applied to the piezoelectric material (e.g., when ultrasound is reflected off an interface between media with differing acoustic impedances), these are received as electrical signals.

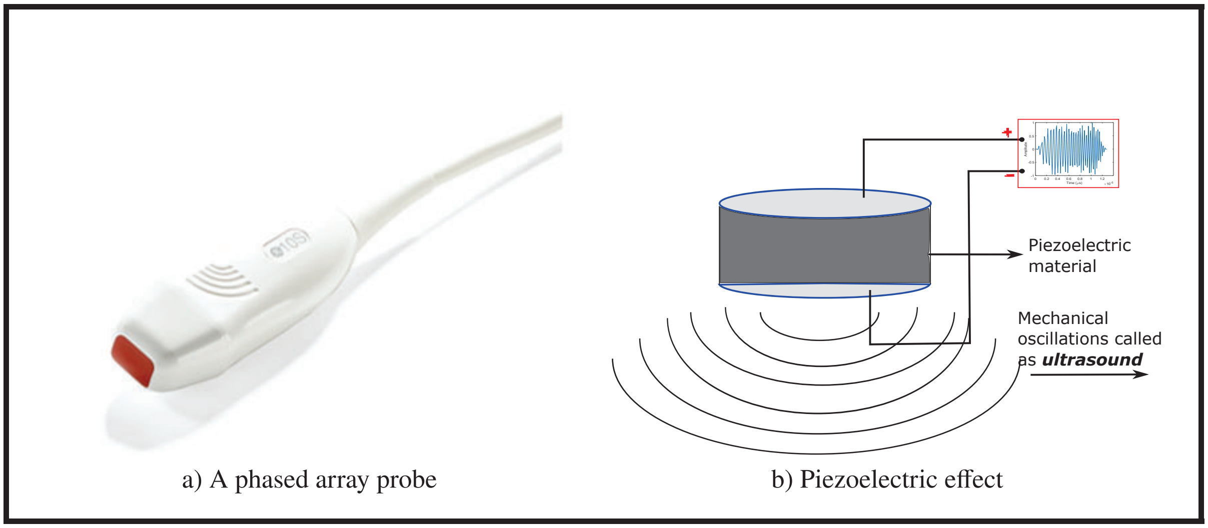

Figure 1.7 (a) A phased array probe or transducer used for medical imaging (b) An external voltage is given to the piezoelectric element causing mechanical vibrations which are emitted as US.

1.4 Probe design and matching layer

An ultrasonic transducer consists of three layers: the backing layer, the piezoelectric material, and the matching layer, as shown in Fig. 1.8. The optimization of the matching layer ensures it transmits the maximum possible ultrasonic pressure. Once high energy is sent to the brain, SNR (signal power/noise power ratio) improves (assuming noise power remains constant throughout the system).

1.4.1 Matching layer

The matching layer is layer placed in front of the transducer to maximize energy transmission. To understand the need for the matching layer, it is important to understand the propagation of ultrasonic waves through interfaces between different media. The interaction of ultrasonic waves at the interface of different media results in transmission losses (Shung & Zippuro, 1996) as illustrated in Fig. 1.9. In this figure, an US wave is incident from the piezoelectric element to the imaging tissue. Because of the difference between the acoustic impedance of the piezoelectric

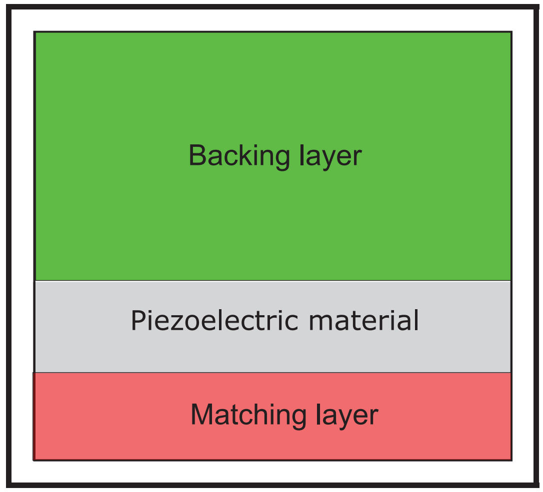

Figure 1.8 A typical ultrasonic transducer consists of three layers: A backing layer, piezoelectric layer, and a matching layer to enhance the transmission.

element and the tissue most of the incident US pressure/energy is reflected. This loss in the transmission causes poor SNR in the images of the tissue.

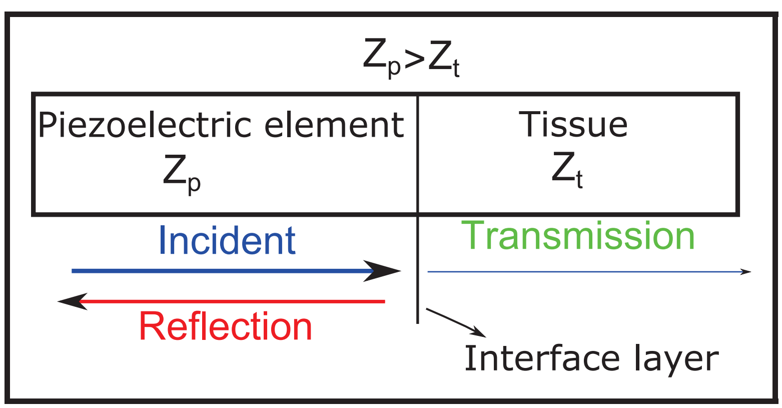

Figure 1.9 The left part of the figure shows a piezoelectric element and right part shows a soft tissue. Due to impedance mismatch there is a loss in the transmission of US, thickness of the line denote the signal strength.

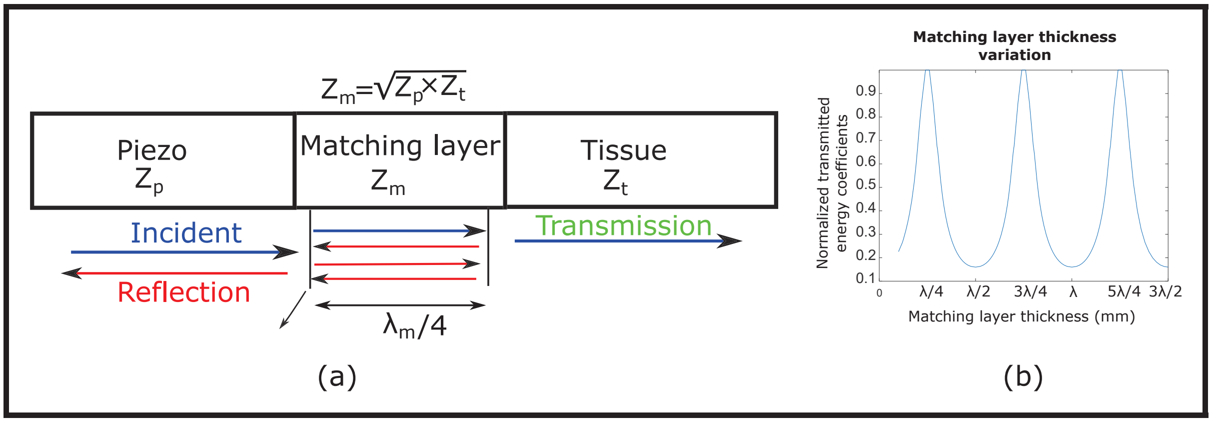

Figure 1.10 (a) Matching layer design consideration, showing its impedance to be the mean of the piezoelectric element and imaging tissue impedance and thickness to be $\lambda_m/4$. By doing so, a series of overlapping waves that are in phase with each other occur which improves energy transmission. (b) An analytical simulation showing the transmitted energy coefficients as a function of matching layer thickness in terms of λ. Whenever the matching layer thickness becomes odd integer multiple of $\lambda/4$ maximum possible transmission occurs and at $\lambda/2$ minimum transmission occurs.

To overcome this effect, there are theories which introduce the concept of matching layer. Modelling techniques, like the Mason Equivalent Circuit (Blackstock, 2000), Wave Guide and Krimholtz-Lee-Mathaei Equivalent Circuit (Krimholtz, Leedom & Matthaei, 1970) explain matching layer design for the ultrasonic transducers. The matching layer's acoustic impedance should be the geometric mean of the piezoelectric material (Z_p) and the imaging tissue (Z_t) as shown in Fig. 1.10 for maximum possible transmission in the imaging tissue (Alvarez-Arenas, 2004). Fig. 1.10 (a) shows that ultrasonic waves reverberating within the matching layer produces a series of overlapping waves that are in phase with each other when its thickness is a multiple of the US quarter wavelength. Hence, when they are joined, these provide a stronger resulting wave. It means that the matching thickness at quarter wavelength will have constructive interference. If the matching thickness deviates from quarter wavelength, intensity of the US starts to attenuate because of destructive interference. Fig. 1.10 (b) shows a similar situation in an analytical simulation that whenever the matching thickness becomes odd integer multiple of $\lambda/4$ maximum possible transmission occurs.

1.5 Probe design: Frequency optimization

In the past, much work was done to improve the energy transmitted through the skull, mainly considering the attenuation effect (Lindsey, Light, Nicoletto, Bennett, Laskowitz & Smith, 2011; Lindsey, Nicoletto, Bennett, Laskowitz & Smith, 2013; Yousefi, Goertz & Hynynen, 2009), and time reversal techniques (Fink, 1992; Gauss, Trahey & Soo, 2001; Haworth, Fowlkes, Carson & Kripfgans, 2008; Liu & Waag, 1994; Pernot, Montaldo, Tanter & Fink, 2006) but the design of the probe considering the acoustic impedance mismatch effect was typically ignored.

(Yue, Liu, Wang, Di, Lin, Wang & Luo, 2014) designed a probe for TCD that improved the transducer sensitivity and the bandwidth but used the frequency range typically used in TCD. This probe improved image resolution because it had a wide range of frequencies, but the problem of poor ultrasonic transmission through the temporal bone persisted since neither attenuation nor acoustic impedance mismatch were considered. Klotzsch et.al (Klötzsch, Popescu & Berlit, 1998) studied how to improve transcranial imaging and showed that a 1 MHz probe allowed a better insonation of patients. Their study showed that vessels could be characterized in only 25% of patients when using a 2 MHz probe, but it was close to 100% when using a 1 MHz probe. This study showed that adapting the frequency in TCD might improve the success rate. Since the transmitting frequency was reduced to 1 MHz, the resolution of the images worsened. (Lindsey *et al.*, 2011) designed custom 2D sparse array transducers. They placed the transducer arrays on either side of the temporal acoustic windows and combined the received signals from both sides to make one final image. By doing so, they eliminated the effect of asymmetry on either side of the window. In another study (Aarnio, Clement & Hynynen, 2005) showed the occurrence of spectral peaks in transmission in real skulls in five out of six anatomical sites as shown in Fig. 1.11. However, the effect of an acoustic impedance mismatch at the bone-soft tissue interface was ignored in the frequency selection. (White, Clement & Hynynen, 2006a), (Aarnio *et al.*, 2005) and, (Clement & Hynynen, 2002) used analytical models to study the phase shift and the attenuation through the skull. They performed these studies at different locations of the skull and depicted the variation of ultrasonic energy as a function of skull thicknesses and phase shifts. However, these studies neglected the effect of the skin thickness on the acoustic impedance

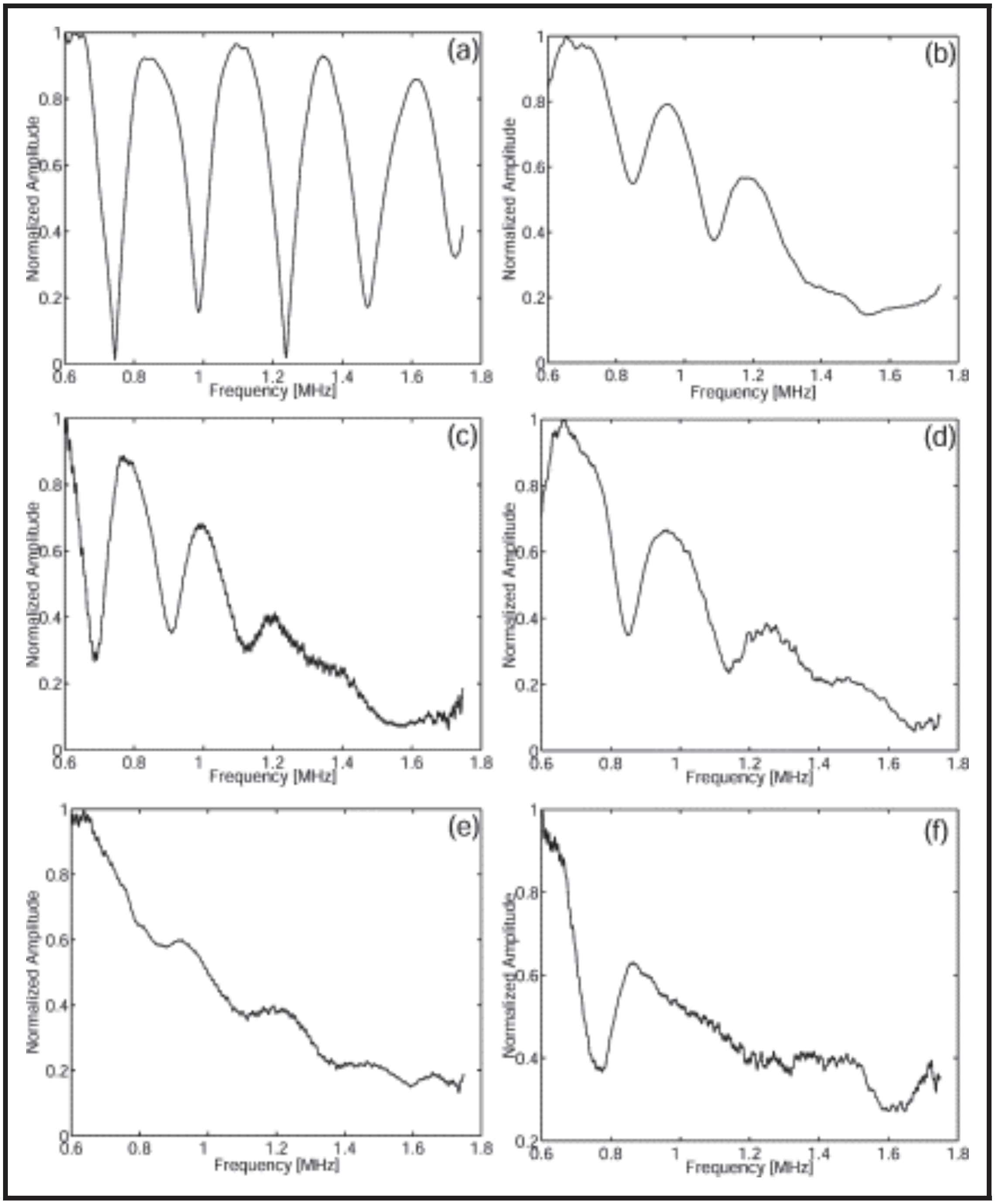

Figure 1.11 Figure showing spectra of reflected signal from different locations of the skull. Apart from (a) which shows nearly an idle spectrum, the other spectra degrades for frequency higher than 1 MHz. But resonances can still be separated. This figure was directly taken from Aarnio *et al.* (2005)

mismatch. Adding the skin thickness might change the overall variation of ultrasonic energy as a function of frequency. (Yousefi *et al.*, 2009) did a study on excitation frequency selection for transcranial imaging. They specifically mentioned aiming for frequencies below 1 MHz. There were two reasons behind this: (1) the scattering of the US, because parameters like density and bulk modulus of blood differ from that of it's surrounding tissues (Kollár, Schulte-Altedorneburg, Sikula, Fülesdi, Ringelstein, Mehta, Csiba & Droste, 2004; White, 1992), and (2) the attenuation caused by the skull (Fry & Barger, 1978). Scattering and attenuation cause losses in the signal's energy. They also considered the use of shear waves to enhance ultrasonic transmission through the skull, as this improves acoustic impedance matching, and reduces refraction and phase alteration compared to longitudinal waves (Yousefi *et al.*, 2009). But the problem with this method was that the amplitude of shear waves was lower than that of longitudinal waves, which resulted in poor SNR, and low contrast in the images. Apart from these effects, researchers have also aimed at correcting ultrasonic waveform aberration caused by the skull (Flax & O'Donnell, 1988). A technique that has attracted the attention of many researchers is the time reversal technique (Fink, 1992; Gauss *et al.*, 2001; Haworth *et al.*, 2008; Liu & Waag, 1994; Pernot *et al.*, 2006).

The technique computes the delays for the elements of the probe from MRI and CT images of the skull. This technique improves the contrast and spatial resolution of the images, but since each person has different skull properties, it is impractical to use in an intensive care setting.

The choice of the transmitted frequency based on the bone-soft tissue interaction studied in depth in the discussed literature.

Therefore, one aim of this thesis is to explore the frequency-dependent effect of acoustic impedance mismatch, which relates to optimizing the transmitted frequency for TCD. Once the optimal frequency is chosen regarding the acoustic impedance, the other effect of spatially varying acoustical properties will indeed be important. They will, however, be significant at all frequencies. Therefore, the choice of the acoustic impedance dependent optimal frequency will always be beneficial. This is an important step towards understanding the reasons behind the poor ultrasonic transmission in TCD and, devise a methodology to improve TCD imaging.

1.6 Image formation

An ultrasonic transducer is placed in contact with the skin. Ultrasonic waves are sent into the body and the transducer receives echos. The received ultrasonic signals contain reflections from the underlying tissues. The received 1D signals are called A-scans and can be plotted as received pressure over time. They represent a line and are placed side by side for multiple scans as shown in Fig. 1.12. A 2-D US image which represents reflection intensities from tissues and organs within the body is called a B-scan image as shown in Fig. 1.12. The US, when generated from the piezoelectric material, goes through imaging tissues with different acoustic impedances. The amplitude of the reflection depends on acoustic impedance differences at the interface between different media. Each point in the image has a brightness which directly correlates to the amplitude of the reflection. This is the reason it is called a B-scan (brightness scan).

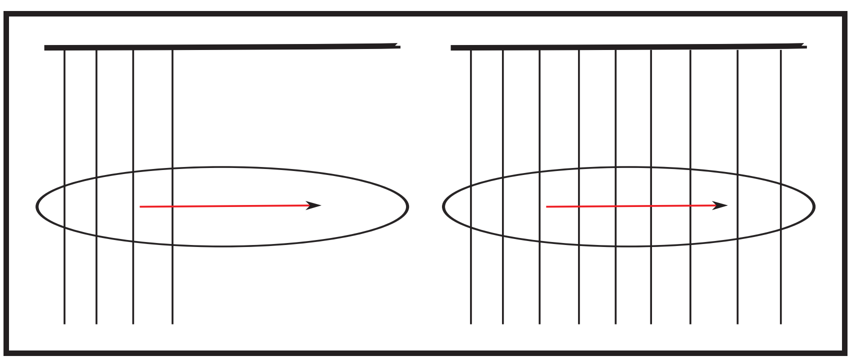

Figure 1.12 Formation of a 2D B-scan in which A-scans are placed side by side for multiple scans, this figure was adapted from (Hoskins *et al.*, 2010).

There are two kinds of imaging techniques mostly used in medical ultrasound: one is classic focused imaging and another one is plane wave imaging as shown in Fig. 1.13. The principle behind these two ultrasonic imaging techniques is to use the delays from the target insonated by ultrasonic waves to calculate the distances and therefore reconstruct an image. In ultrasonic imaging, axial resolution is the ability to distinguish two nearby targets which are in the direction of the US beam. For a distance d_0 between two targets, the difference in distance travelled by the wave to reach the transducer after its reflection is $2d_0$. Therefore, the axial resolution of an ultrasonic image is given by Eq. 1.12.

$$R_{axial} = \frac{N_{cycles} \cdot \lambda}{2} \tag{1.12}$$

where N_{cycles} is the number of cycles of the ultrasonic pulse and λ is the wavelength. So, as the frequency decreases λ decreases and also the resolution. The axial resolution also depends on the pulse length; lower the pulse length, the better is the axial resolution. Lateral resolution is the ability to distinguish the target perpendicular to the direction of propagation of the US. The lateral resolution is determined by the width of the US beam, in the far field the US beam is increasing and the lateral resolution is decreasing.

1.6.1 Classical focused imaging

With focused imaging, a series of waves is emitted at a predetermined depth by activating a set of elements of the probe. The delays are applied to each element individually to form constructive interference and concentrate the energy at the focal point. To obtain a complete image reconstruction in successive columns, the process is repeated with different groups of elements. The number of activated elements depends on the focal number (F) that was chosen, which represents the ratio between the depth of focus and the selection of the elements of the probe for an emission as shown in Fig. 1.13 (a). The focal point of focused imaging has the best lateral resolution because at this point the width of the beam generated by the selected elements of the probe becomes a minimum. Dynamic focusing overcomes this limitation, which consists of successive emissions with different focal points. As a result, the number of transmissions increases and the frequency of imaging must be lowered. A low imaging rate is associated with aliasing in fast moving particles as shown in Fig. 0.1. Since aliasing occurs with TCD systems, the FV cannot be accurately recorded. To reconstruct the image, the most common algorithm

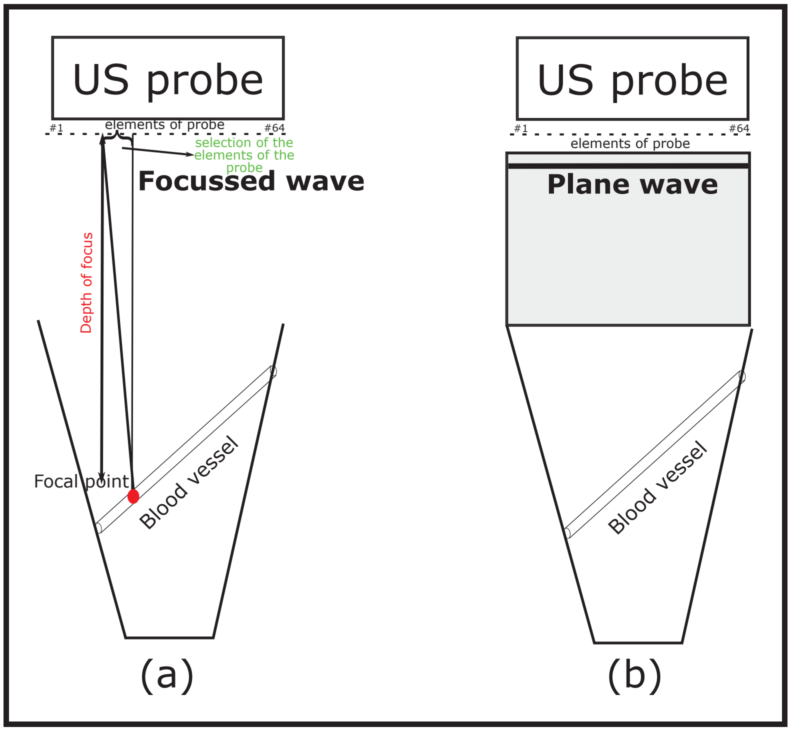

Figure 1.13 Diagram showing focused and plane wave imaging. Figure (a) shows in conventional focused imaging, ultrasonic waves are emitted and received from each element of piezoelectric probe and focused on a point in the ROI. Figure (b) shows in plane wave imaging, ultrasonic waves are emitted and received on all the elements which covers the ROI in just one emission as compared to the focused which takes emission equaled to the number of elements in a probe.

used is called "Delay and Sum" (DaS) (Montaldo, Tanter, Bercoff, Benech & Fink, 2009) as shown in Fig. 1.14.

Focused imaging is the most common imaging method in TCD. Doctors in TCD adjust the focusing depth, in order to capture the complete imaging object (Blanco & Abdo-Cuza, 2018a) which in turn can create aliasing problems for blood particles moving with high FV.

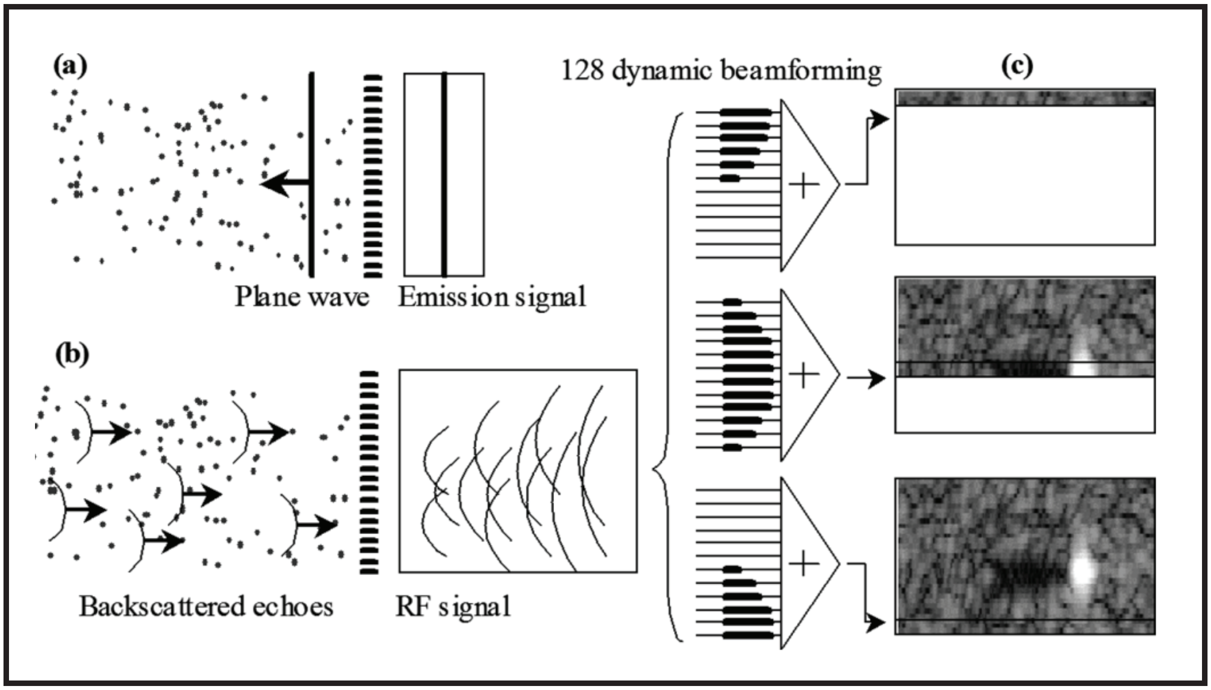

Figure 1.14 DaS method used by the emission of plane waves. As shown this image is reconstructed by columns successively. Image taken from (Montaldo *et al.*, 2009)

1.6.2 Plane wave imaging

The ultrasonic plane wave imaging technique was designed to maintain a high sampling frequency and to prevent spectral aliasing. This principle involves activating all elements of the probe simultaneously to produce an unfocused plane wave that will characterize each emission as shown in the Fig. 1.13 (b). The sampling frequency is therefore limited only by the imaging depth, $F_{samp}=\frac{c}{2d_{max}}$, where c is the speed of sound in the medium and d_{max} is the maximum imaging depth. In contrast to focused imaging, the factor that makes it an improvement is that it can acquire an object with only one emission. A review of the applications of the plane wave sequence is proposed by (Tanter & Fink, 2014; Tiran, Deffieux, Correia, Maresca, Osmanski, Sieu, Bergel, Cohen, Pernot & Tanter, 2015)

Initially applied for B-mode imaging, it was later developed for elastography (Sandrin, Catheline, Tanter, Hennequin & Fink, 1999), then for vector Doppler imaging (Udesen, Gran, Hansen, Jensen, Thomsen & Nielsen, 2008). The algorithm was originally developed for linear probes.

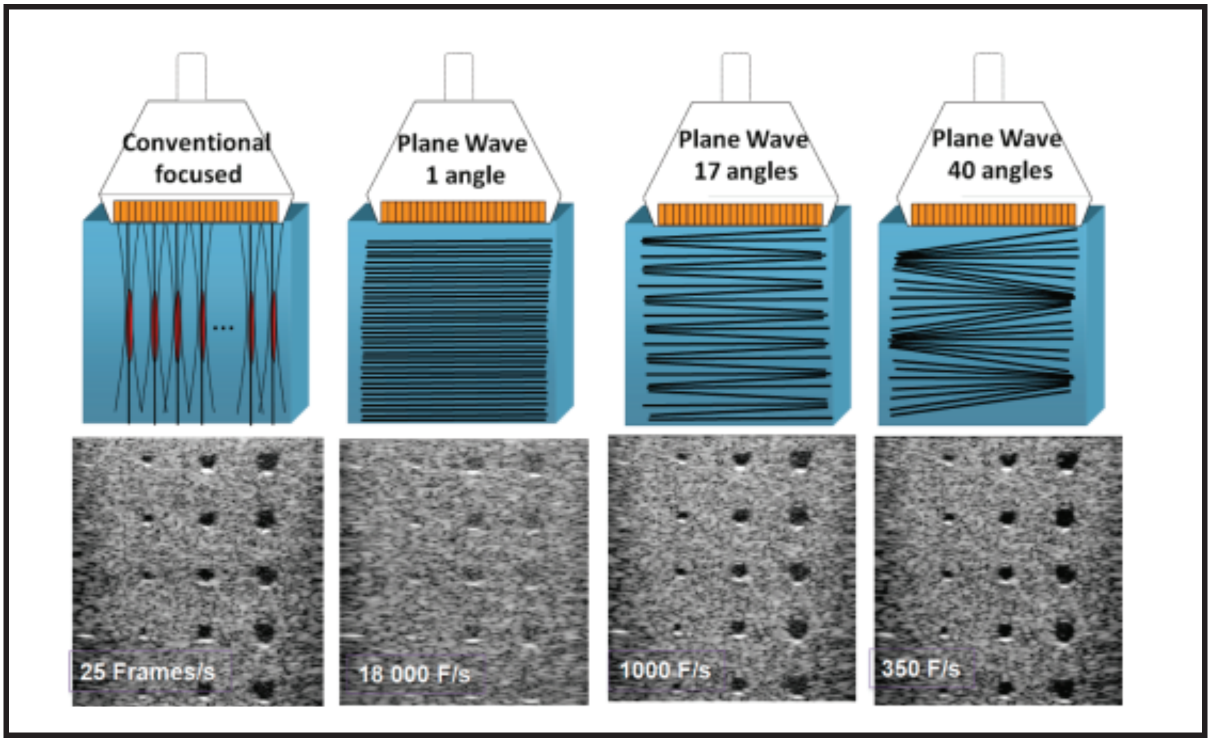

Figure 1.15 Reconstruction of a B-mode image from focused imaging and plane wave imaging for 3 different angles. The frame rates in plane wave imaging can be adjusted according to the number of angles used. Image taken from (Montaldo *et al.*, 2009)

To reconstruct plane wave images, there are many algorithms available (Besson, Zhang, Varray, Liebgott, Friboulet, Wiaux, Thiran, Carrillo & Bernard, 2016; Couture, Fink & Tanter, 2012; Tong, Gao, Choi & D'hooge, 2012). A single plane wave, however, results in a poorer image quality than focused imaging, so multiple plane waves are combined to get the final image. For this, the use of several plane wave emission angles, a sequence called "compounding", has been proposed by (Montaldo *et al.*, 2009). One advantage of multi-angle plane wave imaging is the adjustment of the frame rate, which can be used to our advantage when dealing with the variable particle velocity. Faster velocity means high frame rate, for which only few angles should be used, though it will compromise the imaging quality. For lower velocities, a lower frame rate can also work, so more angles can be used, thereby improving the quality of the image. The SNR comparison between focused and plane wave compound imaging was done by (Bercoff, Montaldo, Loupas, Savery, Mézière, Fink & Tanter, 2011). Focused imaging has a SNR close to plane wave compound imaging at the focus point and progressively degrades as the imaging depth goes away from the focal point. Planar imaging had an advantage over focused imaging by approximately 10 dB in the best case and by 2 dB near the focal point. During plane wave imaging, image reconstruction is carried out by following the DaS procedure discussed in Section 2.6.1. DaS works by calculating the total distance travelled by the wave between its transmission and reception as shown in a schematic diagram in Fig. 1.16, which is also described by the following Eq. 1.13, and is based on geometric considerations (Montaldo *et al.*, 2009):

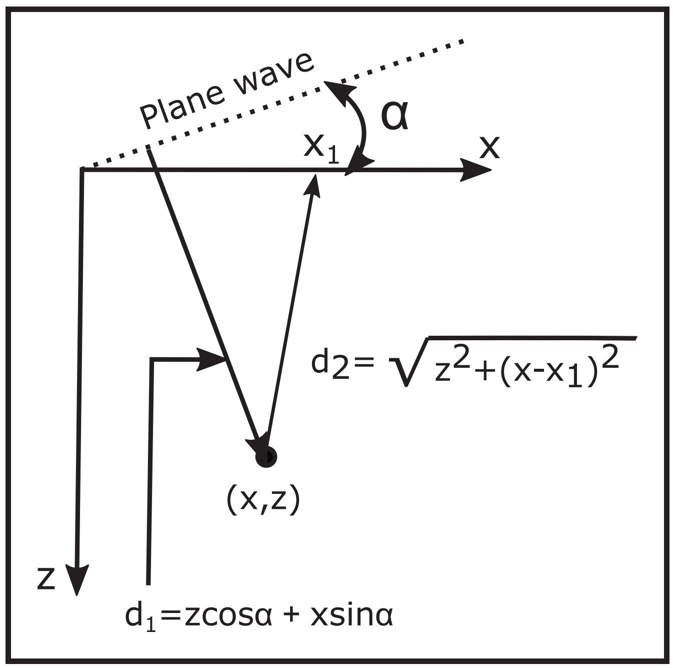

Figure 1.16 Figure shows the distance traveled by the ultrasonic wave between its transmission and emission with a plane wave of angle α. The calculated distance is used for time delay which is further used for plane wave imaging algorithm. This figure was adapted from (Montaldo *et al.*, 2009)

$$d = z\cos(\alpha) + x\sin(\alpha) + \sqrt{z^2 + (x - x_1)^2} \tag{1.13}$$

Where x and z represent the position of the pixel to be reconstructed in the axis of the probe and in the axis of depth respectively, α is the angle of the emitted plane wave with respect to the surface and x_1 is the position of the probe element used for the reconstruction. In addition, for each pixel location travelled time t_i^{xy} from the probe to the pixel and then back to the probe again is calculated. By applying the DaS procedure, an image is formed when each signal is delayed, squared, and averaged based on the calculated time and distance at each pixel location. Currently, clinical devices employ a focused algorithm detailed in the previous sections, and the implementation of the algorithm by plane waves would require a complete reorganization of the sequence. Many applications of plane wave imaging to Doppler imaging have been proposed. In particular, (Udesen *et al.*, 2008) used plane wave emissions for vector Doppler imaging, which makes it possible, in addition to color Doppler imaging, to visualize velocity vectors and therefore a precise direction of flow.

Due to the aforementioned advantages in the terms of SNR, aliasing problem and flexibility in adjusting the image quality, this thesis focuses on the plane wave imaging. However, using plane wave imaging also comes at a cost. US probes used in TCD imaging has a very small aperture which directly correlates to a small field of view. In this small field of view, it is possible that the vessels would not be directly insonified by plane waves, so in that case multi angle plane waves must be used to cover the field of view.

1.6.3 Doppler processing

A typical received A-scan from a TCD system is shown in Fig. 1.18. Looking closely at the figure, there are blood reflections which are surrounded by the vessel walls and a situation may arise when reflections from these walls are very low, such that it becomes difficult to separate the blood flow region from vessel walls as shown in Fig. 1.18b. This problem was first investigated by (Thomas & Hall, 1994). Filtering techniques were used to estimate the Doppler shift from the vessel wall signal and shift them to zero frequency. A high-pass filter is used which cancels vessel wall frequencies and estimates velocity. Though this method applies to cardiac signals, it can easily be adapted to our study in order to process A-scans.

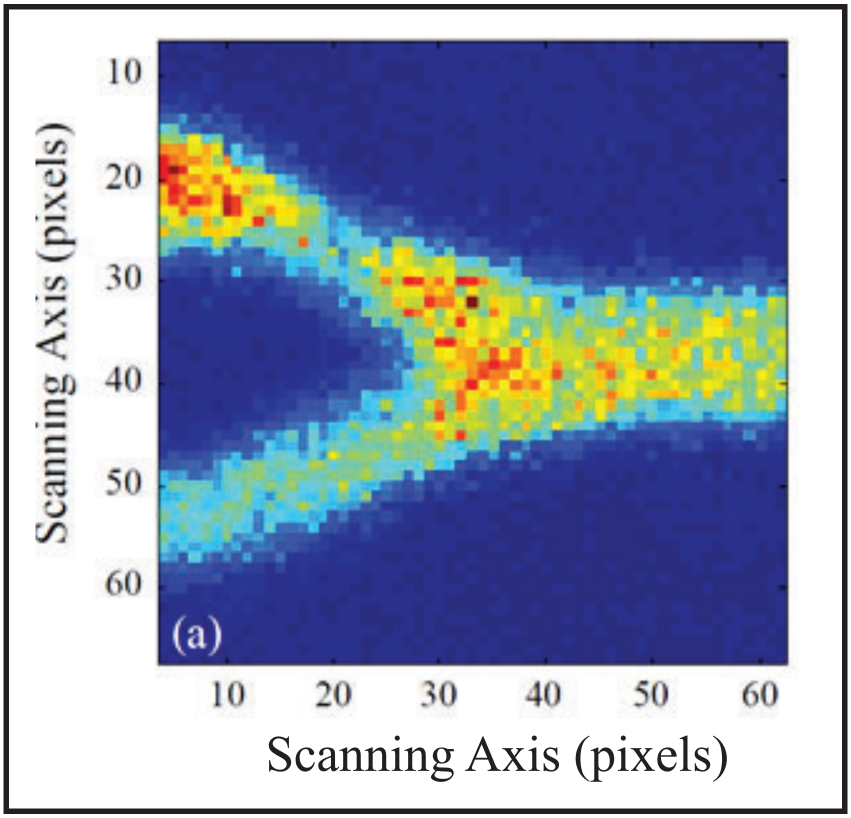

Figure 1.17 x and y axis represents the scanning axis. Figure showing the blood flow region in a Y-shaped Doppler phantom using processed A-scans and was directly taken from (Sadler *et al.*, 2013).

The most basic technique to process the received A-scan for estimating the blood flow is the very famous autocorrelation technique. (Kasai, Namekawa, Koyano & Omoto, 1985) use the power spectrum of autocorrelation function to determine the mean Doppler frequency shift and use Eq. 1.11 to determine FV. This technique is still in use and will be helpful in our case to reconstruct the Doppler image. (Sadler *et al.*, 2013) studied imaging blood flow using signal processing techniques for 2.5 MHz frequency range. In (Sadler *et al.*, 2013) the blood flow is detected by using the reflections from the blood scatterers. This method relies on detecting the temporal changes in A-scans, imaging the blood flow region and eliminating static components like vessel walls. This process is analyzed over multiple A-scans which allows an image of the blood flow to be obtained. The obtained image with this method looks like Fig. 1.17. Another

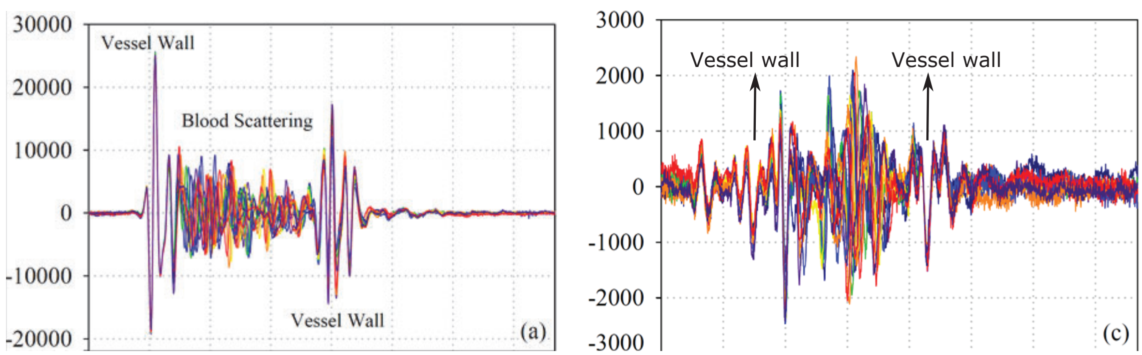

a) Transcranial Doppler A-scan with visible vessel walls

b) Transcranial Doppler A-scan attenuated vessel walls

Figure 1.18 (a) Figure showing A-scan with strong reflections from the vessel walls, blood scattering is clearly seen to be confined within this region (Baradarani *et al.*, 2014). (b) Figure showing A-scan with weaker reflections from the vessel walls, which makes it difficult to separate vessel wall from blood reflections(Baradarani *et al.*, 2014). This figure is directly taken from (Baradarani *et al.*, 2014)

study (Robins, Leow, Chapuis, Chadderton & Tang, 2017) used contrast agents while using two probes (one high frequency (1 MHz - 4 MHz) and another one low frequency (2 MHz - 4 MHz)) to increase the SNR of the Doppler signal. While this study suggests the method to overcome the effect of attenuation, but the study was performed on rats whose bone thickness was small, so to adapt this concept for the human skull using the mentioned frequencies would be difficult due to the high attenuation of the human skull. The method used to the Doppler signal and calculate FV in this thesis is adapted from the work of (Errico, Osmanski, Pezet, Couture, Lenkei & Tanter, 2016). In this work they compared plane wave vs focused Doppler imaging. However, instead of reconstructing an angle wise Doppler image and then do the compounding, they did the compounding of angles first and then reconstructed the Doppler images. The problem with this approach is Doppler shift information from each angle can get mixed with each other and create aliasing. Instead, FV information for each angle should be computed first and then compounding should be performed.

1.7 Ultrasonic wave propagation through irregular bone surfaces

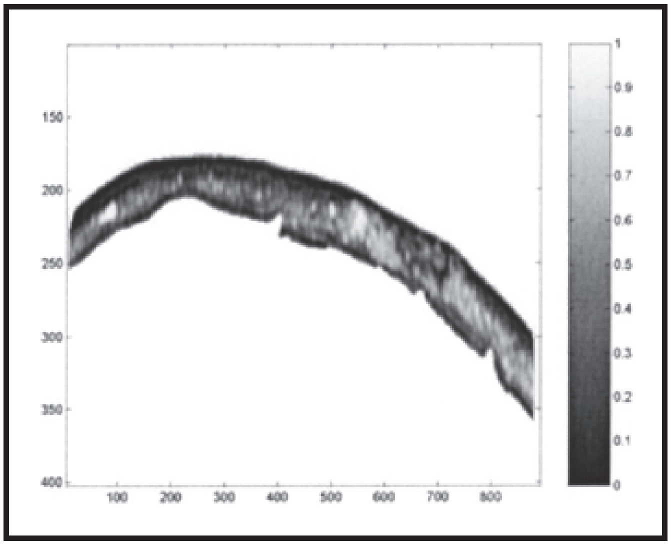

Figure 1.19 Porosity map of a slice derived from CT values where x-axis and y-axis represents pixel values (Aubry *et al.*, 2003). This figure was directly taken from (Aubry *et al.*, 2003)

The skull has an irregular surface as shown in Fig. 1.19. This irregularity is always present therefore distorting ultrasonic waves propagating through it. This distortion will cause poor transmission through the skull, and it is important to study its effects on SNR.

Apart from the time reversal technique, previous research did not consider the reduction of ultrasonic transmission because of the distortion of plane wave caused by the irregularity of the skull surface. Due to the skull curvature, ultrasonic waves were scattered in different directions and transmission loss happens. (Kwon, Kim, Kang, Bae & Kwon, 2006)

While the loss in the transmitted energy due to the external geometry of the skull has been ignored in the TCD literature, there is some literature in nondestructive testing (NDT) which considers the interaction of US plane waves with irregular surfaces (Robert, Casula, Roy & Neau, 2012). These methods are slow, as it requires individual transmission from piezoelectric elements from the ultrasonic probe. This slow process will cause aliasing in the TCD application. Another method is surface adaptive ultrasound (SAUL) (Hopkins, Brassard, Neau, Noiret,

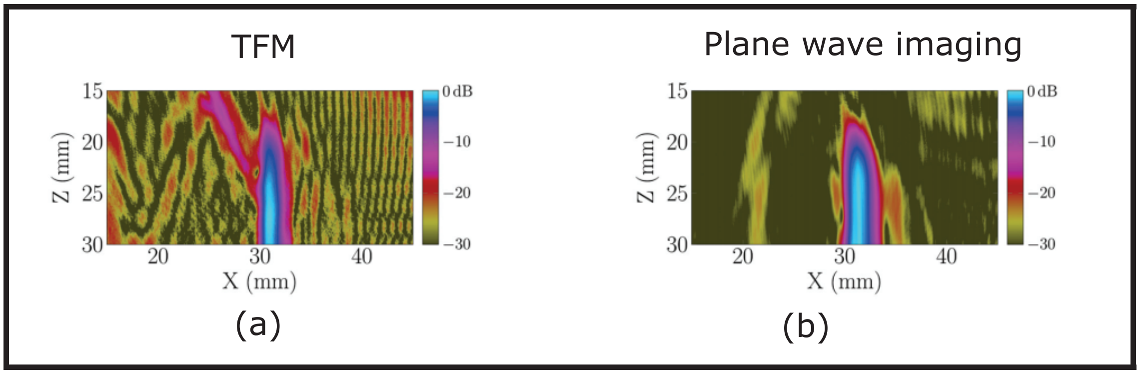

Figure 1.20 Figure showing imaging comparison between TFM and plane wave imaging. This image shows a vertical notch which is imaged using TFM and plane wave. Plane wave imaging was performed using only 4 transmissions as opposed to TFM which took 64 transmissions. SNR level in plane wave image is better than TFM. This figure was directly taken from (Le Jeune *et al.*, 2016)

Johnson & Le Ber, 2013) which requires much fewer firings of the element as compared to the previous technique. This is an iterative technique in which plane waves are emitted 4-5 times to calculate the surface profile. There is another interesting study related to SAUL which investigates a plane wave imaging under a complex surface (Le Jeune *et al.*, 2016). This study compared the total focusing method (TFM) and plane wave imaging. It was shown in this study that synthesizing a multi-angle plane wave beyond the complex surface enhanced the SNR of the images. The reason being plane waves are less sensitive to noise and attenuation because of their high amplitude as compared to the cylindrical waves used in TFM as shown in Fig. 1.20. Since in TCD it is not possible to compensate for each irregular surface along the propagation path, this thesis will explore the possibility of compensating only the outermost surface of the bone.

CHAPTER 2

EFFECT OF THE ACOUSTIC IMPEDANCE MISMATCH AS A FUNCTION OF FREQUENCY IN TRANSCRANIAL ULTRASOUND: A SIMULATION AND IN-VITRO EXPERIMENTAL STUDY

2.1 Introduction

As discussed in the literature review, the problem with TCD lies in the low ultrasonic energy penetrating inside the brain through the skull which leads to low SNR ratio. This is due to several effects including phase aberration, variations in the speed of sound in the skull, scattering, the acoustic impedance mismatch and absorption of the three layer medium made up of soft tissues, the skull and the brain. The acoustic impedance mismatch effect based on soft-tissue and bone interaction has typically been ignored in the literature. The aim of this chapter is to study the effect of transmission losses due to the acoustic impedance mismatch on the transmitted energies as a function of frequency. Understanding from this chapter will give better insight to the transmission of energy in the case of TCD.

2.2 Materials and Methods

2.2.1 Analytical model

An analytical model (Hill & El-Dardiry, 1980) for which a schematic description is presented in Fig. 2.1 was used to simulate the acoustic energy transmission as a function of the frequency in a multi-layer transcranial acoustic wave propagation transmission model. This chapter is focused on plane wave transmission to eventually use plane wave Doppler imaging (Mansour, Poepping & Lacefield, 2016). Though most clinical systems use focused ultrasound for Doppler measurements, plane wave TCD imaging is proposed due to its capability to acquire fast velocity information without aliasing. Clinical systems such as the Aixplorer (Couade, 2016) are now starting to offer plane wave imaging due to its superior frame rate. Therefore, a longitudinal plane wave is generated from a piezoelectric element, travelling from left to right through a

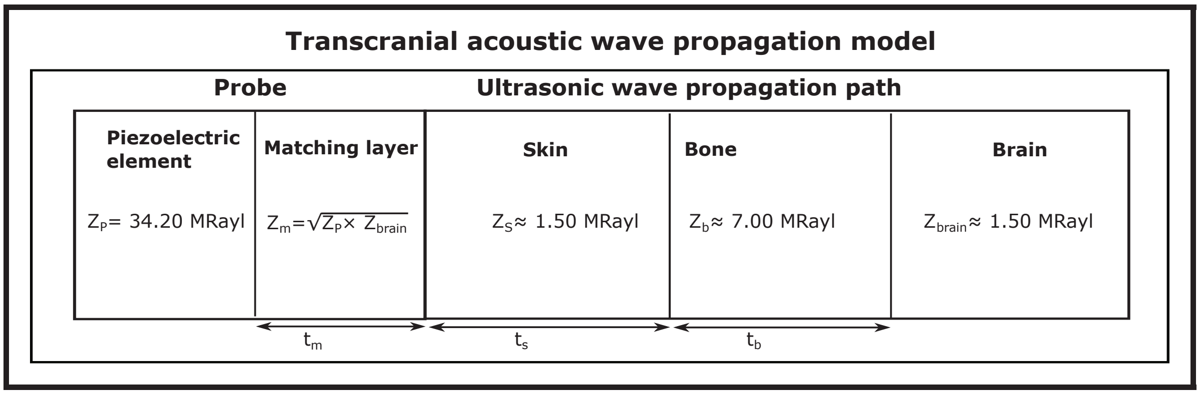

Figure 2.1 A one-dimensional acoustic wave propagation model for TCD. Z_x is the acoustic impedance and t_x is the thickness in layer x.

series of layers with different acoustic impedances Z. The plane wave interacts with layers causing multiple reflections and transmissions until a transmitted wave reaches the brain. The brain and piezoelectric crystal layers are assumed to have a semi-infinite thickness.The acoustic impedances of the piezoelectric element, the matching layer, the skin layer, the bone, and the brain are Z_p (34.20 MRayl), Z_m (7.10 MRayl), Z_s (1.50 MRayl), Z_b (7.00 MRayl), and Z_{brain} (1.50 MRayl) respectively (Cheeke, 2002). Since the brain consists mainly of water, an acoustic impedance of 1.50 MRayl was assumed. The skin's acoustic properties also matches very closely with water (Ludwig, 1950). While, the absorption of skin due to scalp tissue (Shankar & Pagel, 2011) is significantly different from that of water, the effect of absorption would remain almost constant for the given small range of frequencies typically identified as optimal. The acoustic impedance in skin was shown to vary within a narrow range (Ludwig, 1950). However, the acoustic impedance of the human skull was shown to vary significantly (Fry & Barger, 1978). Although the bone acoustic impedance was constant at 7 MRayl in this work, the concept of adapting the centre frequency of the transmitted signal to acoustic impedances of the layers along the wave propagation path is of interest. The thicknesses of the matching layer, the skin, and the bone are t_m, t_s, and t_b respectively. The matching layer thickness was considered to be $\lambda/4$ at a centre frequency of 3 MHz for a 2-4 MHz probe and 1.50 MHz for a 1-2 MHz probe. However, the thickness of skin and bone do vary in the literature (Mahindra & Murty, 2009; Seidenari & Giovanni, 1999), which motivates the study presented in this chapter. The assumed speed of sound in the piezoelectric element layer, the matching layer, the skin layer and the bone layer is 4500 m/s, 3310 m/s for a 2 MHz-4 MHz probe and 2000 m/s for 1-2 MHz probe (provided by the manufacturer), 1500 m/s and 3000 m/s (provided by the manufacturer) respectively. To predict the energy inside the brain based on different thicknesses and acoustic impedances, the classical transmission matrix method was used (Hill & El-Dardiry, 1980). If a layer has a thickness t_l and acoustic impedance Z_l, the transmission matrix is given by

$$\begin{bmatrix} T_l \end{bmatrix} = \begin{bmatrix} \cos\theta_l & iZ_l \sin\theta_l \\ i \sin\theta_l / Z_l & \cos\theta_l \end{bmatrix},$$

where $\theta_l = 2\pi t_l / \lambda_l$, λ_l is the wavelength and t_l is the thickness of the l_{th} layer. The equivalent acoustic impedance of the model is (Z_{eq}) which considers the acoustic impedance of piezoelectric element:

$$Z_{eq} = \frac{T_{11} \cdot Z_p + T_{12}}{T_{21} \cdot Z_p + T_{22}}, \tag{2.1}$$

where $T_{mn}, m, n \in \{1, 2\}$ are the elements of a transmission matrix T_x representing a multi-layered structure consisting of a matching layer, a skin layer and a bone layer. T_x is given by:

$$\begin{bmatrix} T_x \end{bmatrix} = T_1 \cdot T_2 \cdot T_3 = \begin{bmatrix} T_{11} & T_{12} \\ T_{21} & T_{22} \end{bmatrix}$$

where 1,2,3 represents the matching, the skin and the bone layers. For a given TCD wave propagation model, transmission coefficients are calculated. The coefficients of the reflected and transmitted waves in the brain are given by:

$$R = \left[\frac{|Z_{eq} - Z_{brain}|}{|Z_{eq} + Z_{brain}|} \right]^2 \tag{2.2}$$

and

$$T = 1 - R. \tag{2.3}$$

For maximum energy transmission, $R = 0$, and $T = 1$; i.e., Z_{eq}=Z_{brain} in equation 2.2. In the case of TCD, this situation can happen when the thickness of the matching layer $\lambda_m/4$ is followed by skin and bone thicknesses of $t_s = \lambda_s/2$ and $t_b = \lambda_b/2$ respectively. (λ_m, λ_s, λ_b are the wavelengths in the matching, the skin and the bone layers respectively). Thus, certain combinations of frequency, skin layer thickness, bone thickness and matching layer thickness lead to better energy transmission than others. The most obvious parameter to tune in a practical situation where different patients are seen would be the frequency. Therefore, the analytical simulation was run using equations 2.1, 2.2, 2.3 which provided the transmission coefficients for different bone, skin and matching thicknesses as a function of frequency. The energy propagating back to the probe from a reflector is of interest and is also calculated using equations 2.1, 2.2, 2.3.

The transmission coefficients received from the analytical model were based on the assumption that the input excitation signal is a sine wave of a single frequency leading to an infinite signal in the time domain. In practice, the signals are finite in the time domain. To overcome this effect:

1. A transmitted energy coefficients curve is calculated for different skin layer thicknesses as a function of frequency based on the analytical model.

2. To find the transmitted energy of a finite time domain signal, a 10-cycle Tukey-windowed tone burst sampled at 10 MHz is simulated as an excitation signal. A narrow band 10-cycle waveform was chosen since this is the typical length of the waveform used in color Doppler imaging. The power spectrum of the input signal and transmission coefficient spectrum are multiplied to provide the transmitted energy spectrum;

3. The transmitted energy spectrum is multiplied by the attenuation curve which is proportional to the frequency squared and is derived using (30 dB/cm @2.25 MHz Wydra & Maev (2013) in the case of the bone phantom plate used in the experiments. The attenuation at 2.25 MHz was supplied by the manufacturer of the phantom). It was assumed that the attenuation was constant in the skull layer and the value of attenuation was extrapolated for different centre frequencies ranging from 1 MHz-4 MHz. The absorption was not considered in

the modeling since it would unlikely change the optimal frequency with respect to the acoustic impedance mismatch due to skin layer thickness. Across the small range of optimal frequencies obtained from the model, the absorption would be almost constant.

4. Reflected energy is calculated all the way back to the piezoelectric element from an aluminium plate with a reflection coefficient of 86% Cheeke (2002).

The final spectrum gives the reflected energy with respect to the input signal which includes the combined effect of attenuation and the acoustic impedance mismatch. This step is repeated for different skin layer thicknesses varying from 1 mm to 2 mm for a constant bone thickness of 4.40 mm giving a 2D map as shown in Fig. 2.2 (a) and (b) as a function of the centre frequency (1 MHz - 3 MHz). The experimental validation was limited to a constant bone thickness of 4.40 mm which is also in the range of the average human temporal bone thickness (Mahindra & Murty, 2009), with centre frequencies ranging from 1-2 MHz and 2-3 MHz. The two sets of frequencies were chosen to perform simulations and experiments. Lower frequencies were chosen as it was suggested in the literature that TCD imaging performs better in lower frequency ranges. The second set was chosen because the typical frequency range used for TCD is between 2-2.5 MHz. The water layer (which mimics acoustic properties of skin) thickness was kept between 1 mm to 2 mm since the average skin thickness of a human being near the temporal window is 1.85 mm (Seidenari & Giovanni, 1999). Fig. 2.2 (a) and (b) were used for the comparison in the next sections to compare analytical and experimental results.

2.2.2 Experiment

To validate the analytical model, an experimental setup was devised. Fig. 2.3 shows the different components which were used to make the setup. A corner bracket was used to hold a linear positioning stage (Velmex A1503P20-S1.5, 0.025 mm resolution) vertically. The probe holder was fixed to the adapter using set screws. The Verasonics P4-2v probe was connected to the Verasonics V1 phased array controller and could be moved vertically using the linear stage. The whole assembly was immersed in a water tank, which also contained a bone phantom plate Wydra & Maev (2013) made up of a ceramic material mimicking the acoustic properties v_l:

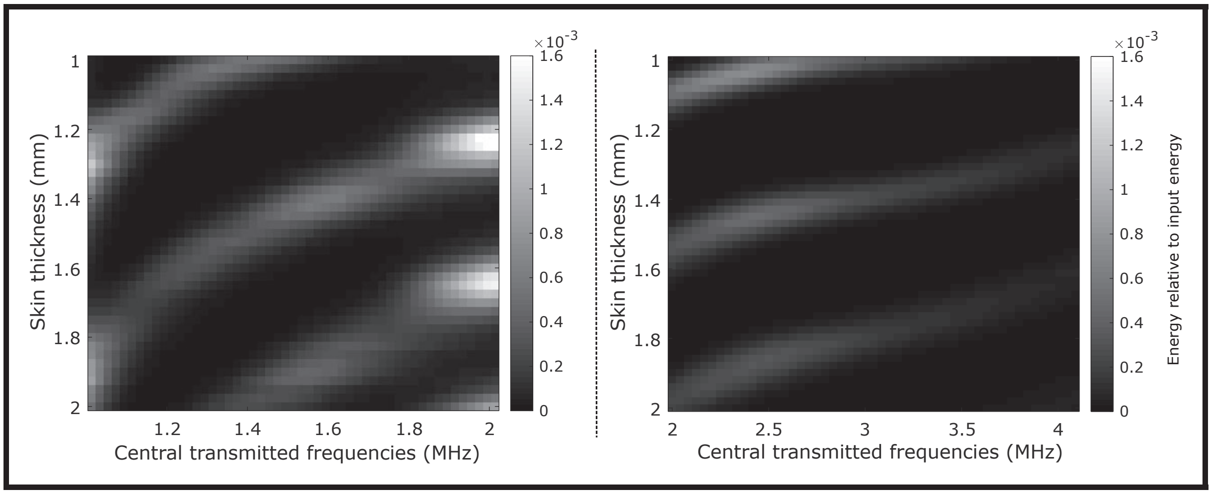

Figure 2.2 (a) Received energy as a function of skin layer thickness varying from 1 mmto 2 mm and central transmitted frequencies varying from 1 MHz to 2 MHz. The reflection is caused by an aluminium plate 3 cm from the bone surface. (b) Received energy as a function of water layer thickness varying from 1 mm to 2 mm and frequencies from 2 to 3 MHz. Both 2D maps were obtained from simulations.

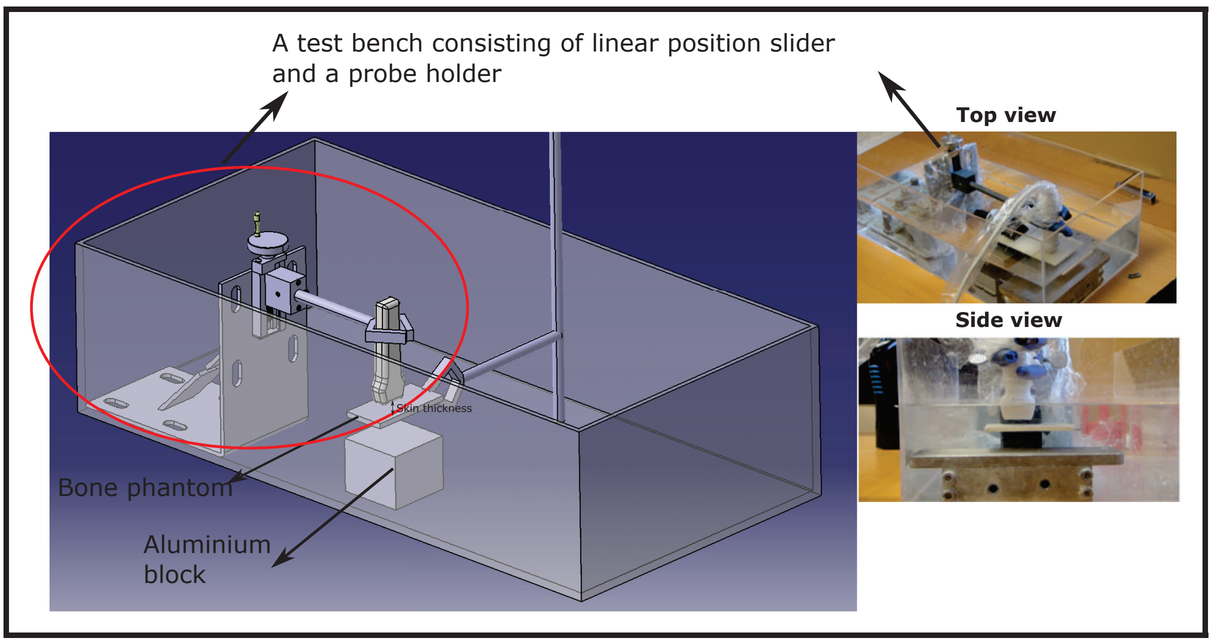

Figure 2.3 The experimental setup comprised of a linear positioning stage to hold an ultrasonic probe, a bone phantom plate which mimicked the acoustic properties of the skull, water which mimicked the skin's acoustic properties and an aluminium block which was used as a reflector.

3000 m/s, ρ: 2100 kg/m^3 - the cortical layer of the bone phantom can be assumed homogeneous. However, the trabecular bone layer contains voids and inclusions to increase its attenuation. The total attenuation of the bone phantom plate is 30 dB/cm @ 2.25 MHz of the skull. The bone phantom plate thickness was 4.40 mm. An aluminium block was chosen as a reflector at a distance of 3 cm from the bone surface. The tank was filled with water to mimic the skin's acoustic impedance. The experiments were conducted using a Verasonics V1 system Khalitov, Gurbatov & Demin (2016). The frequency range of the P4-2v probe was 2 MHz-4 MHz with the centre frequency at 3 MHz. This probe had 64 elements which were simultaneously activated to approximate a plane wave. The experimental procedure was repeated for the 1.5L64-0.3x15 probe manufactured by Guangzhou Doppler Electronic Technologies Inc.. This second probe had a frequency bandwidth between 1 MHz and 2 MHz. In all cases, the transmitted waveform was a 10-cycle Tukey windowed tone burst. The initial position of the probe was marked at the top of the bone phantom plate and then it was moved up step by step, thus increasing the gap between the probe and bone phantom plate. This water gap mimics the skin thickness. A typical transmitted waveform without the bone phantom is shown in fig. 2.4 (a) A typical received waveform for a water layer thickness of 1 mm is shown in Fig. 2.4 (b). The probe was moved up in steps of 0.025 mm to acquire a measurement. The probe was moved upwards until the gap between the probe and the plate was 2 mm. In Fig. 2.4 (b), the received waveform acquired using the P4-2v probe contains a reflection from the top part of the bone plate and from the surface of the aluminium block. The reflected signal from the aluminium block is shown in the small box of Fig. 2.4 (b). The 10 cycles of the reflected signal were extracted. The input signal is the emitted signal from the phased array controller. The ratio of the reflected to input signal energy was calculated using equation 2.4

$$E_{brain} = \left| \frac{|\mathsf{FFT}(signal_{extracted})|}{|\mathsf{FFT}(input)|} \right|^2 . \tag{2.4}$$

This same calculation was repeated for the other input signal centre frequencies ranging from 2-3 MHz for the P4-2v probe and from 1 MHz to 2 MHz for the 1.5L64-0.3x15 probe. The variation of received energy as a function of the frequency for a water layer thickness of 1 mm is shown in

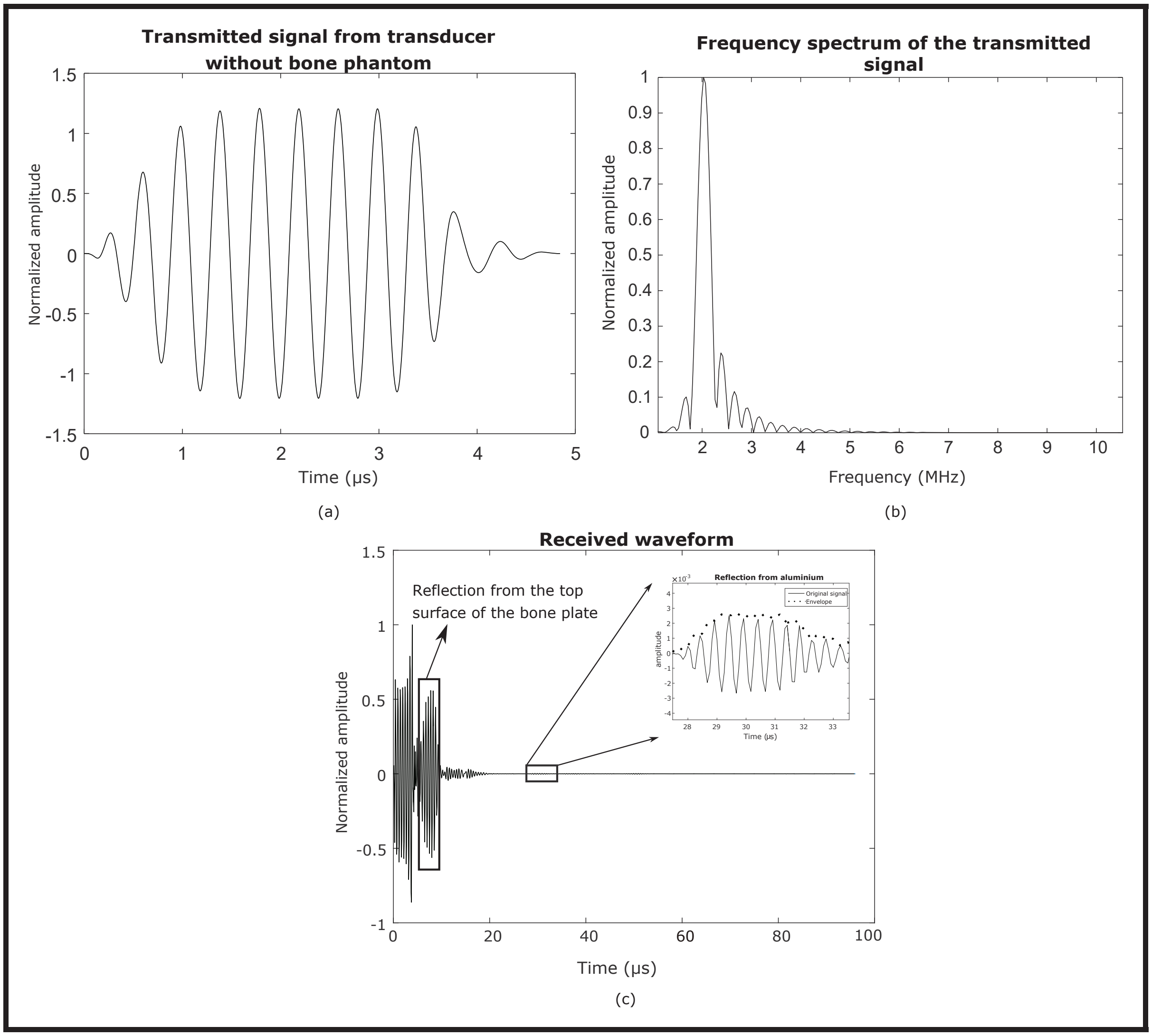

Figure 2.4 (a) A typical transmitted waveform for a frequency of 2 MHz without the presence of bone phantom. (b) Corresponding frequency spectrum of the transmitted waveform without bone phantom. (c) A time trace of a received waveform for a frequency of 2 MHz and a gap between the probe and the bone phantom plate of 1 mm. The figure also shows a reflection from the aluminium block along with the envelope.

Fig. 2.5. The same process was repeated for multiple water layer thicknesses varying from 1-2 mm keeping the bone thickness constant. This experiment provides a two-dimensional map, as shown in Fig. 2.6. The experimental setup and measurement process mimic the analytical model results with a constant bone thickness and water layer thickness varying from 1 mm to 2 mm.

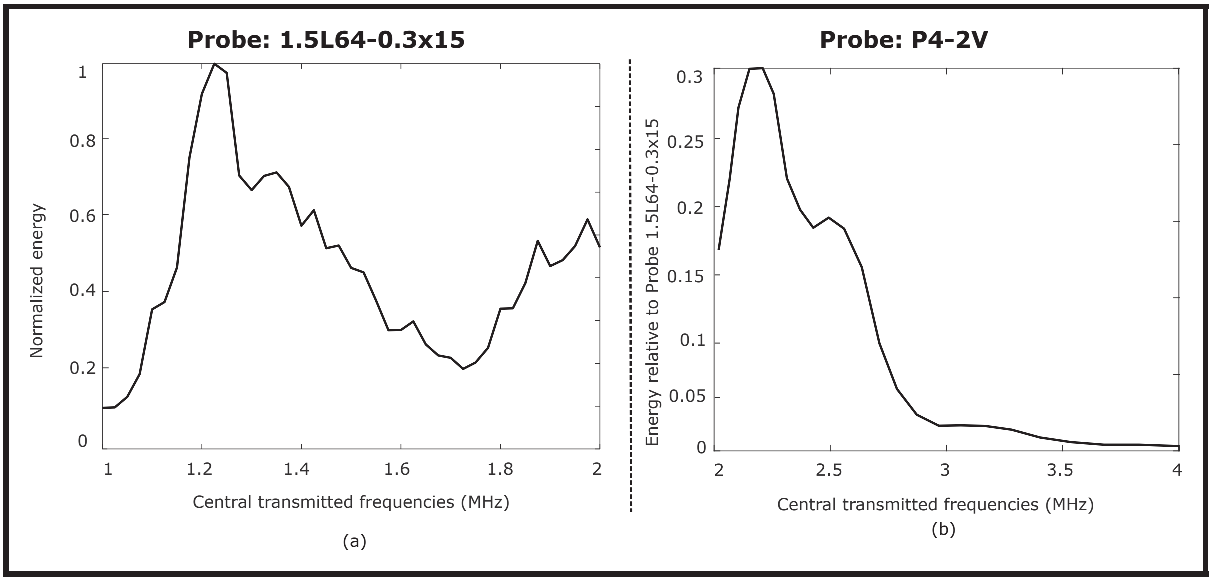

Figure 2.5 (a) Normalized experimental energy received as a function of the frequency for a 1 mm water layer thickness for probe 1.5L64-0.3x15. (b) Experimental energy received as a function of the frequency for a 1 mm water layer thickness for probe P4-2v relative to probe 1.5L64-0.3x15.

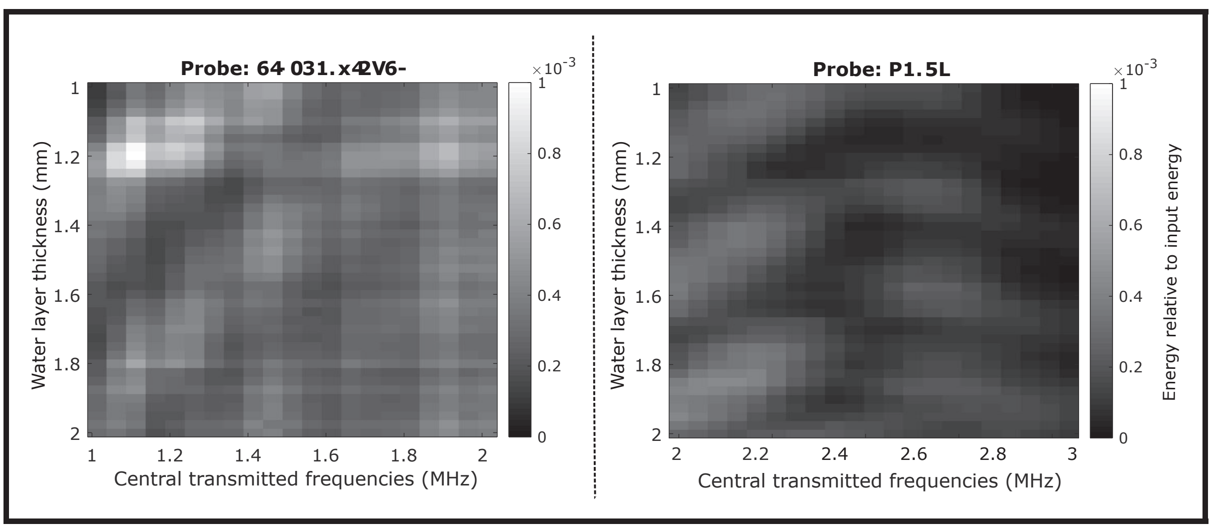

Figure 2.6 The experimental 2-D map shows the variation of received energies as a function of frequency and water layer thickness. The experimental result showed that there is an acoustic impedance mismatch effect as the intensities vary as a function of water layer thickness for a constant frequency.

2.3 Results

To look more closely at the comparison between the analytical and experimental results, narrow band signals with a centre frequency between 1.00 MHz to 1.19 MHz and 2.06 MHz to 2.26 MHz at regular intervals of 65 kHz were taken from the original data and overlaid on each other as shown in Fig. 2.7. Table 2.1 shows the correlation coefficient between the simulated and experiment results for the given frequencies, which was calculated according to

$$\frac{1}{n-1}\left(\sum_x \sum_y \frac{(x-\bar{x})(y-\bar{y})}{S_x S_y}\right), \tag{2.5}$$

where x and y are the two signals, $\overline{x}$ and $\overline{y}$ are the mean of the two vectors , S_x and S_y are the standard deviation of the two vectors and n is the length of the signals.

The table also contains the average local shift (the average water layer thickness difference) between simulation and experiment of the received energy maxima and its standard deviation. The difference between the position of the maximum amplitude between the experiment and analytical result was equivalent to an average of 0.06 mm error on the water layer thickness given a fixed bone thickness. The average correlation between the experimental and analytical result came out to be 0.50 for a high frequency probe and 0.78 for a lower frequency probe. The Average full-width at half maximum (FWHM) for experimental and analytical curves was calculated to show the extent of the spread of energy around the maximum. The average statistic was used because it summarized all the individual local shifts, standard deviation and FWHM into a single value, which made it easy to compare between all the curves. These results showed that the energies do depend on specific combinations of bone and water layer thicknesses as a function of the frequency.

2.4 Discussion

The aim of this chapter was to show the effects of the frequency-dependent acoustic impedance mismatch. By choosing the frequency that will enable the highest transmission of ultrasonic

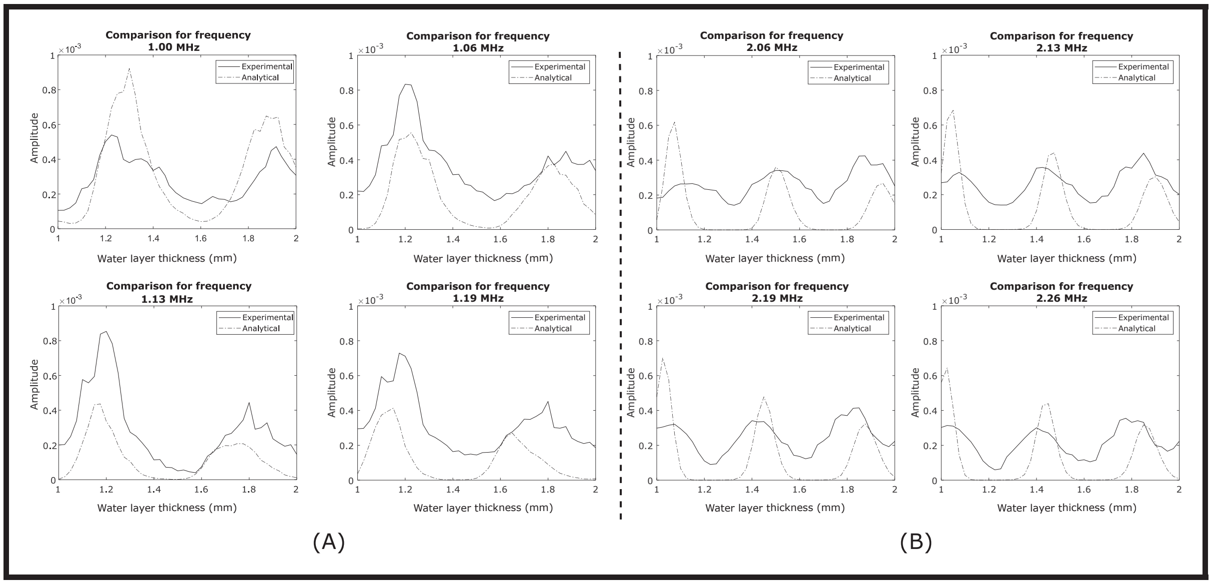

Figure 2.7 The multiple figures shows the comparisons between the selected frequencies ((A) being the results from probe 1.5L64-0.3x15 whose frequency spectrum lies between 1-2 MHz (B) being the results from the probe P4-2v whose frequency spectrum lies between 2-4 MHz) for received energies as a function of water layer thickness for experiment and analytical results.

Table 2.1 Comparisons between the selected frequencies of experimental and analytical image

Frequency (MHz)	Correlation coefficient	Average shift of maximums (mm)	Standard deviation of the shift of maximums	Average FWHM (experimental)	Average FWHM (analytical)
1.00	.72	.07	.04	.21	.15
1.06	.85	.05	.03	.30	.18
1.13	.86	.05	.04	.18	.19
1.19	.67	.10	.06	.15	.15
2.06	.38	.04	.04	.20	.15
2.13	.48	.06	.02	.19	.12
2.19	.55	.09	.06	.19	.11
2.26	.57	.06	.05	.20	.11

energy the chances of a successful measurement are higher. While there are effects like scattering, shear mode conversion and effects due to the heterogeneous internal structure of the temporal bone, these effects should have a uniform effect across the range of skin thicknesses and frequencies and will happen regardless of the chosen frequency. The results obtained shows that ultrasonic transmission in the frequency range of interest through the human skull is affected by the acoustic impedance mismatch and that the transmitted energy varies as a function of the

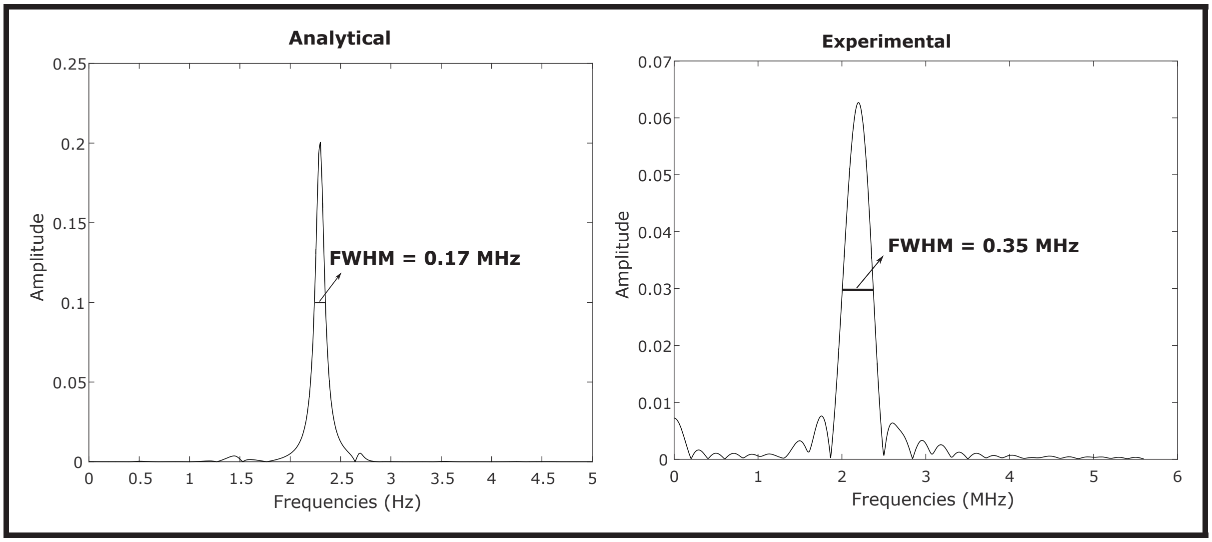

Figure 2.8 Frequency spectrum for a water layer thickness of 1 mm and a frequency of 2.20 MHz. The experimental frequency spectrum width is roughly double the analytical model spectrum. This widening of the frequency spectrum is correlated to the widening of the curves shown in Fig. 2.7 (B)

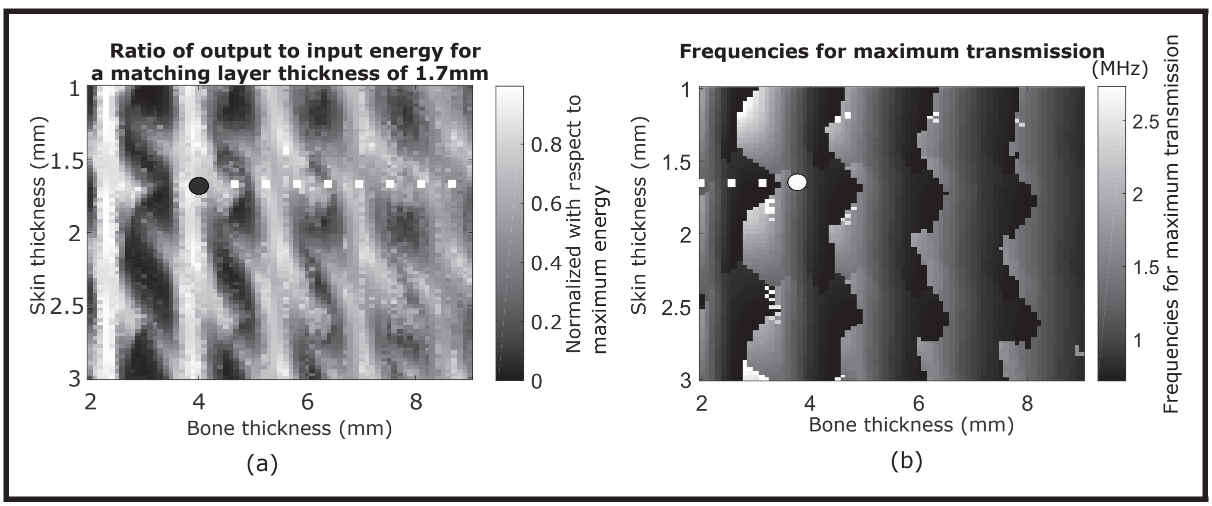

Figure 2.9 X and Y-axes in both the figure represents skin and bone thickness respectively. Figure (a) shows the corresponding transmitted energy for the measured thicknesses including attenuation of 30 dB/cm @2.25 MHz. Figure (b) shows the variation of optimized frequencies for different skin and bone thicknesses.

frequency, skin thickness and bone thickness. Transmitted energy for a typical combination of skin thickness and frequency may then lead to higher SNR.

The results show that the maximum received energy level is on the order of 10^{-4} times the input energy. With the current configuration it is not possible to transmit more than 20% of the incident energy. The reason is that incident pressure is inversely related to the square of acoustic impedance. So if ultrasonic wave starts from the piezoelectric domain and ends inside the brain incident pressure will be $\sqrt{(Z_{brain}/Z_p)}$ where Z_{brain} and Z_p are the acoustic impedances in the brain and the piezoelectric element respectively. That means:

$$p_{brain} = \sqrt{(1.50/34.20)}p_{incident}, \tag{2.6}$$

where $p_{incident}$ was arbitrarily set to 1 Pa, Z_{brain} is 1.50 MRayl and Z_p is 34.20 MRayl (Cheeke, 2002), which gives a maximum possible transmitted pressure of 0.20 Pa that in turn makes the maximum received pressure to be 0.04 Pa without including the attenuation effects. When including a linear attenuation factor for the bone, the received pressure level drops to 10^{-4} Pa.

The interesting features in the experimental map of Fig. 2.6 are the three local maxima occurring for any frequency between 2-3 MHz. As explained in section 2.2.1, a maximum transmission can occur if the thickness of the matching layer is $\lambda_m/4$ and is followed by the skin and the bone thickness of odd integer multiple of $\lambda_s/2$, $\lambda_b/2$ respectively. When using 2.26 MHz a local maximum at a water layer thickness of 1.51 mm can be seen. At this frequency if the matching layer thickness is $\lambda_m/4$, the water layer thickness becomes $\approx 5\lambda_s/2$ and the bone thickness becomes $\approx 7\lambda_b/2$ which are odd integer multiples of $\lambda/2$ therefore lead to a local maximum energy transmission. The same concepts can be applied for all frequencies. On the obtained maps it is seen that on the edge of the probe bandwidth, the transmission was reduced. It is due to the fact that the probe bandwidth is not flat and rather decreases in amplitude at the edges, so the signal transmitted after passing through the probe edges had decreased amplitude.

The average shift corresponding to the locations of the local maxima of the experimental and the analytical results fluctuated around an average of 0.06 mm for the selected four frequencies for both the probes with an overall standard deviation of 0.04 mm. Thus, the model was able to accurately predict the local positions of the maxima, with small differences due to experimental errors. However, a close analysis of Fig. 7 and Fig. 3 reveals that there is a deviation between the experimental results and the analytical results. This deviation is currently thought to be caused by the bone phantom attenuation increasing more than the predicted by assumed power law. The discrepancy between experimental and analytical results is reduced for the lower frequency probe, which supports, this interpretation. The overall correlation coefficient for the selected frequencies was 0.50 for a high frequency probe and 0.78 for a low frequency probe, showing a strong relationship between experimental and analytical results. The experimental curves are also wider than the analytical curves in the both the comparisons of Fig. 8 and this discrepancy is more pronounced for higher frequency probe. The reason for this widening is explained in Fig. 2.8, where FWHM of the experimental curve is roughly double that of the analytical curve for a selected water layer thickness of 1 mm and for a centre frequency of 2.20 MHz. The widening of the frequency spectrum directly leads to the widening of the curves in Fig. 2.7 since the ratio of the reflected to input energy is calculated based on these spectra. Physically, this means that the optimal frequency range is not as narrow as the prediction of the model. This also means there is no sudden drop of energy if the transmitted center frequency is little bit away from the optimal frequency, which is good for the practical implication of TCD.

To address the problem of using a fixed input signal for all situations, an analytical simulation was run, which gave an optimized two-dimensional map of water layer and bone thicknesses for which the frequency with the highest transmission was selected as shown in Fig. 2.9. This figure suggests that given measurements of skin (Seidenari & Giovanni, 1999) and bone thickness (Mahindra & Murty, 2009), an optimal excitation frequency could be selected to optimize ultrasonic transmission. The optimized 2D map obtained in Fig. 2.9 suggests that lower frequencies from 750 KHz to 1.7 MHz should be used depending on the combination of skin and bone thicknesses, which is in agreement with previous suggestions to use lower frequencies (Klötzsch *et al.*, 1998; Kollár *et al.*, 2004; Lindsey *et al.*, 2011; White, 1992; Yousefi *et al.*, 2009). The main limitation of this study is that it does not account for inhomogeneities, anisotropy and the difference between the inner and outer structure of the skull. One more limitation of this study is that the bone phantom was considered as a single layer rather than a multilayer system. This assumption was made since an average speed of sound for the whole phantom was provided by the manufacturer and not for the individual layers. Separating the bone into multiple layers would help modeling a more realistic overall impedance mismatch but was not feasible in this study. However, the experiment remains a valid proof of concept in a relatively simple scenario to isolate the impedance mismatch effect. Apart from the skin thickness, there will be a measurable thickness of connective tissue. The thickness of connective tissue will also play a role in determining the optimal frequency selection for the measurement, but in this study the connective tissue was neglected since the acoustic impedance of subcutaneous tissues is around 1.35 MRayl (Shankar & Pagel, 2011), which is similar to soft tissue/brain so that they would be nearly transparent to ultrasonic waves, and would not affect the propagation path in an adverse manner. However, one might make this model more complex by introducing this thickness. Also, this study considers only normal incidence and the effect of acoustic impedance mismatch according to the angle of entry still requires further study which will also increase the field of view. Furthermore, it is important to note that this study do not take into account effect of frequency selection due to the backscattering coefficient of the blood which increases with the frequency. Exploring these options will further enhance the knowledge related to ultrasonic transmission in the skull. These effects may change the optimal selection of frequency derived by the method. Therefore, evaluating the effectiveness of frequency optimization as suggested here would require more detailed studies and experiments.

Future work will primarily focus on validating the proposed choice of centre frequency based on acoustic impedance mismatch for Doppler measurements.

2.5 Conclusion

TCD is a method that is used to measure blood FV within the arteries located inside the brain but suffers from poor image quality due to less energy penetrating through the skull. The variation of ultrasonic transmission as a function of frequency was considered in this chapter and was due to (1) acoustic impedance mismatch and (2) attenuation. Although there are other important factors like phase aberration, scattering and diffraction inside the skull that affect transmission of ultrasound, these will affect all frequencies evenly. However by adapting the frequency to enable strong impedance matching a significant gain in transmitted energy can be achieved. In this chapter, a study was conducted that allows to understand how ultrasonic transmission is affected by the skin and bone thickness acoustic impedance mismatch effects. The study was performed by designing an analytical model which simulates US wave propagation from the piezoelectric element into the brain. The analytical model was validated using an experimental setup which comprised a bone phantom plate immersed in water, mimicking the acoustic properties of the skull. Comparison between analytical and experimental results, showed that the analytical model was able to accurately predict the occurrence of maximum energy transmission as a function of the frequency and the water layer thickness. The average water layer thickness difference between occurrence of maximum amplitudes was 0.06 ± 0.04 mm. Overall correlation coefficients of 0.50 and 0.78 showed a strong similarity between analytical and experimental results. More analysis indicated that an optimized frequency can be chosen depending on the measured bone and water thicknesses. This provides an opportunity to break the barrier of ultrasonic transmission through the skull.

CHAPTER 3

DOPPLER IMAGING THROUGH A BONE PHANTOM

3.1 Introduction

Blood flow imaging through the skull is one of the major goals of TCD. However, because of poor ultrasonic transmission through the skull, it is difficult to evaluate the blood flow in the vessels present inside the brain. The primary aim of this chapter is to calculate the blood mimicking fluid flow through a bone phantom without prior knowledge of the vessel diameter. The blood flow calculation depends on the Doppler effect as discussed in chapter 2. Doppler calculation in TCD relies on the scattering caused by the red blood cells. The resolution and image quality of Doppler US images in TCD are strongly affected by attenuation and the effect of acoustic impedance mismatch. Following on from the previous chapter, the major contribution of this chapter is to optimize the frequency based on acoustic impedance mismatch effect for Doppler experiments.

3.2 Materials and Method

The experimental setup for Doppler imaging is illustrated in Fig. 3.1. This setup comprised a blood vessel mimicking phantom as shown in the side view of Fig. 3.1, which was kept inside a cup to hold it. The blood vessel diameter was 2 mm with wall thickness varying from 0.5 mm to 1 mm. These numbers were provided by the manufacturer (True phantom solutions inc.). Sound speed in the blood vessel wall was 1400 ± 10 m/s, and the density was 1020 kg/m^3. These acoustic properties approximate of a real blood vessel. A continuous flow was generated using a pump (BT100-2J). The flow could be controlled through the control panel. The maximum flow was limited by the pump capabilities. The flow in the experiments varied from 50 ml/min to 70 ml/min, corresponding to a blood FV of 26 cm/s to 37 cm/s respectively. These blood FV are in line with the normal blood FV extracted in the middle cerebral artery (Bishop, Powell, Rutt & Browse, 1986) of a normal patient. The inside structure of the vessel phantom was assumed to be perfectly circular. A compatible tube provided by the manufacturer was used with the pump (white color tube shown in the front view of Fig. 3.1) to carry the blood mimicking fluid (Shelley Medical Imaging Technologies, London, ON, Canada) to the vessel. The blood mimicking fluid contained particles of size 5μm which scattered ultrasonic waves. The blood mimicking fluid was circulating in a closed-loop circuit at room temperature and atmospheric pressure. In this manner, there was a continuous flow of fluid without disruptions. It should be noted that before passing the liquid inside the blood vessel phantom, the extremities of the tube were bonded together to avoid potential leakages. A bone phantom (the same as the one used in the previous chapter) was positioned above the blood vessel phantom as shown in the top view of Fig. 3.1 at an approximate distance of 50 mm. The bone phantom was held by a holder to keep the distance constant between the vessel and the bone phantom. The tank was filled with water to simulate the properties of soft tissue. The experiments were performed using a 1.5L64-0.3x15 probe manufactured by Guangzhou Doppler Electronic Technologies Inc. The ultrasonic probe was positioned above the bone phantom with a distance varying between 1 mm and 2 mm. This water layer was used to mimic the skin thickness. The probe was maintained with a holder to ensure a constant position and orientation, while the water layer thickness was varying, for all the experiments performed on the phantom. The probe was connected to a Verasonics Vantage 64 LE system. The imaging plane was an oblique longitudinal plane relative to the flow direction. An angle of approximately of 45^o was chosen. The choice of the angle was arbitrary and also limited by the structure used to hold the blood vessel. However, the results obtained in this chapter could easily be extended to other angles.

3.2.1 Methodology

3.2.1.1 Doppler processing

The whole Doppler processing pipeline is shown in Fig. 3.2. On the top, there is a probe shown which emit plane waves. The emission of a plane wave captures the movements of blood

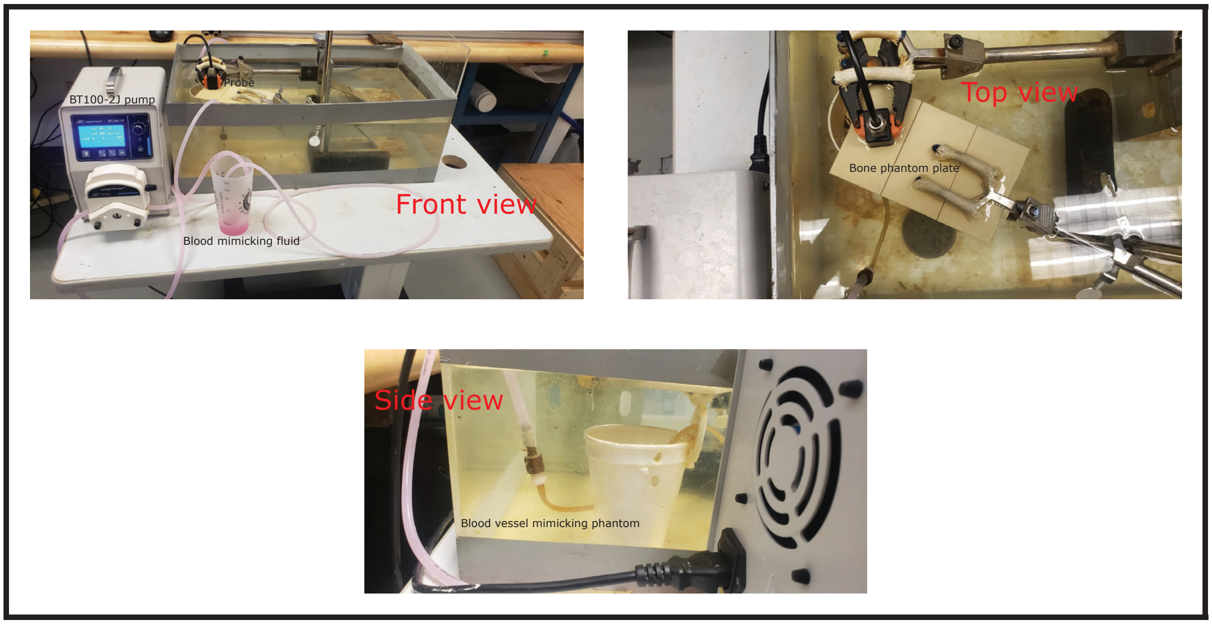

Figure 3.1 Front view: photo showing a BT100-2J pump which controlled the flow of blood mimicking fluid. The blood mimicking fluid was circulating in a closed loop. A ultrasonic probe connected to Verasonics Vantage 64 LE system. Top view: the bone phantom plate. Side view: photo showing the position of a blood vessel and a cup holding it.

scatterers inside the insonified area of the vessel. The algorithm parameters listed in Table 3.1 were chosen to obtain a Doppler sampling frequency for plane wave Doppler imaging.

Table 3.1 Doppler experiment settings used for plane wave Doppler algorithms

	Plane wave Doppler
Wave frequency	1 MHz to 2 MHz
Cycles used for the emitted signal	10 cycles
Aperture	64 elements
Steering	$\pm 5^o$
Imaging depth	100 mm
Number of waves	300
Acquisition time for one Doppler image	42 ms
Number of frames in a Doppler image	60

US wave frequencies used in the experiments varied between 1 MHz and 2 MHz. The input signal was a 10-cycle Tukey windowed burst, and the sampling frequency was 250 MHz. The probe consisted of 64 elements. Five angles were used for Doppler imaging which were evenly

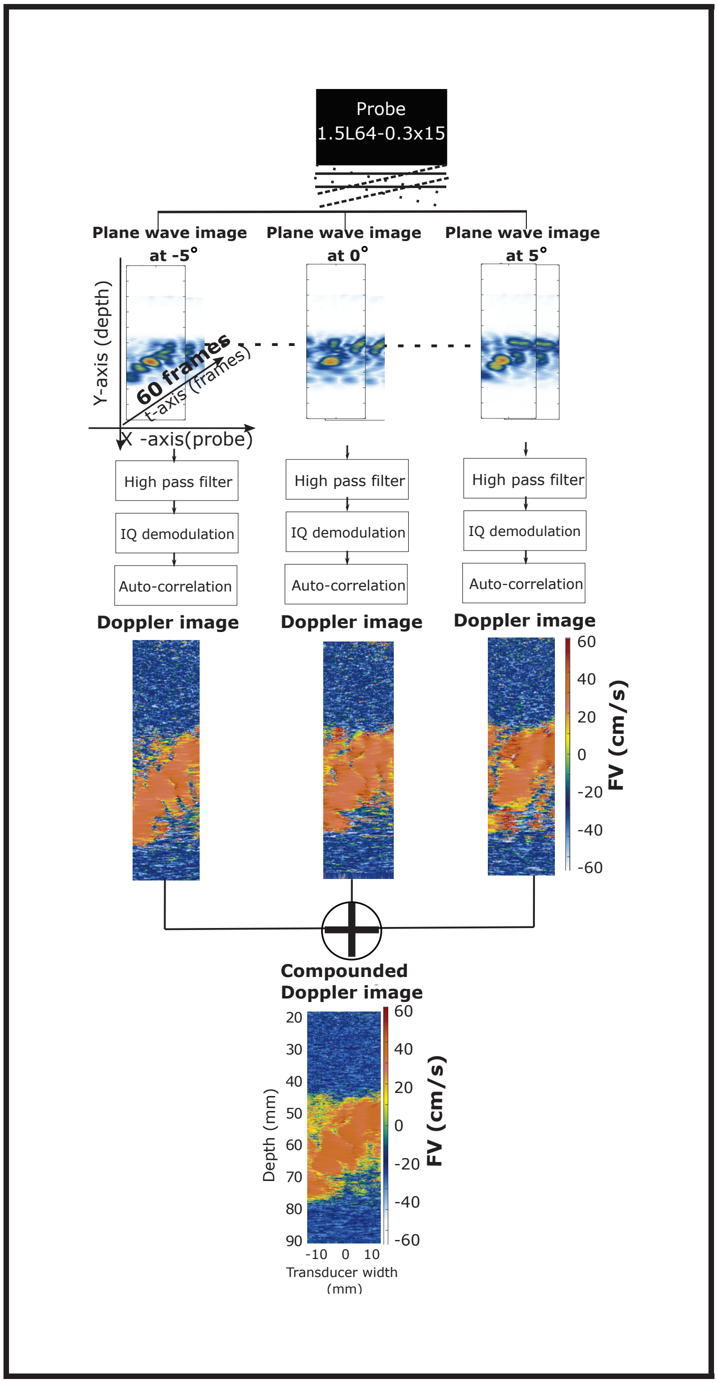

Figure 3.2 Probe 1.5L64-0.3x15 emitting plane waves at five different angles. Image reconstruction at different angles was performed and Doppler images were formed at each angle which were afterward combined to form a single compounded Doppler image.

spaced between $\pm 5^o$ with an angle step of 2.5^o. To capture the movements of blood scatterers inside the blood mimicking fluid, 60 plane waves were emitted for each angle. Those 60 plane waves were saved in a sequential manner in a frame. This made the frame length of 60 in a Doppler image. The same step was repeated for all the angles. Therefore, the number of emissions for all the angles was 300 waves. For the present application, a maximum depth of 100 mm was used. For the 100 mm depth, the time required for one plane wave to travel 100 mm in both directions was 0.134 ms according to the speed of sound in water. But, during the experiments it was set to 0.14 ms, so that there was no overlapping between received and emitted ultrasonic wave. Finally, to capture the complete Doppler data one angle required 8.4 ms, and the complete acquisition required 42 ms. Once the acquisition was completed, beamforming was performed using a DaS calculation of the captured data for each angle. A set of beamformed images for a single angle was taken, a clutter filter was applied to reject the low frequency components like the movement of vessels walls etc. The clutter filtering can be done in many ways for example by using the singular value decomposition (SVD) (U. Lok,P. Song & Chen, 2020) or by applying a simple high pass filter. In this study, a simple high pass 100 Hz 6th order Butterworth filter was applied to each pixel of the set of images. IQ demodulated images were then calculated. Each pixel of these IQ demodulated images is represented as $z_{(x,y,t_i)}$, where x is the probe axis, y is the depth, and t_i is the successive pulse emissions as shown in Fig. 3.2. The autocorrelation method was then applied to the filtered data (Kasai *et al.*, 1985) to determine the axial blood FV at each pixel. Once the blood FV map was obtained, the same steps were repeated for all the angles. After these steps were completed, there were 5 different Doppler images for 5 different angles. But the image quality using only a single plane wave was poor, so to improve the quality coherent compounding was applied as described in (Couture *et al.*, 2012). The coherent compounding principle combines all the backscattered echoes coming from a set of n angles plane waves titled with different angles to form a single Doppler image. Currently, velocity estimation errors occurring due to the angle of emission with respect to the bone was not considered. Due to this, blood FV values can still be underestimated or overestimated, affecting the overall blood mimicking fluid flow calculation. However, in this thesis, the insonification angles considered for plane waves were within $\pm 5^o$, so multiplying by the cosine of the insonification angle would have a small effect on the results.

3.2.1.2 Frequency optimized Doppler experiment

To validate the frequency optimized method developed in the previous chapter, the result presented in Fig. 2.6 was used. To confirm the effect of acoustic impedance mismatch on Doppler experiments, two types of experiments were performed: (1) constant water layer thickness and (2) constant input signal. The reason to do so was to show that both the water layer thickness and the frequency could have a significant impact on the blood mimicking fluid flow measurements. The two types of experiments are shown as blue and red dots respectively in Fig. 3.3. The red dots experiments were performed with a distance between the probe and the bone phantom of 1 mm and for a flow rate of 50 ml/min. The blue dots experiments were performed in which the flow rate was set to 65 ml/min keeping the transmitted frequency constant. Firstly, the initial position of the probe was marked at the top of the bone phantom plate and then it was moved up step by step, thus increasing the gap between the probe and bone phantom plate. This gap mimicked the skin thickness. In the blue dot experiments, the probe was moved to a distance of 0.2 mm, 0.4 mm, and 0.6 mm and Doppler experiments were performed by sending multiple tone burst signal at a constant centre frequency of 1.17 MHz. For the red dot experiment, the distance between the probe and the bone phantom plate was constant and close to 1 mm, but centre frequency of the tone bursts were 1.17 MHz, 1.45 MHz and 1.97 MHz.

3.2.1.3 Doppler experiment for the quantification of blood mimicking fluid flow

The blood mimicking fluid flow from the Doppler images was calculated according to the Eq. 3.1.

$$Q = \frac{v \cdot \pi \cdot (d)^2}{4}, \tag{3.1}$$

where Q represents the flow rate, v the velocity calculated from the Doppler images, and d is the diameter of the vessel. A ROI was defined for images that aimed at segmenting the vessel from

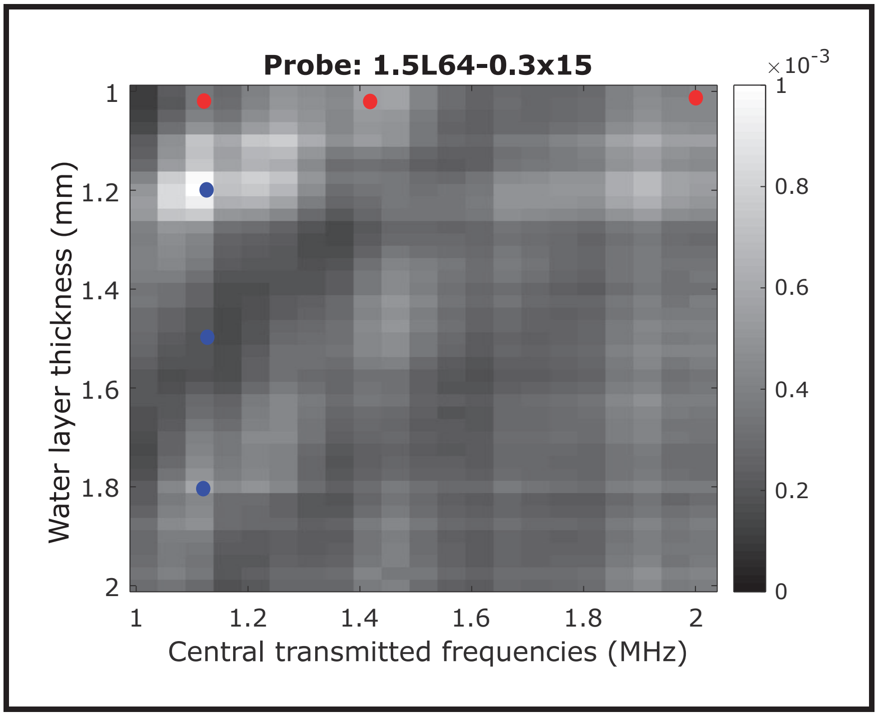

Figure 3.3 Figure showing transmitted amplitude as a function of frequency and water layer thickness obtained experimentally. Blue dots present the experiments performed at three different water layer thicknesses, keeping a 1.17 MHz center frequency. Red dots corresponds to the experiment performed with a constant distance between the probe and the bone phantom plate but varying centre frequency.

the Doppler image. A schematic diagram showing the process of defining the ROI is shown in Fig. 3.4. The ROI was defined by first selecting the maximum pixel value from the B-mode image and then pixels were selected whose values dropped to -3 dB.

This kind of thresholding is known as full-width half maximum and is generally accepted in signal processing (Webb, 1993). Thus, the ROI was defined as two oblique straight lines passing through -3 dB pixel points (equivalent to half of maximum pixel value) in the image, which covers most of the vessel and disregards the noisy part of the image. Diameter was defined as the width perpendicular to ROI. Fig. 3.5 (a) shows the result of this process on a real reconstructed B-mode image using minimum number of cycles that could be emitted from the probe at its center frequency. It should be noted that since the outer structure of the blood vessel phantom

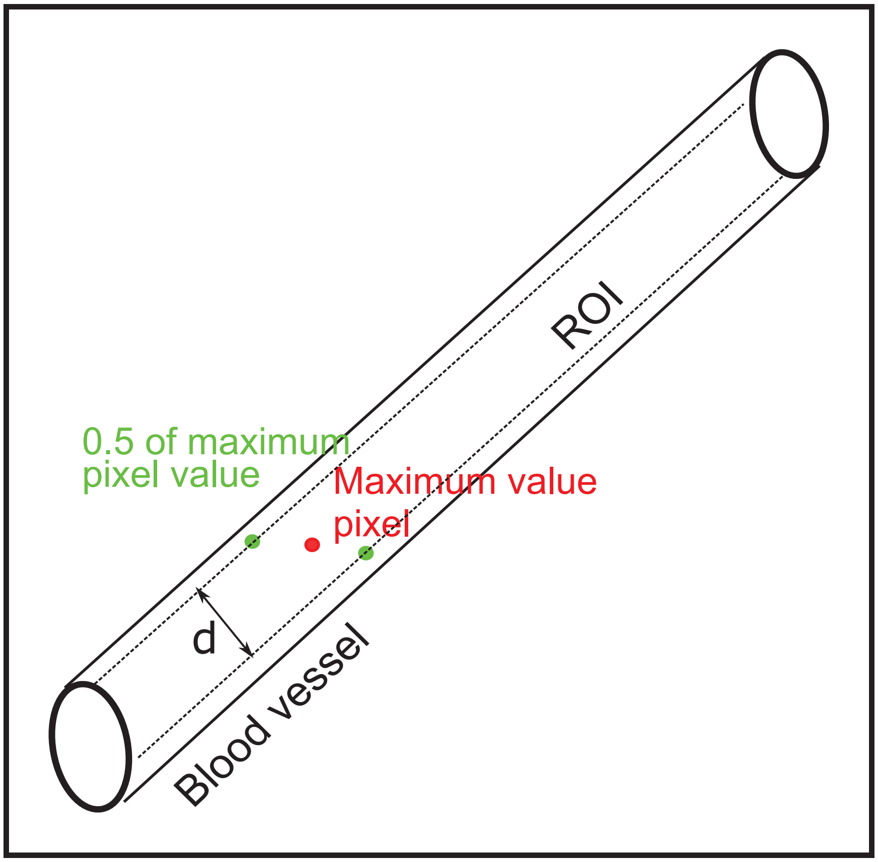

Figure 3.4 Schematic diagram showing the process to calculate the diameter of the vessel. Firstly, the maximum pixel value was selected (shown in red color) and then pixels whose values drop down to half (shown in green color) compared to the maximum pixel value were selected. ROI was then defined as two oblique lines passing through the points where the intensity of the pixel was dropped to half of the maximum. The diameter "d" is the width perpendicular to the selected ROI.

was irregular, some parts of the vessel were smaller than others in the reconstructed B-mode image. Based on the calculated ROI from a B-mode image, the diameter of the vessel was calculated perpendicularly to the flow direction. The calculated diameter from the B-mode image was 5.40 mm. The calculated ROI was then used and placed on the top of the Doppler image to segment it as shown in Fig. 3.5 (b) . Since Doppler imaging requires many cycles to be emitted, the spatial resolution was not optimal and as a result, the reflection obtained from the vessel was larger than the original size of the vessel. The velocity calculated from the

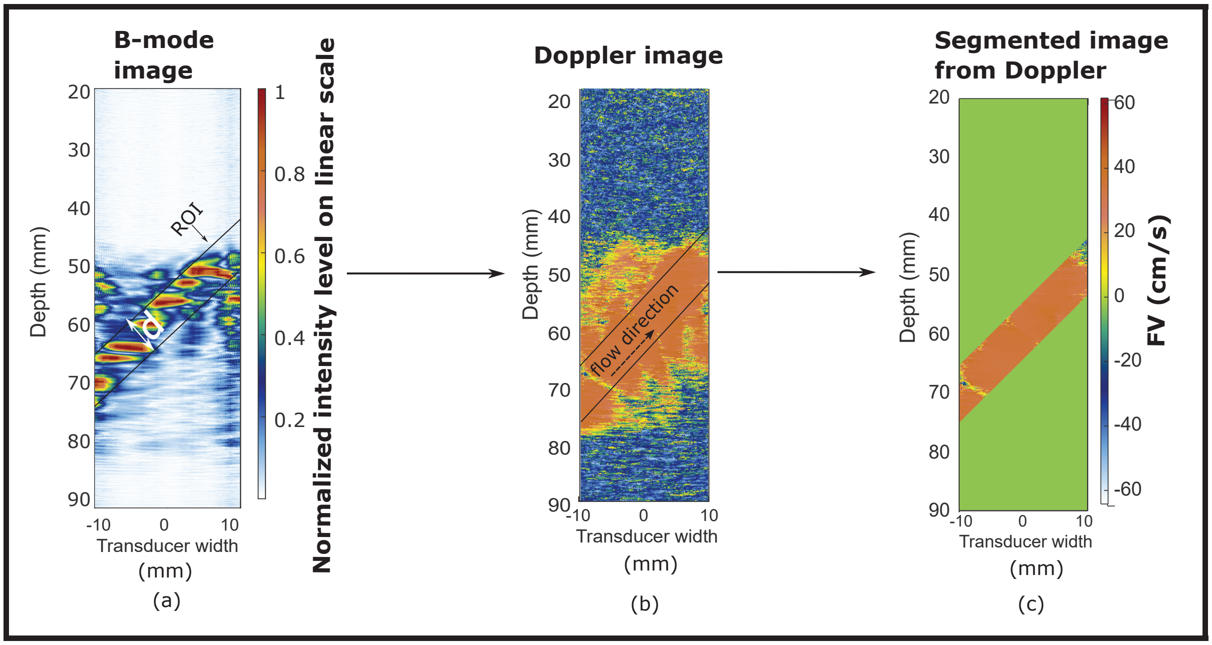

Figure 3.5 Figure showing (a) B-mode image of a blood vessel mimicking phantom showing the diameter "d" and the defined ROI (b) Doppler image constructed using a plane wave imaging algorithm showing velocity which was calculated using an autocorrelation method (c) A segmented Doppler image using the defined ROI. From (a) the first image, the diameter of the vessel was calculated using pixel values when it drops down to 0.5 and two oblique horizontal lines were drawn with the size of diameter, and the region between the lines is called ROI. (b) ROI was placed on top of the Doppler image to segment and an arrow inside the ROI shows the flow direction. (c) FV of the blood mimicking fluid flowing in the vessel is the mean value of the pixels inside ROI.

segmented image Fig. 3.5 (c) was the mean value of the pixels inside the corresponding ROI from an autocorrelation equation. For the current phantom configuration, five experiments were performed using the plane wave imaging algorithm. Control of the flow from the pump was kept constant at 65 ml/min, and the flow direction of the blood mimicking fluid was towards the probe.

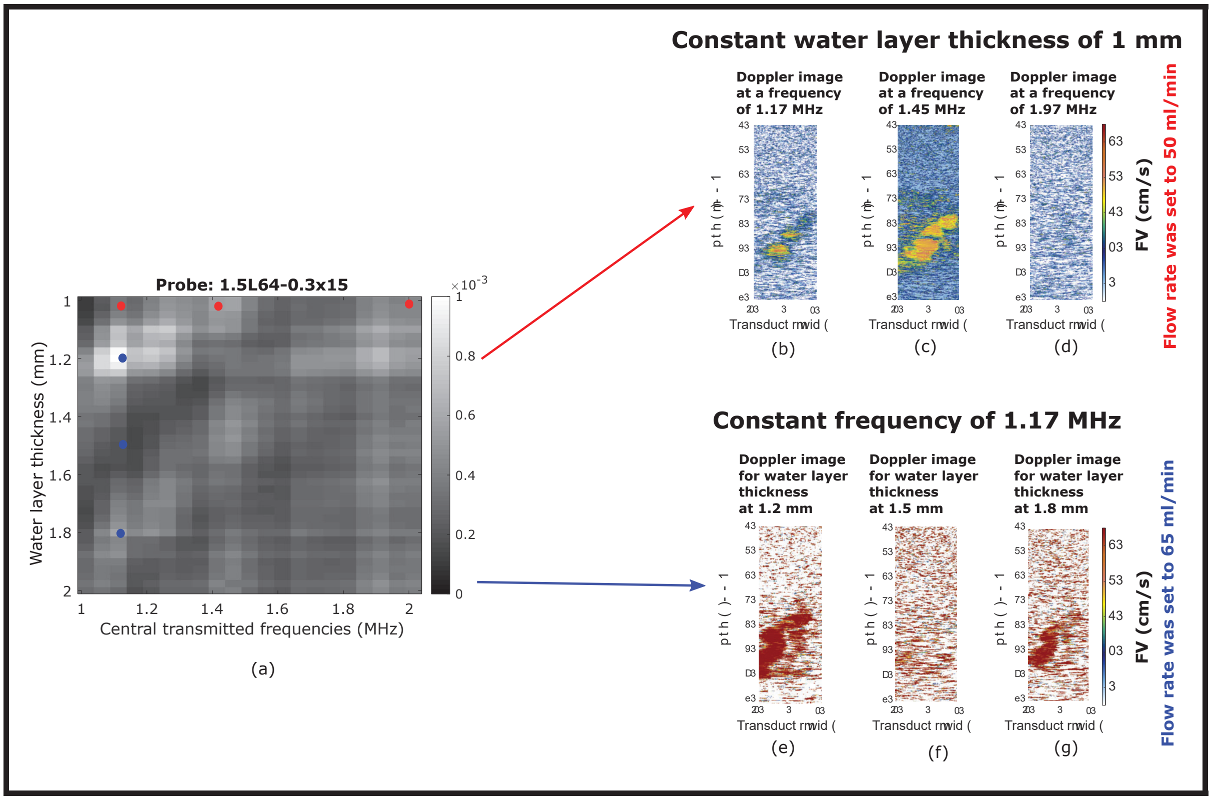

Figure 3.6 Figure showing the effect of acoustic impedance mismatch done on Doppler images. Figures b,c and d correspond to a distance between the probe and the bone phantom plate of 1 mm and 3 different centre frequencies and the flow rate for this experiment was set to 50 ml/min. Figures e,f and g correspond to a centre frequency of 1.17 MHz and a distance between the probe and a bone phantom plate of 1.20 mm,1.50 mm and 1.80 mm and the flow rate for this experiment was set to 65 ml/min.

3.3 Results

3.3.1 Impedance mismatch

Fig. 3.6 shows the effect of impedance mismatch considering Doppler effect. Fig. 3.6 (b), (c), (d) correlates to the red dots in the 2D map shown on the left. The corresponding FV was therefore 28 cm/s which can be estimated with a centre frequency of 1.45 MHz. However, when the centre frequency was set to either 1.17 and 1.97 MHz the FV could not be easily detected. This is in line with the transmission maps obtained in the previous chapter and shown in Fig. 3.6 (a). Fig. 3.6 (e), (f), (g) represents a second experiment. In these experiments, the centre frequency was kept constant at 1.17 MHz. The flow rate could not be detected with a distance of 1.5 mm between the probe and the bone phantom plate at 1.17 MHz as was suggested by the energy transmission map shown in Fig. 3.6 (a).

3.3.2 Quantitative flow

The quantitative flow results are provided in Table 3.2.

Table 3.2 Flows calculated from five reconstructed images. The values are in ml/min and the standard deviation and mean flow is calculated for the reference. The calculated values from the reconstructed images showed consistency over different experiments with overestimation of blood mimicking fluid flow rates.

	First Experiment	Second Experiment	Third Experiment	Fourth Experiment	Fifth Experiment
Theoretical flow rate	65 ml/min	65 ml/min	65 ml/min	65 ml/min	65 ml/min
Calculated flow rate	398.50 ml/min	451.40 ml/min	462.53 ml/min	431.75 ml/min	486.72 ml/min
FV	29.10 cm/s	32.85 cm/s	33.66 cm/s	31.42 cm/s	35.42 cm/s
True FV	34.48 cm/s				
Calculated diameter	5.40 mm				
True diameter	2 mm				
Measured quantities for all the five experiments	**Standard deviation of all the five experiments**			**Mean of all the five experiments**	
FV	2.38 cm/s			32.48 cm/s	
Flow rate	33.24 ml/min			446.18 ml/min	

The measured flow rate was approximately seven times higher than the true flow rate. Consistency of the flow rate results was proven by showing a standard deviation of 33.28 ml/min for a mean flow rate of 446.18 ml/min, which accounted for only a 7.3% of deviation around mean. Similarly, for the FV the results obtained showed a standard deviation of only 2.28 cm/s with a mean of 32.48 cm/s. The diameter of the vessel was overestimated by approximately 2.7 times the real diameter. These results showed that it was possible to calculate the flow rate inside the vessel in the presence of bone with great consistency. The overestimation of the diameter calculated from B-mode image was, however, a strong limitation.

3.4 Discussion

In this chapter Doppler images were obtained to show the effect of the acoustic impedance mismatch, this laid a background for a proof of concept that using a fixed frequency may lead to unsuccessful Doppler measurements. This chapter also measures the quantitative flow rate in the blood vessel phantom from outside the bone phantom via the plane-wave Doppler. It was shown in this chapter that adapting the frequency to the distance between the probe and the bone phantom plate had a significant influence on the success of a measurement.

The results showed that for a given water layer thickness, there could be multiple frequencies for which Doppler measurements were successful. But there were some other frequencies in which Doppler measurements were unsuccessful, because there was insufficient energy transmitted for that combination of water layer thickness and frequency. Therefore, it is very important to first measure the skin and bone thickness of the patient, and then based on the 2D map select the right frequency for which there is high transmission of ultrasound.

Under normal circumstances, the flow rate in TCD varies between 50 ml/min to 70 ml/min. However, with vasospasm, the blood FV can reach up to 180 cm/s that corresponds to a flow rate of 340 ml/min (Kohama, Sugiyama, Sato, Endo, Niizuma, Endo, Ohta, Matsumoto, Fujimura & Tominaga, 2016) which implies a very high flow rate. Such high flow rates were not achievable in the current experimental setup. The elasticity of the blood vessel phantom used in the experiments was not high enough to support this. Flow rates higher than 100 ml/min were tried and the phantom ruptured because of the high flow. Therefore, a flow rate between 50 ml/min to 70 ml/min was used to keep the vessel intact. However, the proposed method for optimizing frequency with respect to the acoustic impedance mismatch effect will still remain valid and Doppler measurements can be extended to the higher FV also.

The results from Table 3.2 showed the consistency of the Doppler measurements done on the phantoms. However, the flow rates were overestimated by by a factor of about seven. The reason behind this was the diameter which was overestimated by approximately 2.7 times. Since the flow rate is directly proportional to the square of the diameter as shown in Eq. 3.1, the flow rate was overestimated by a factor of approximately 7. The overestimation of the diameter was caused by the pulse length used in the experiments. The smallest pulse length which could be sent from the probe was approximately double the diameter at the center frequency of the probe. Therefore, in the B-mode image of a blood vessel phantom, the diameter appears much larger than it is in reality. For Doppler imaging a longer pulse length was used to have a narrow frequency band such that there was a minimum error in determining the Doppler shift. To rectify the problem of determining the diameter in the B-mode image correctly, one solution is to use a probe that can send a shorter pulse to accurately capture the diameter of the vessel.

Apart from the overestimation caused by the diameter, the measured FV from the Doppler image was consistent and close to the theoretical FV. The mean FV obtained from the experiments was 32.48 cm/s with a standard deviation of 2.28 cm/s which is very close to the theoretical FV of 34.48 cm/s. This showed that the major cause of the overestimation of the flow was from the diameter and not from FV.

3.5 Conclusion

The study in this chapter was performed to show the effect of acoustic impedance mismatch on Doppler data. Due to the acoustic impedance mismatch effect, Doppler measurements were successful at 1.45 MHz for a given 1 mm water layer thickness, and for other frequencies where the SNR was low, Doppler measurements were unsuccessful. The same phenomenon was observed when water layer thicknesses were varied keeping the frequency constant at 1.17 MHz, in this case at a water layer thickness of 1.5 mm. The method was not able to record the FV due to low SNR. This effect adds to the effect of attenuation already present in the bone phantom. Based on these results, it would be advisable for clinicians to change the emitted frequency of the probe depending on the skin and bone thickness of the patient. Doing so will make it possible to measure the localized blood flow from cerebral arteries. After proving the concept of acoustic impedance mismatch on Doppler images, quantification of flow rates were performed using five experiments in which flow rates were kept constant at 65 ml/min. The results obtained showed an overestimation of flow rates by a factor of seven , due to an overestimation of the diameter. Overestimation of the diameter occurred due to the usage of pulse lengths which could not be shortened due to the limitations of the probe used. Though flow rates were overestimated, they were consistent between the five experiments, with a standard deviation of 33.24 ml/min and a mean of 446.48 ml/min, which represents only a 7.44% deviation around the mean value. Additionally, the mean FV calculated from all the five experiments was very close to the theoretical FV with an absolute difference of 2 cm/s. A method for estimating the vessel diameter is therefore essential to successful flow rate measurements.

CHAPTER 4

IMPROVING ULTRASONIC IMAGING THROUGH IRREGULAR SURFACES

4.1 Introduction

Imaging of the blood vessels present inside the brain via TCD is difficult because it suffers from the poor ultrasonic transmission. This poor transmission is due to the presence of the skull in the wave propagation path. As suggested in the previous chapters, the skull introduces many effects that decrease the transmitted energy of the ultrasound for example phase aberration, variations in the speed of sound in the skull, scattering, acoustic impedance mismatch, and absorption. However, all the aforementioned effects did not consider the reduction of ultrasonic transmission due to the outer part of the skull. The skull is a three-layer structure in which the diploe is sandwiched between outer and inner tables as shown in Fig 4.1 (a). As shown in Fig. 4.1 (b), the layers of the skull have a curvature and are not flat as shown in Fig. 4.1 (b). However, in this chapter the effects due to outer surface of the skull will be investigated. Due to irregular shape, the US plane wave gets distorted and scattered in different directions and transmission loss happens. The work presented in this chapter studies the loss of transmission due to the external surface of the skull and introduces a process to improve the transmission.

4.2 Simulation of the effect of irregularity of the skull surface shape on the transmission of ultrasound

4.2.1 Finite element simulation

A FEM model for which a schematic is presented in Fig. 4.3 was used to simulate the transmission of longitudinal US through the temporal window of the skull. It was built upon a skull CAD whose geometry was provided by True Phantom Solutions inc. The mesh used in the simulation consists of triangular elements and was optimized to provide a convergent solution to the wave equation. Twenty-five finite elements per wavelength were used in the water layer (Mickael Brice, 2008). The first layer of the model was a piezoelectric layer which consisted of 64 finite elements

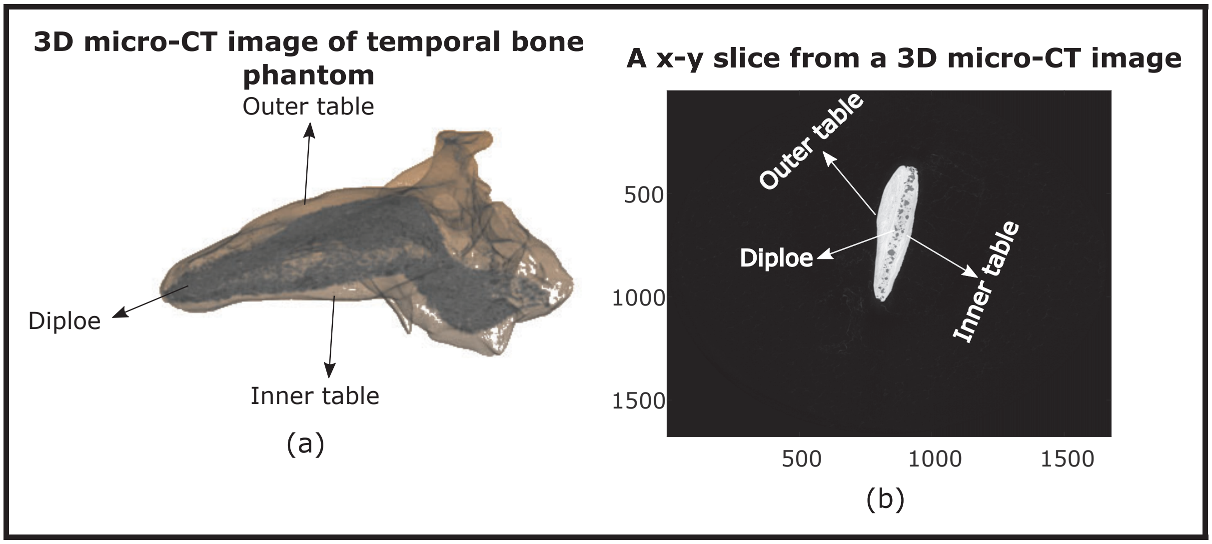

Figure 4.1 A 3D micro-CT scan of the phantom (Wydra & Maev, 2013) of the temporal part of the human skull. This phantom is 7 mm thick and consists of three-layer structure of bone. Outer table being the outermost part of the skull, diploe having the most porosity, and the last is the inner table. (b) A slice through the thickness of the bone. The outer table has a slight curvature due to which there is an ultrasonic transmission loss as shown in Fig. 4.2

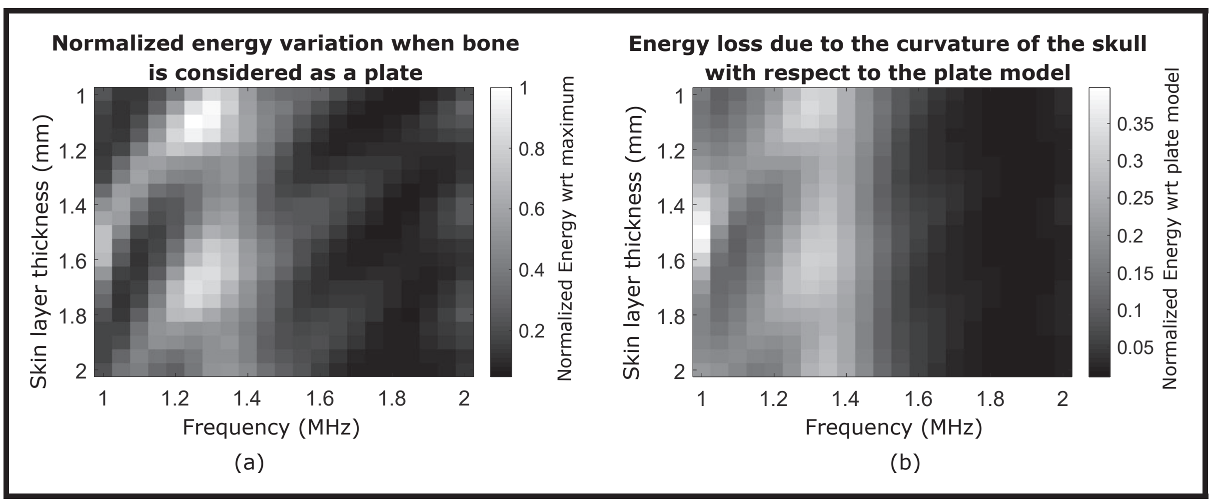

Figure 4.2 Transmitted energy as a function of skin and bone thickness. These are the results of a FEM simulation performed in section 5.2.1. Figure (a) shows a simulated map of the ultrasonic energy transmitted to the brain when considering bone as a plate. Figure (b) represents energy transmitted to the brain with respect to the plate model when the bone is considered to have curvature. The variation of energy along the water layer thickness axis is due to acoustic impedance mismatch effect.

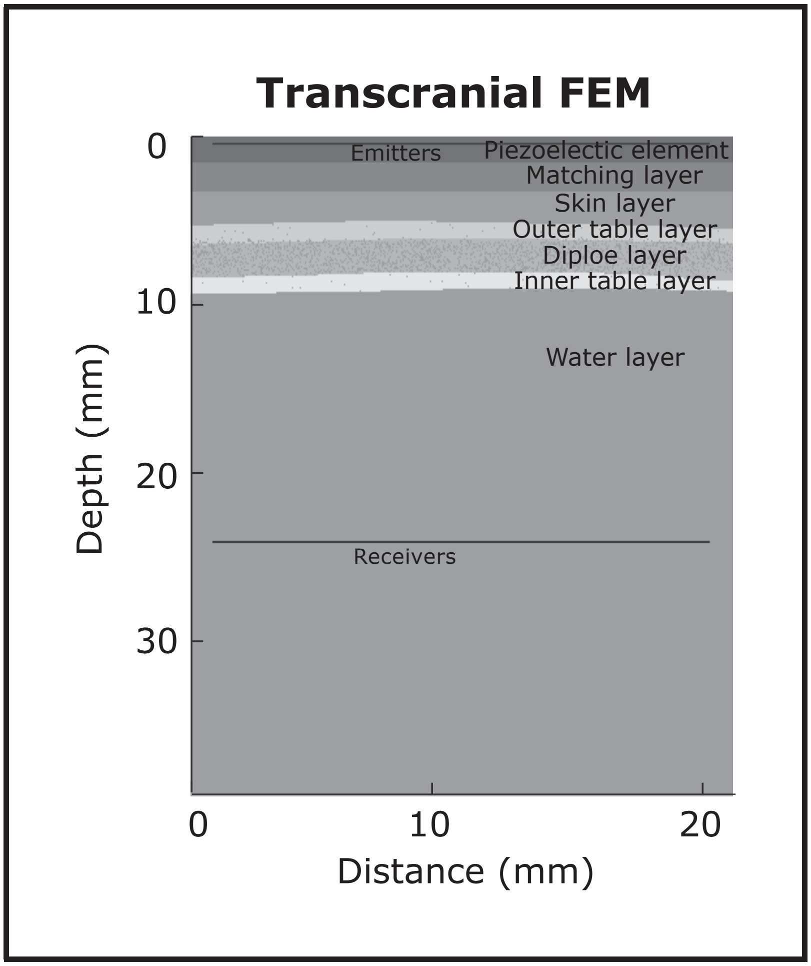

Figure 4.3 A two-dimensional FEM acoustic wave propagation model for transcranial US. Each section presents a material whose property is given in the Table 4.1

and with the properties shown in below Table 4.1. All finite elements from the piezoelectric layer transmitted ultrasonic waves simultaneously to generate a plane US wave. A 10-cycle Tukey windowed tone burst was used as an excitation. A time step increment of $1ns$ was used based on the stability criteria defined by $\delta t = 0.8 * \delta x / v_{max}$ (Rajagopal & Lowe, 2007), where v_{max} is the fastest velocity among the given materials. The POGO finite element solver was used to run the simulation (Huthwaite, 2014). The material properties were taken from (Fry & Barger, 1978) and are in the below Table 4.1 where E is the modulus of elasticity. It should be noted that water was modelled as an isotropic elastic solid layer. The reason was POGO cannot model fluids with acoustic elements (Huthwaite, 2014). The porosity in the bone region varies from 30 to 60% in the diploe region and 5 to 10% in the outer and inner table region (Fry & Barger, 1978). For the simulation purposes, the porosities were introduced artificially. Here porosity means the introduction of elements in the model which were filled with water properties. For example, 35% porosity in the diploe layer meant that 35% of the elements present in the diploe layer were given the properties of water. The same was done by introducing a porosity of 5% each for the outer and inner table.

Table 4.1 Material properties used in the FEM.

Material	E (GPa)	Poisson's ratio	Density (Kg/m3)
Piezoelectric layer	157	0.39	7500
Skin layer	.04	0.49	1000
Matching layer	14	0.34	2195
Diploe layer	13.40	0.25	1740
Outer and Inner table layer	20	0.3	1890
Water layer	.04	0.49	1000

As shown in Fig. 4.2 the FEM predicted a loss of energy whenever a curved surface is encountered by a plane wave due to the distortion of the wavefront. The solution to this problem is to stimulate the transducer elements in such a way as to compensate for the irregular shape of the skull and create a plane wave after ultrasonic transmission through surface of the outer table so that US thereafter continues to propagate as a planar wavefront. To do that, firstly it is important to know the shape of the surface (in this case outer table). This information can be derived by calculating the time taken by each element of the probe to receive the reflected waveform from the outer table, hereafter called a delay. If the delays are the same for each element, the surface is flat and there is no surface shape compensation required. If the delays are not the same then there is a need for surface shape compensation. Once delays are calculated for each element, then the ultrasonic wave can be transmitted with the calculated delays in such a manner that a planar wavefront is formed after propagation through the outer table. To accomplish this the SAUL (Hopkins *et al.*, 2013) technique from the non-destructive testing literature was used. This technique uses 4 to 5 plane wave transmissions depending on the geometry of an inspected surface. Multiple transmissions are needed to calculate the delay for individual transducer elements. Since, a single plane wave transmission do not capture the true delay information of the skull shape, and has information mixed up from the neighbouring elements as shown in Fig. 4.4 (a), and called incoherent delays. Increasing transmissions decreases the incoherency of delays for each element for surface adaptation. After a few transmissions, the delays for each element becomes coherent (each element's delay does not have an effect from the neighbourhood element) and becomes adaptive to the surface in the received waveform as shown in Fig. 4.4 (b). Thereafter, a plane wave is transmitted compensating the reception delays.

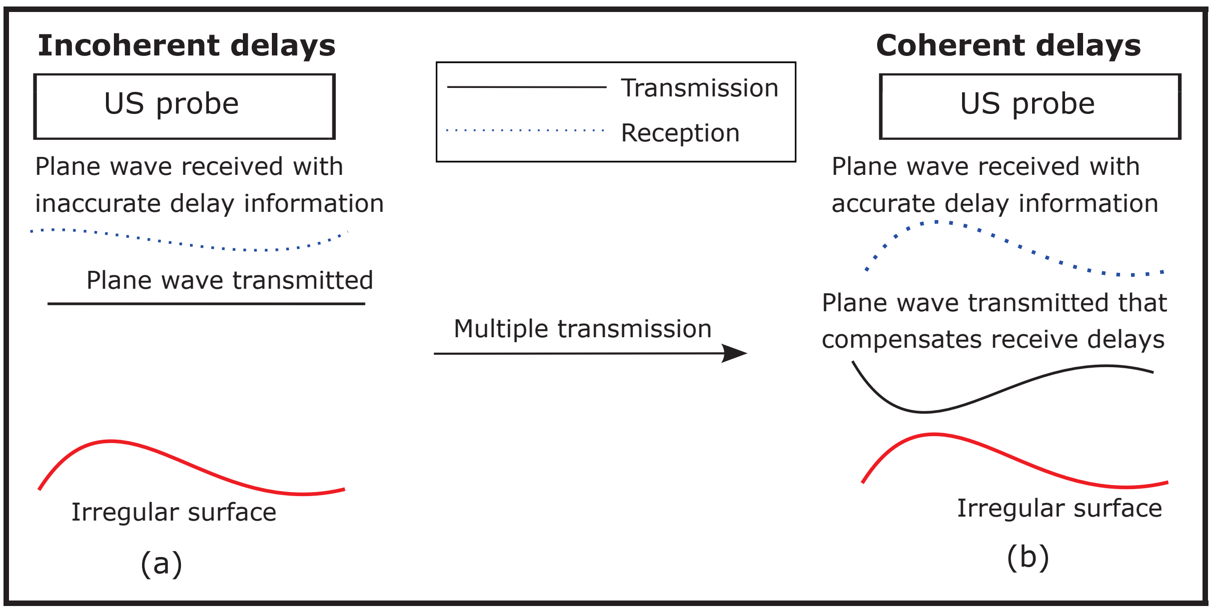

Figure 4.4 Schematic diagram showing incoherent vs coherent delays. Figure (a) shows when a plane wave is transmitted, delays due to irregularity of the skull shape becomes incoherent and transducer elements do not catch the true delays due to the surface shape. These kind of delays are called incoherent delays. Figure (b) shows that when multiple US plane waves are transmitted with adapted delays, transducer elements capture the true information of delays in the plane wave reception. These kind of delays are called coherent delays. Thereafter, a plane wave is transmitted that compensates the reception delays.

Firstly, to calculate the delays a plane wave was generated from the emitters shown in Fig. 4.3 from the top to the bottom. Since there is a significant acoustic impedance mismatch between the skin and the outer table layer, a reflection will occur from the surface. To identify the reflection, a waveform with a very small wavelength is required, ideally, a probe with a centre frequency varying from 5 to 10 MHz will suffice since the thickness of the skin is very small and usually varies from 1 mm to 2 mm (Seidenari & Giovanni, 1999). But transcranial Doppler measurements are done with a lower frequency, varying between 1 MHz and 2 MHz with a correspondingly larger wavelength. If a probe with a higher center frequency is used for surface compensation, then it has to be replaced with a lower frequency probe for Doppler measurements. The problem is that replacement of the probe will not guarantee the same position from where the surface profile is calculated. The solution to this problem is to make use of a delay line and keep using a low-frequency probe (Chang, Cho, Wang & Zou, 2013). A delay line is medium placed between the active elements of a probe and the skin layer. The delay line has acoustic properties similar to skin (Chang *et al.*, 2013) and can therefore be used without affecting energy losses due to acoustic impedance mismatch. A delay line varying from 7 mm to 10 mm is sufficient to calculate the surface profile using a low-frequency probe. The cross-correlation technique was used to compute the delay for each element.

Figure 4.5 shows the surface profile calculated by sending the plane wave multiple times and adapting it each time to the surface of the outer table. It also shows the comparison with the theoretical surface taken from the CAD model for comparison. The estimated and theoretical surfaces are in very close agreement.

A plane wave was transmitted with the calculated delays that compensated the irregularity of the skull shape, and created a planar wavefront after the outer table surface.

Figure 4.6 below shows a simulation of a compensated plane wave and a plane wave which was sent without the delays. This simulation was carried out for a 2 MHz centre frequency with a skin and average bone thicknesses of 2 and 4 mm, respectively. The attenuation for the bone region was set to 45 dB/cm @ 2.25 MHz. The dashed oval in the figures shows the arrival of the waves after the outer table surface. It can be clearly seen in the zoomed region of the two figures that the plane wave has lower energy because of uneven spread and has some lighter shaded areas over the oval-shaped region due to the curvature of the surface. Quantitatively, the surface compensated plane wave had 8.12 dB higher energy as compared to the non-compensated plane

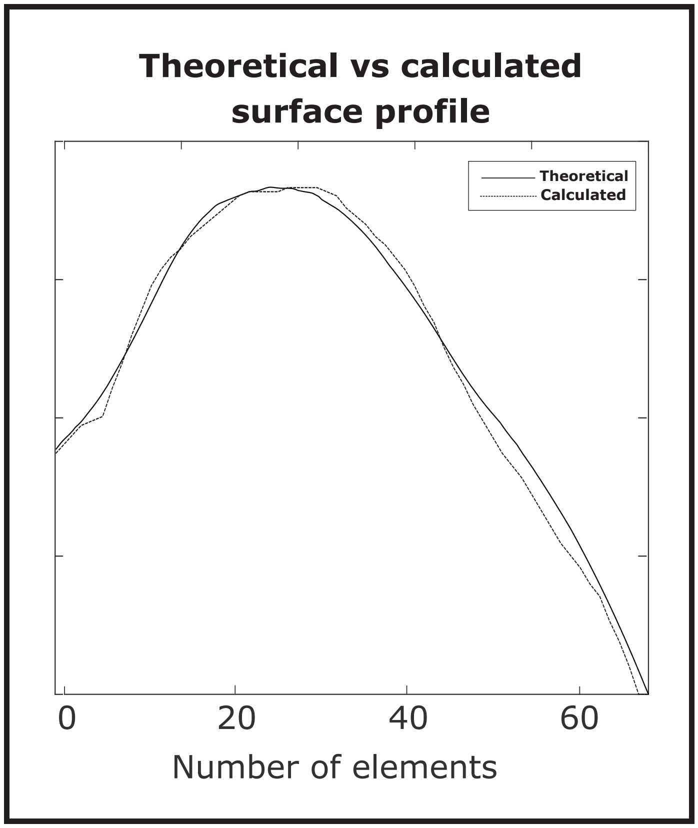

Figure 4.5 Comparison between the theoretical and calculated surface profiles. The theoretical surface was taken from a CAD model, and the SAUL method was used for calculating the surface profile.

wave for this simulation. This was assessed by dividing the normalized energy of the surface compensated plane wave with that of the plane wave from the 2D map shown in Fig. 4.7 for a skin layer thickness of 2 mm at 2 MHz. This simulation was done only for one combination of skin and bone thicknesses, but from the results described in Chapter 3, it was clear that due to acoustic impedance mismatch, some combinations of skin layer thickness and frequency might lead to poor transmission. To evaluate this effect, a 2D simulation was run for different skin layer thicknesses and frequencies keeping the bone thickness constant. The 2D map of Fig. 4.7 (a) shows that the transmitted energy is increased in the case of surface compensated plane wave transmission as compared to plane wave transmission. Fig. 4.7 (b) shows that for any

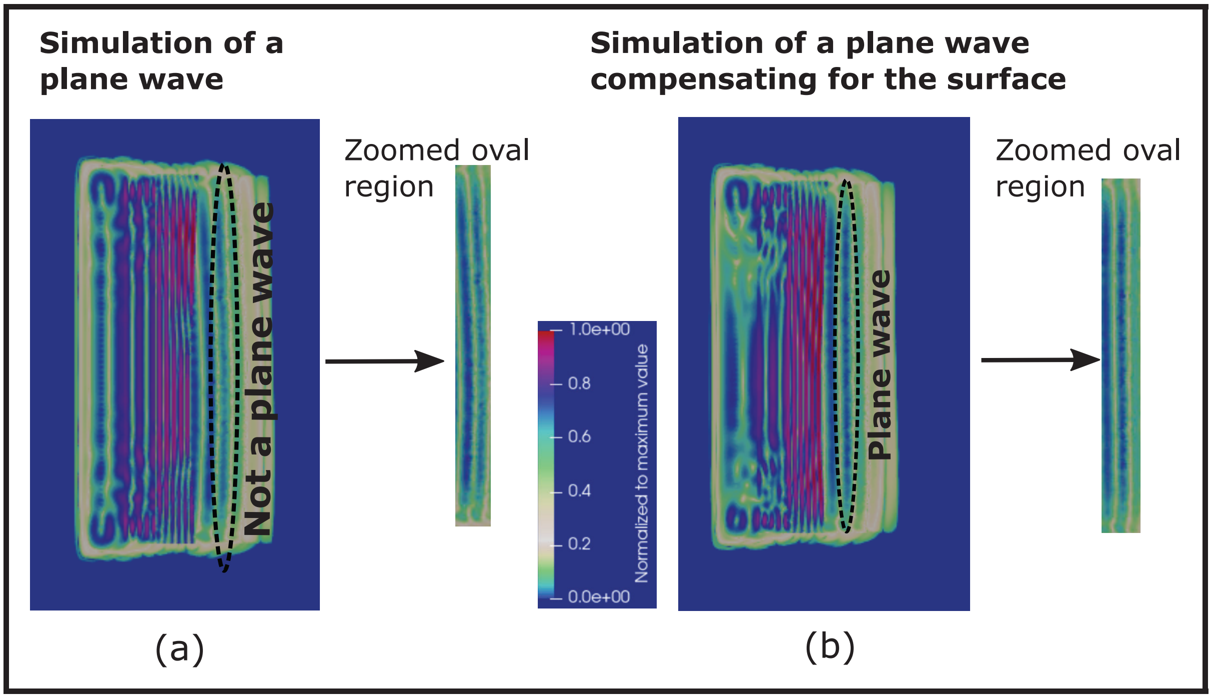

Figure 4.6 Figure showing simulation comparison for compensated and without compensated plane wave. The figure (a) shows an uncompensated plane wave after the outer table. The oval region marked presents wavefront after passing through the outer table. The figure (b) shows a surface compensated plane wave after the outer table. The one with surface compensated plane wave has overall 8.12 dB greater energy as compared to normal plane wave transmission.

given combination of skin layer thickness and frequency, the overall transmission of energy via compensated plane wave imaging is greater uncompensated plane wave transmission.

Plane waves should be transmitted at multiple angles to enhance the SNR (Le Jeune *et al.*, 2016), and thereby improving plane wave Doppler imaging. Given the success of the proposed surface shape compensation method for the transmission of 0^o angle plane waves, the same method for the angle transmission as well was applied. Fig. 4.8 shows the transmission of a compensated plane wave and an uncompensated plane wave at 10^o angle to the surface as a proof of concept. Again, the transmitted energy after the outer surface was greater in the compensated plane wave simulation. Fig. 4.9 shows a 2D map for different skin layer thicknesses and centre frequencies when a plane wave is transmitted at a 10^o angle to the surface. The figure again showed that the

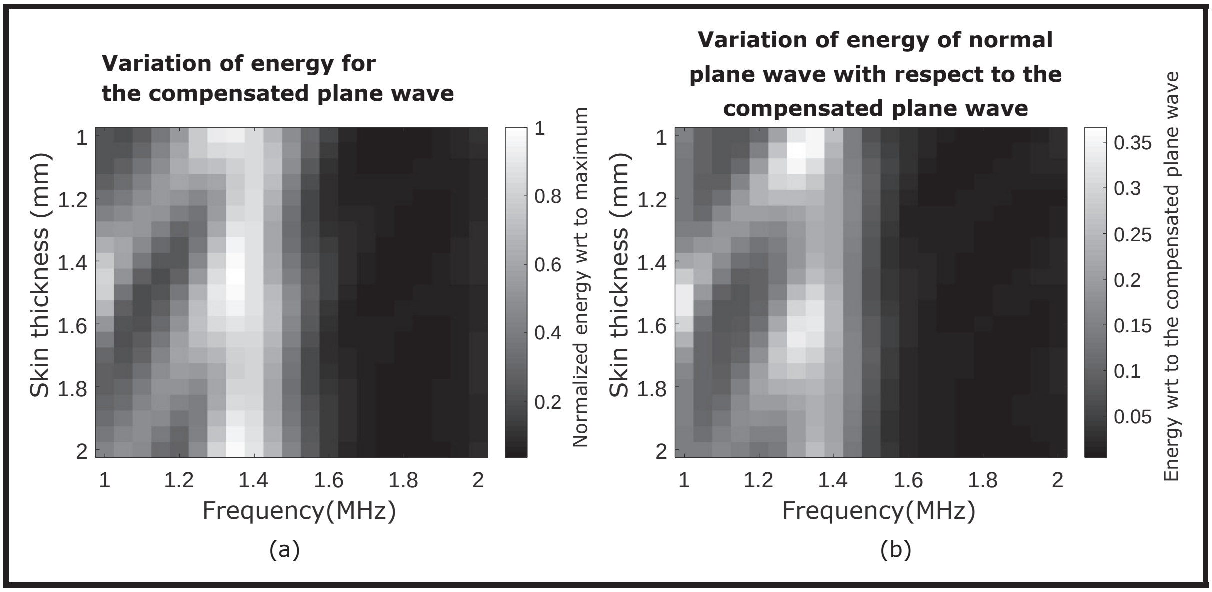

Figure 4.7 Figure (a) and (b) shows the transmitted energy variation for different skin layer thickness and frequencies for the surface compensated and plane wave. The compensated plane wave for each frequency had overall higher energy.

overall transmission of energy with the compensated plane wave was higher than normal plane wave transmission.

4.2.2 Experiment: A-scan comparisons between multi angle compensated and uncompensated plane waves for different skin thicknesses

To validate proof of concept developed in previous section, an experimental setup was devised. Fig. 4.10 shows the different components which were used to make the setup. A corner bracket was used to hold a linear positioning stage (Velmex A1503P20-S1.5, 0.025 mm resolution) vertically. The probe holder was fixed to the adapter using set screws. An ultrasonic probe developed by Guangzhou Doppler Electronic Technologies Inc. whose bandwidth is 1-2 MHz was attached and could be moved vertically using the linear stage. The whole assembly was immersed in a water tank, which also contained a temporal bone mimicking phantom (Wydra & Maev, 2013) made of a ceramic material mimicking the acoustic properties of the skull. Five kinds of different phantoms were used in this study with varied thicknesses, attenuation and geometrical shapes. All five phantoms are shown in Fig. 4.11.

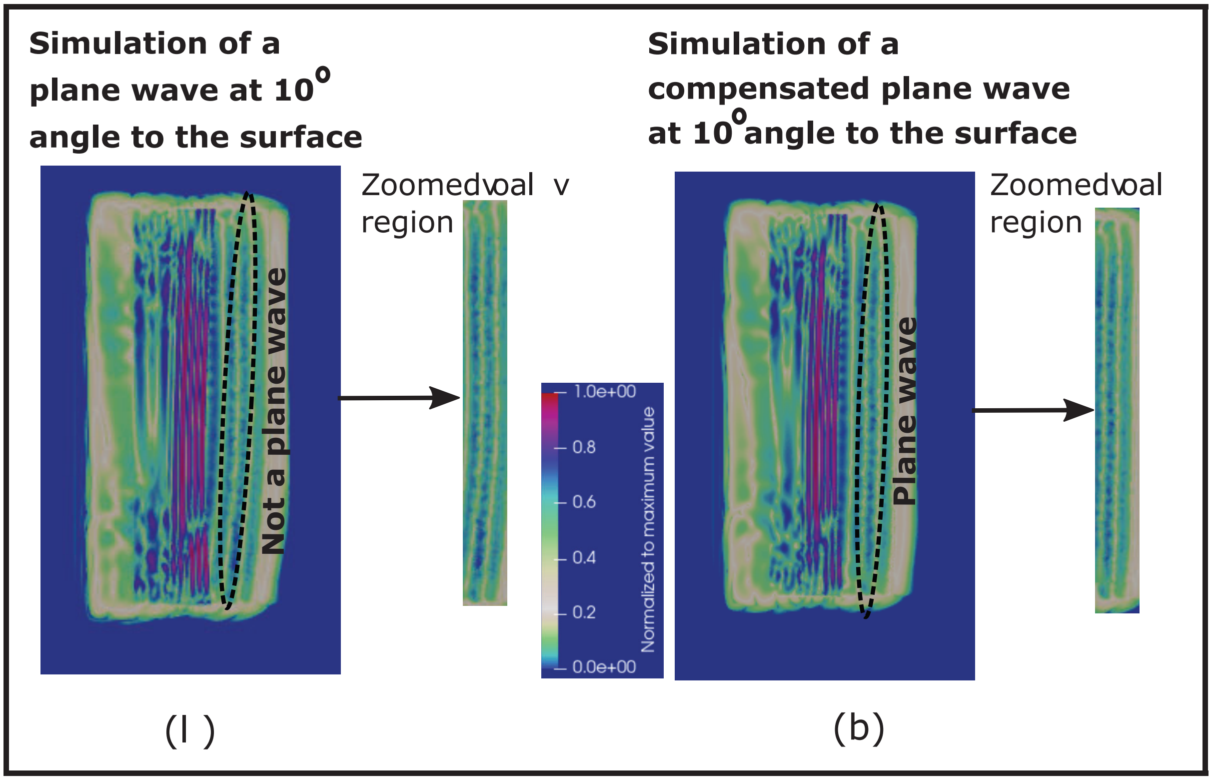

Figure 4.8 Simulation of compensated and a normal plane wave which was transmitted at 10^o angle. The wave inside the oval region has 2.40 dB higher integrated energy compared to normal plane wave transmission.

The acoustic properties of all the phantoms and their thicknesses are shown in Table 4.2. The following experiment was conducted for all the phantoms. An aluminum block was kept at a distance of 12 cm from the bone phantom and acted as a reflector. The water between the phantom and the probe mimicked the skin's acoustic properties.

Table 4.2 Acoustical properties of the phantoms.

Samples	Averaged thickness (mm)	Average speed of sound (m/sec)	Averaged attenuation at 2.25 MHz (dB/cm)
A	2.2	2820	45
B	4	2820	45
C	7	2820	45
D	4	2820	30
E	4	2820	60

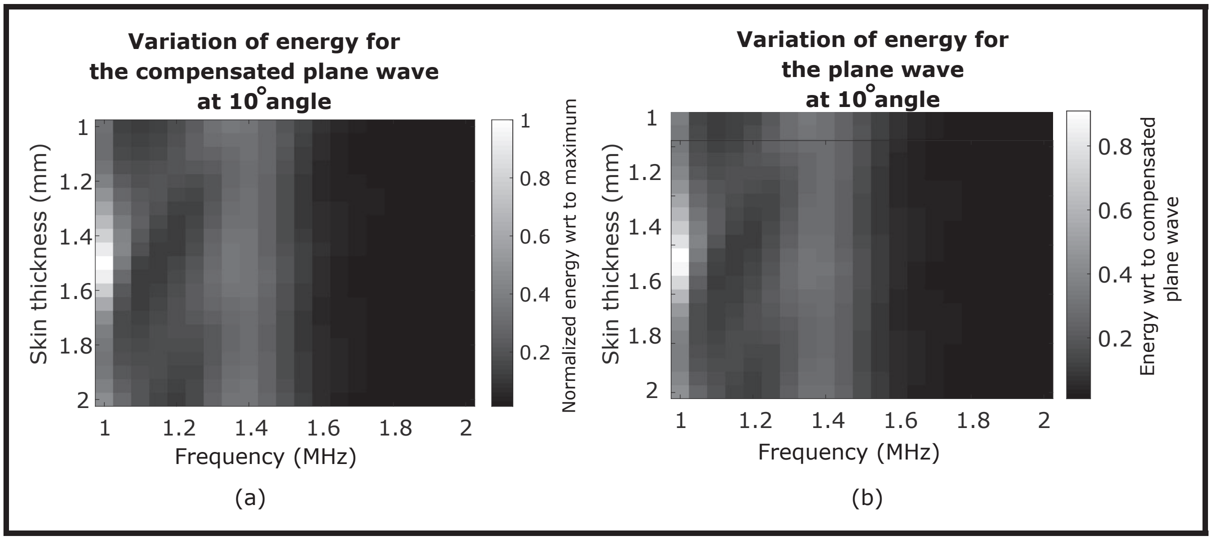

Figure 4.9 Figure (a) and (b) shows the transmitted energy variation for different skin layer thickness and frequencies for the surface compensated and plane wave at 10^o inclination. The surface compensated plane wave for each frequency has overall higher energy but does not have a huge improvement over the plane wave.

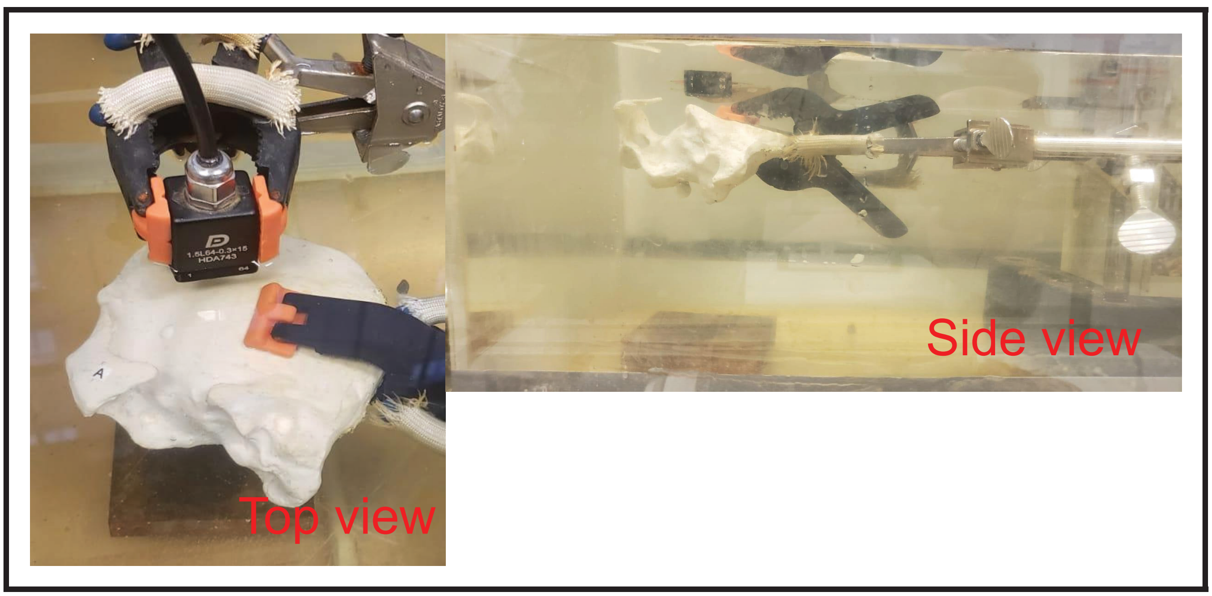

Figure 4.10 A digital photo of an experimental setup consisting of a probe, bone phantom, and an aluminum block which is used as a perfect reflector.

An ultrasonic probe was connected to a Verasonics vantage 64 LE system. The transmitted waveform was a 10-cycle Tukey windowed tone burst as shown in Fig. 4.12 (a). To first measure

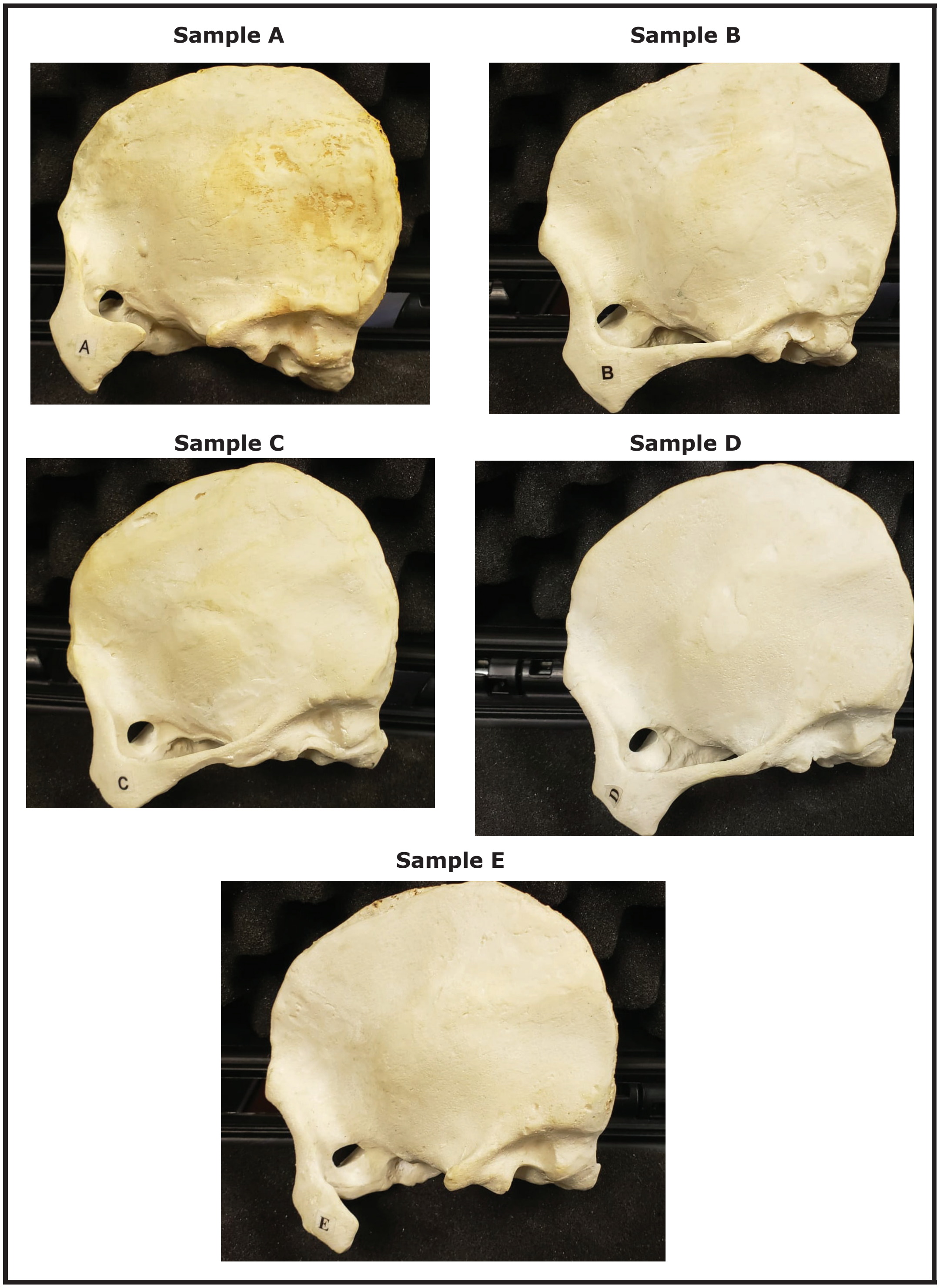

Figure 4.11 Five different temporal bone phantoms with different thicknesses and attenuation mimicking the acoustical properties of the skull.

the delay profile, the probe was moved up by 10 mm from the outer surface of the phantom. This gap mimics the delay line. A plane wave was emitted iteratively to fit the outer surface of the phantom. A typical delay profile is shown in Fig. 4.13. Once the delay profile was calculated, the gap between the probe and the outer surface of the phantom was adjusted to keep the water layer thickness between 1 mm and 2 mm. To make a measurement, surface compensated US is transmitted for a typical water layer thickness and the received waveform resulting from reflection off from the top part of the bone phantom and the surface of the aluminum block is captured. The captured waveform is shown in Fig. 4.12.

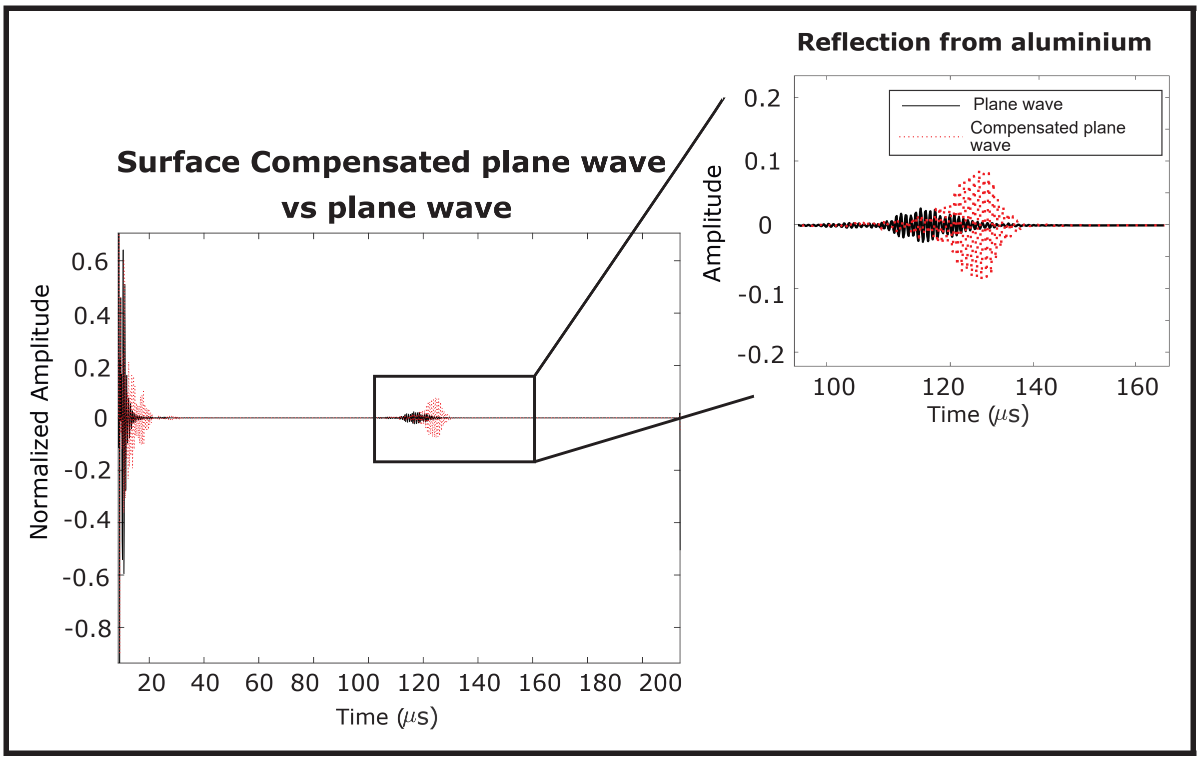

Figure 4.12 A typical time trace of a received waveform for sample B, comparing surface compensated and a normal plane wave for a frequency of 1.41 MHz and a gap between the probe and the bone phantom of 1.5 mm. The figure also shows a reflection from the aluminium block. The figure clearly shows an increase in the amplitude as well as the energy for a compensated plane wave.

The ratio of the extracted reflected waveform energy to the input signal energy was calculated according to Eq. 4.1

$$E_{brain} = \left| \frac{|\mathsf{FFT}(signal_{extracted})|}{|\mathsf{FFT}(input)|} \right|^2. \tag{4.1}$$

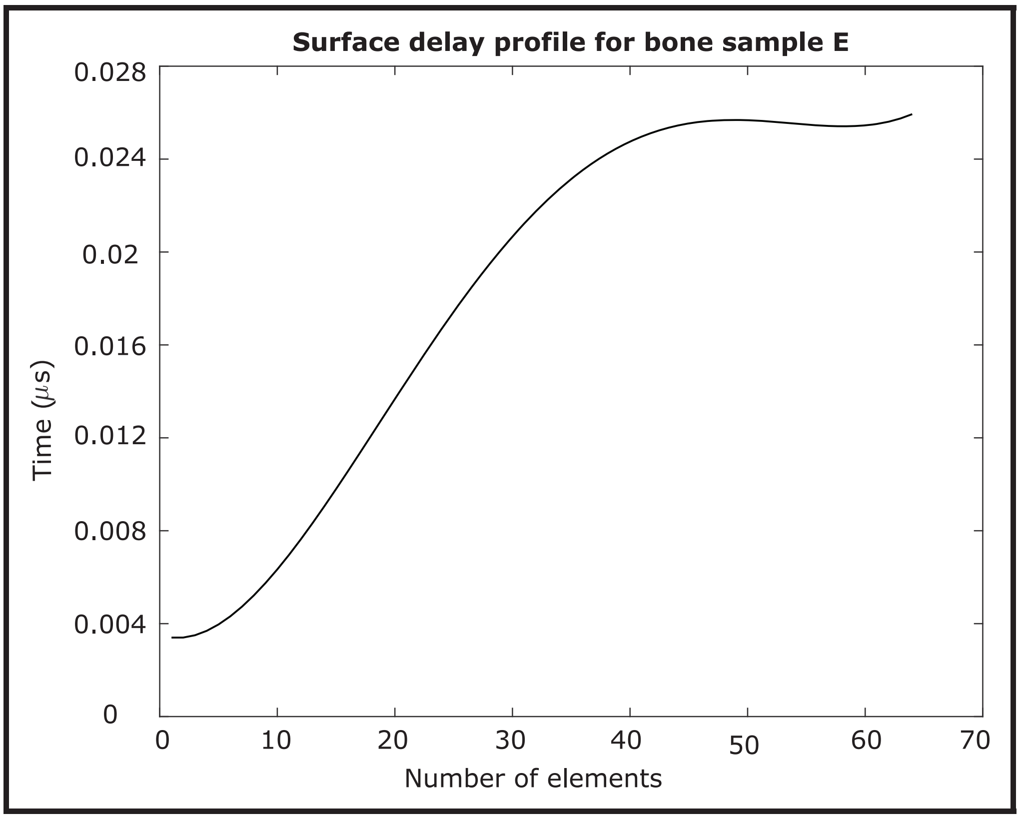

Figure 4.13 A typical delay profile calculated for sample E which was smoothed out for better representation.

Comparison of the received energy from surface compensated US and plane wave US experimentally was done. For example, as shown in Fig. 4.12, an experiment was done for a water layer thickness of 1.5 mm comparing the received energy waveforms of the two methods.

To measure and compare the received energy of the surface compensated US and plane wave US for all the samples shown in Fig. 4.11 steps mentioned below were performed for each sample:

1. The time delay profile was calculated by sending plane waves iteratively to fit the outer surface of the skull for each sample and one of the example for sample E is shown in Fig. 4.13. This curve was smoothed out for better presentation.

2. The gap between the probe and the bone sample surface was adjusted to mimic real skin thickness i.e. between 1 mm and 2 mm.

3. Multiple frequencies ranging from 1 MHz to 2 MHz were sent from the probe for a typical water layer thickness with angles ranging from -10^o to $+10^o$ at an interval of 5^o degree.

4. The received energy ratio was calculated for each frequency and angle using Eq. 4.1. Once it is done the ratio of maximum energy between surface compensated US and plane wave US was selected for the given water layer thickness.

5. Lastly, the probe was moved by a step of 0.2 mm to do the process in steps 3 and 4 until water layer thickness reaches 2 mm.

After completing this process, the results are shown in Fig. 4.14. This figure shows the comparison of the ratio of received energies between compensated and uncompensated plane waves in dB. The result shown were normalized to maximum of 30 dB for each sample. The gain in transmitted energy ratio between compensated and uncompensated plane waves was highest when 0^o angle was used irrespective of any sample and skin thickness. However, this gain in the energy ratio started to get diminished when ultrasonic waves were transmitted with a tilt for all the investigated temporal bone phantoms.

4.2.3 Experiment: B-scans comparison between multi angle compensated and uncompensated plane waves for all the five samples

A second experiment focused on the evaluation of image quality of surface compensated US and plane wave US. The setup was the same as in part A. To evaluate the SNR performance of the two methods on the image, both type of waves were sent with the probe one after another with a bone sample beneath the probe. The image area was 180 mm by 20 mm and covered the

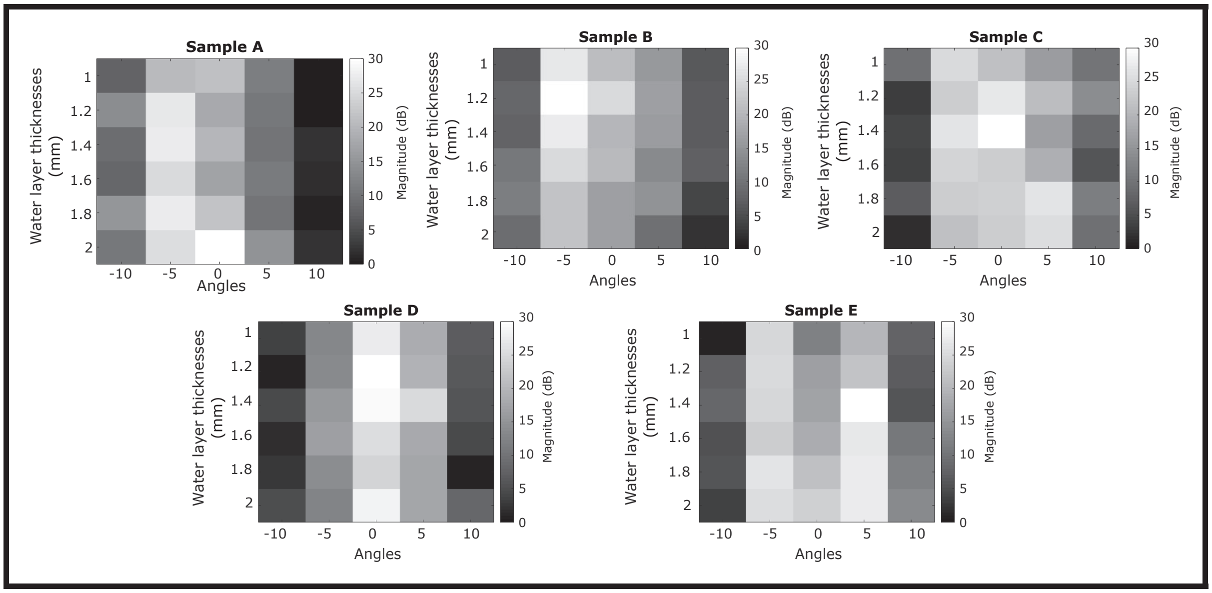

Figure 4.14 Experimental 2D maps of A-scan comparison for compensated and uncompensated plane wave. The x-axis of the figures represents angles varying from -10^o to $+10^o$, whereas the y-axis represents water layer thickness varying from 1 to 2 mm. The color scale represents the energy ratio between compensated and uncompensated plane waves in dB.

complete probe aperture. Experiments for the evaluation of B-scan images were done for the angles ranging from -10^o to $+10^o$ at intervals of 1^o. Once all the images from different angles were available, they were added up coherently to form one compound image. The SNR of each image was calculated via following process: sum of the energy was taken from the reflected region of aluminium block seen in the image and dividing it by the sum of the energy above and below the reflection region. This SNR calculation is shown in Eq. 4.2 which is coupled with Fig. 4.15. The water layer thickness was kept constant at 1.5 mm for every phantom. The way SNR was calculated is shown in Fig. 4.15 and its equation in Eq. 4.2. The results obtained from the experiments are shown in Fig. 4.16 and in Fig. 4.17. The results shown contain the SNR for each sample, for both the surface compensated plane wave US image and uncompensated plane wave US.

$$SNR = \frac{\sum\sum I^2_{x,y(reflectedregion)}}{\sum\sum I^2_{x,y(noisyregion_{upper})} + \sum\sum I^2_{x,y(noisyregion_{lower})}} \tag{4.2}$$

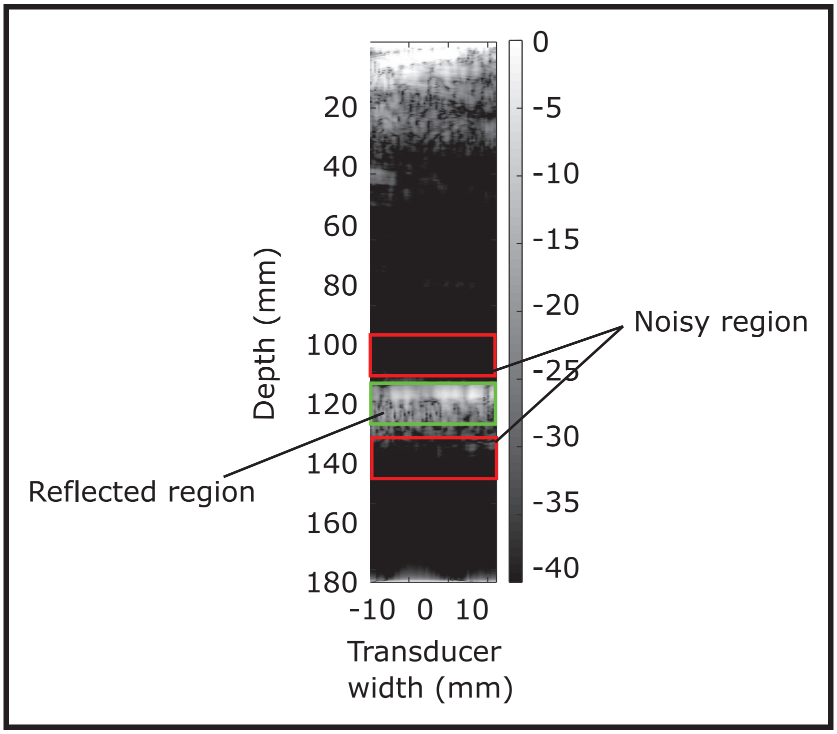

Figure 4.15 Figure showing an example of a B-scan image for the calculation of SNR. The x-axis of figure represents the transducer width in mm and y-axis represents imaging depth in mm. The red part in the image show noisy region and green part show the reflected region. SNR is calculated by dividing the sum of the energy of the reflected region by the sum of the energy of the noisy region also shown in Eq. 4.2

The results showed a reflection from an aluminium block at a depth of 120 mm from the probe for every sample. However, in every figure, reflection from the aluminium block was of different shape which was because of the different outer and inner shapes of temporal bone phantoms. There was an overall gain in SNR varying between 10-15 dB depending on the samples except sample E which showed only a gain close to 5 dB.

4.3 Discussion

In this chapter, the SAUL (Hopkins *et al.*, 2013) technique was used to improve the image quality of TCD systems using surface compensated plane waves. This technique was developed in

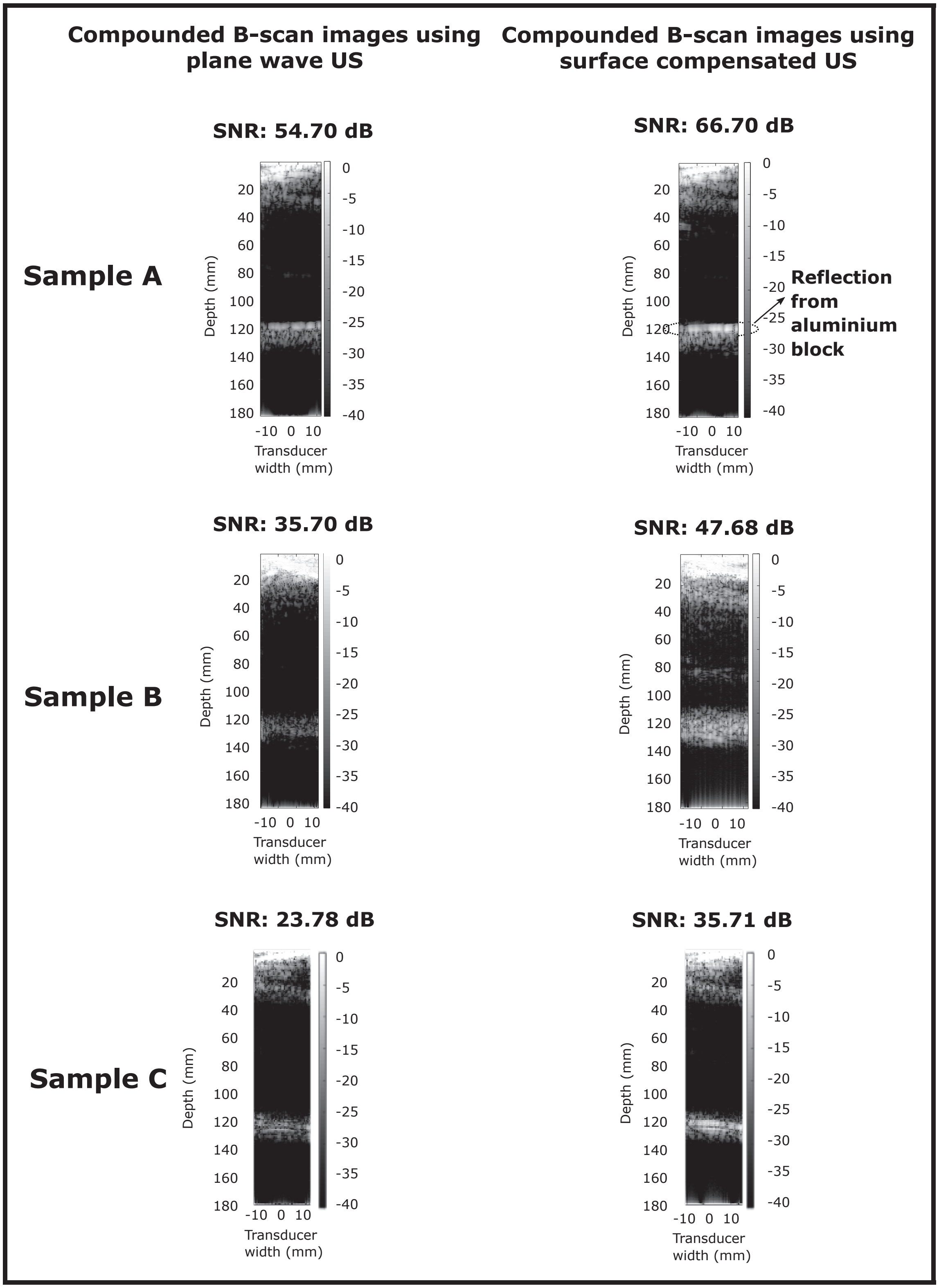

Figure 4.16 Experimental B-scan comparison for uncompensated plane wave and surface compensated wave for samples A,B and C. The x-axis represents the transducer width, whereas the y-axis represents the depth. All figures showing improvement in the transmitted energy in the case of surface compensated ultrasonic waves.

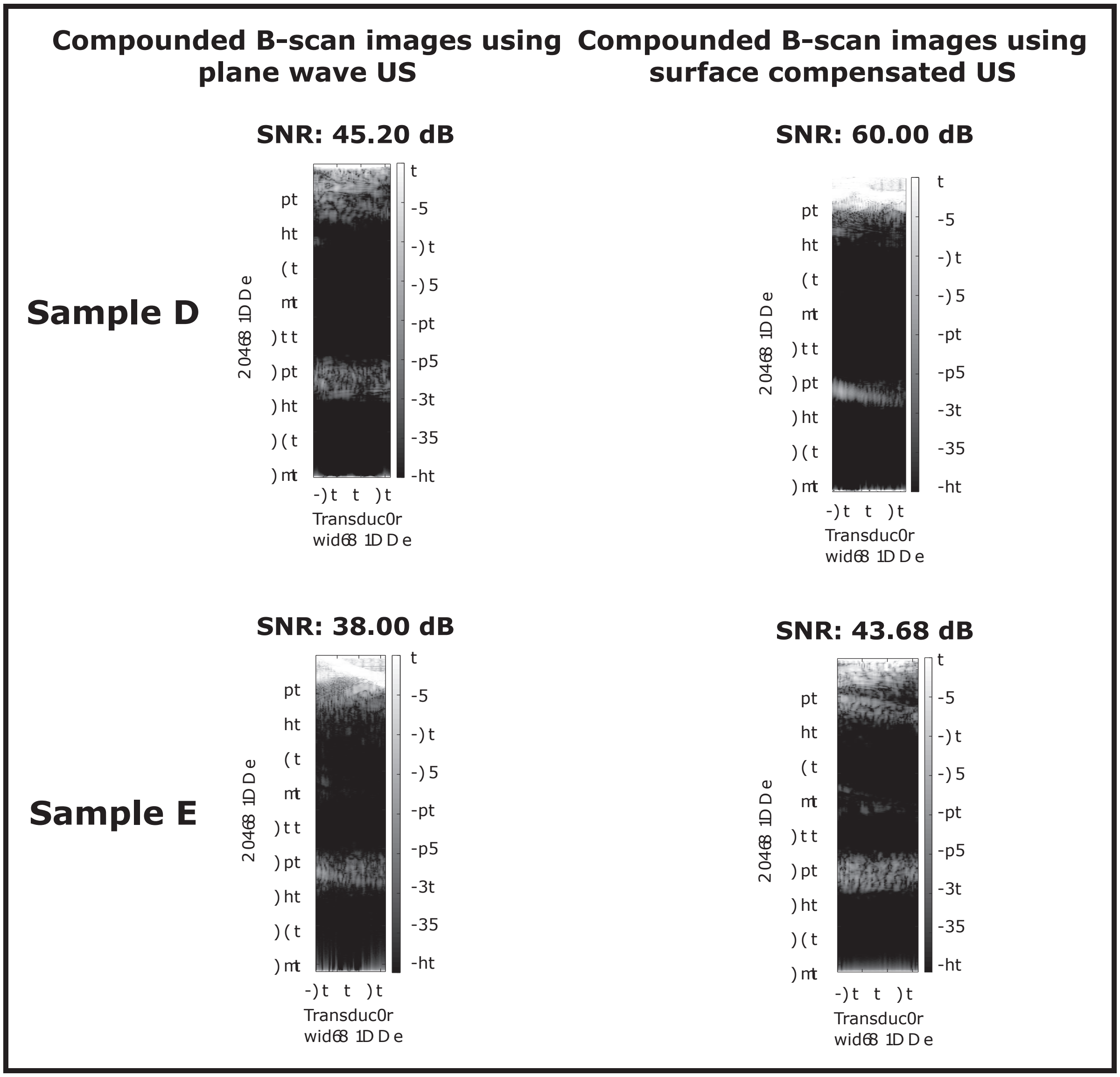

Figure 4.17 Experimental B-scan comparison for plane wave and surface compensated wave for samples D and E. The x-axis represents the transducer width, whereas the y-axis represents the depth. Both pair of figures showing improvement in the transmitted energy in the case of surface compensated ultrasonic waves.

NDT. By optimizing the imaging frequency based on the expected effect of acoustic impedance mismatch and timing the emissions from individual transducer elements to achieve the surface shape compensation, the transmission of US through the bone phantom increases. This increase in transmission leads to better image quality and higher chances of a successful Doppler measurement. The bone phantoms that were used lack heterogeneities and could cause more losses in the overall transmission. However, once the wave with a higher energy is penetrated after the outer boundary of the skull, these effects will be the same for both plane wave and surface compensated plane wave. The results obtained show that irrespective of the bone phantom properties like thickness and attenuation, surface compensated plane wave always have higher energy transmission and SNR as compared to an uncompensated plane wave. The reason is that the plane wave is distorted after propagation through the first layer of the skull.

The results in the FEM shown in Fig. 4.6 predicted that this improvement translates to a 65% increase in the maximum energy for a 0^o incidence angle and the specific phantom geometry involved in the simulation experiment. This percentage gain depends on the outer structure of the skull. The more distorted a plane wave gets due to the surface irregularity, more improvement compensation can bring. However, the gain in the transmitted energy was only 15% when a 10^o angle was used. One of the reasons is that when a longitudinal ultrasonic wave enters the skull with an angle, it can be refracted into shear waves according to Snell's law. Energy loss due to shear mode conversion can be considered as attenuation. It can also be seen that when the emitted wave is angled (Fig. 4.9) the amplitude of the plane wave emerging from outer surface of the skull is less as compared to the amplitude in Fig. 4.7 of FEM which proves the concept that energy is lost in shear waves when angled ultrasonic waves are emitted. However, it is important from the imaging point of view to consider multiple incidence angles, because images acquired from different angles are typically compounded to improve the overall SNR of images produced by plane wave TCD imaging. However, overall there is a limitation in this method if the surface shape is highly curved relative to the wavelength used then it might be possible there is no improvement at all (Hopkins *et al.*, 2013). The results in section 5.2.2 follow the same trend as predicted by the FEM where the ratio of received energy between plane and surface compensated plane wave is highest for a 0^o angle and degrades as the tilt of ultrasonic waves increases because of the introduction of shear waves (is considered as a part of attenuation) due to tilt of ultrasonic waves. So, it may happen that for larger angles there is no significant gain for the imaging purpose. Though, in most of the samples, maximum energy was seen at 0^o angle, in some of the samples like B and E maximum energy was seen at -5^o and $+5^o$ respectively. This might happen due to the misalignment of the probe relative to the bone sample. There was another limitation in the study, which involved considering reflection from an aluminium block. In reality, there would likely be scattering from various types of blood particles. This scattering might have a different effect on the overall SNR gain from surface compensated plane wave. A better solution might involve the use of a hydrophone rather than an aluminum block to see what impact surface compensated plane waves have on the overall transmission energy.

The results in section 5.2.3 demonstrate the performance of the method for transcranial imaging. The method was able to mitigate the challenge of energy losses caused by the complex geometry of the skull. Generally, TCD requires the probe to be placed at a 0^o incidence angle relative to the bone (Bathala, Mehndiratta & Sharma, 2013), but if it is not then there is an energy loss due to the tilt of ultrasonic waves. The method, as shown in section 5.2.3, alleviates this limitation by increasing the energy transmission for the angles that were tested. In all the samples, there is a gain in SNR varying from 10 dB to 15 dB, apart from sample E which showed a gain of only 5 dB. This exception might be due to the higher attenuation in sample E, which was 1.3 times the attenuation in sample (A, B, C) and 2 times the attenuation in sample D.

4.4 Conclusion

In TCD, energy losses caused by the irregularity of the skull has not been investigated in depth. The energy losses happen because the US plane wave gets distorted after encountering an irregular surface and loses its planar wavefront which causes a loss in the transmitted energy. This chapter focused on improving the distorted wave after propagation through an irregular surface. The improvement means converting a distorted wave into a planar wavefront. To do so, the SAUL technique was used to iteratively adapt each transducer element's emission delay to the geometry of the surface. Delays calculated from the SAUL method were used to send a waveform that compensates for the geometry of the outer surface of the skull. To evaluate this technique, a FEM model was used to simulate ultrasonic wave propagation through an irregular surface and SAUL technique was applied in FEM. The main goal of the FEM simulation was to compare the transmitted energy levels of the waveform for a plane wave and a surface compensated wave. Results showed an overall 65% of improvement at a 0^o incidence angle and a 15% improvement when the ultrasonic probe is tilted 10^o relative to the surface. The results obtained from the FEM laid a proof of concept for the experiments. The experiment was performed using bone phantom samples with irregular surfaces that mimicked the acoustical properties of the real temporal bone. The experiments were performed in two parts. Part-A comprised of A-scan comparisons between compensated and uncompensated plane waves. The results from part-A showed that compensated plane waves had higher transmitted energies compared to uncompensated plane waves. Part-B was done using B-scans comparison. Part-B experiments suggested an overall 10 dB -15 dB of improvement in transcranial B-scan images. These are very promising results for TCD imaging, which generally suffers from poor transmission.

CONCLUSION AND RECOMMENDATIONS

Cerebrovascular activity monitoring is important in clinical care. TCD is a non-invasive method that measures blood FV in the arteries inside the brain. The blood FV measurement can help in a variety of diagnostic cerebrovascular applications. Although TCD sonography provides several advantages as compared to other modalities (e.g. safety, less cost, portability), the acceptance of the TCD method in detecting conventional problems like vasospasm has been limited. Detecting vasospasm requires blood flow rate, and for that, it is required to accurately determine the diameter of the blood vessel. Predicting the diameter of the blood vessel requires high-quality imaging. One of the reasons why TCD fails to record the blood flow rate is due to the insufficient transmission of energy into the brain; the blood vessels are not visible in the majority of the patients. This thesis focused on increasing the transmitted energy into the brain. In this study, firstly an analytical model was developed which provided a 2D map of transmitted energies as a function of frequency, skin, and bone thickness. This 2D map demonstrated the effect of the acoustic impedance mismatch effect due to the bone-soft tissue interface. This analytical model was validated with an experimental setup suggesting that choosing the right frequency will increase the chances of a successful measurement. The analytical and experimental results were strongly correlated. A first journal paper was accepted in December, 2020 in IEEE Transactions on Ultrasonics, Ferroelectrics and Frequency Control.

Once it was established how transmitted energy plays a role as a function of skin and bone thicknesses, Doppler experiments were performed to prove the concept. It was shown in this chapter that choosing the optimal frequency from the 2D map developed in chapter 3 helps in a successful measurement of blood mimicking fluid flow due to a higher SNR. But there were some combinations of frequency and water layer thickness for which it was not possible to measure the flow due to low SNR. Furthermore, experiments were conducted to measure blood mimicking fluid flow rates. This work showed that flow rates were successfully calculated across five experiments. Though flow rates were overestimated by a factor of 7 they showed consistency. It was discovered that diameter overestimation was causing this, since calculated blood FV were within 5% of the theoretical blood FV.

The last chapter was about solving the problem of transmission energy losses due to the irregular outer surface of the bone. To accomplish this task, the FE solver was used in the evaluation and refinement of creating a plane wave beyond the outer surface of the skull. Although FE solver did not provide an exact match of noise effects, inhomogeneities present in the real skull, it was useful in validating the proof of concept and comparing performance metrics - especially using simplified assumptions. For the experiments, five temporal bone phantoms with different thicknesses, curvatures, and attenuations were used. Using the approach described above firstly an optimal frequency was chosen for the maximum energy transmission. Once the optimal frequency was obtained, the surface profile of the bone phantom was calculated by setting the distance between the probe and the bone phantom to 1 cm. The surface profiling was calculated according to SAUL. A surface compensated wavefront could then be transmitted. For the comparison, two kinds of results were used, one comparing the amplitudes of the signal without the compensated ultrasonic waves and the surface compensated ultrasonic waves. Secondly, B-scan images using multiple plane waves were reconstructed. Results showed a gain of 10-15 dB when using a surface compensated wave.

So overall, it can be concluded that the acoustic impedance mismatch combined with surface compensation of ultrasonic waves presents a novel procedure to increase the chances of a successful Doppler measurement from a TCD system.

It is highly recommended to perform an acoustic impedance mismatch study considering a more complex analytical model, which involves multiple layers of bone and a scalp tissue layer to include more attenuation effects. Doing this will help in understanding the overall effects of these layers on the choice of frequency. Furthermore, to perform the Doppler experiments for irregular bone surfaces is also recommended. The experiments should not only include acoustic impedance mismatch but also surface compensated US using the SAUL method discussed in chapter 5. An improvement in TCD imaging quality is anticipated when applying both the aforementioned techniques together.

Finally, an in-vivo study involving a large number of samples with varying bone thicknesses is also recommended. This would give a solid demonstration of clinical viability for the findings in this work.

REFERENCES

Aarnio, J., Clement, G. T. & Hynynen, K. (2005). A new ultrasound method for determining the acoustic phase shifts caused by the skull bone. *Ultrasound in Medicine & Biology*, 31(6), 771–780. doi: 10.1016/j.ultrasmedbio.2005.01.019.

Aaslid, R. (1986). The Doppler Principle Applied to Measurement of Blood Flow Velocity in Cerebral Arteries. In Aaslid, R. (Ed.), *Transcranial Doppler Sonography* (pp. 22–38). Vienna: Springer. doi: 10.1007/978-3-7091-8864-4_3.

Alder, H. C. (2002). Safe Medical Devices Act: management guidance for hospital compliance with the new FDA requirements. *Hospital technology series*, 12, 1-2. doi: 10.1016/S0377-1237(02)80001-6.

Alexandrov, A. V., Brodie, D. S., McLean, A., Hamilton, P., Murphy, J. & Burns, P. N. (1997). Correlation of peak systolic velocity and angiographic measurement of carotid stenosis revisited. *Stroke*, 28(2), 339–342.

Alvarez-Arenas, T. (2004). Acoustic impedance matching of piezoelectric transducers to the air. *IEEE Transactions on Ultrasonics, Ferroelectrics and Frequency Control*, 51(5), 624–633. doi: 10.1109/TUFFC.2004.1320834.

Aubry, J. F., Tanter, M., Pernot, M., Thomas, J. L. & Fink, M. (2003). Experimental demonstration of noninvasive transskull adaptive focusing based on prior computed tomography scans. *The Journal of the Acoustical Society of America*, 113(1), 84–93. doi: 10.1121/1.1529663.

Baradarani, A., Sadler, J., Taylor, J. & Maev, R. (2014). High-resolution blood flow imaging through the skull. *2014 IEEE International Ultrasonics Symposium*, pp. 444–447. doi: 10.1109/ULTSYM.2014.0110.

Bathala, L., Mehndiratta, M. & Sharma, V. (2013). Transcranial doppler: Technique and common findings (Part 1). *Annals of Indian Academy of Neurology*, 16(2), 174. doi: 10.4103/0972-2327.112460.

Baumgartner, R., Arnold, M., Gonner, F., Staikow, I., Herrmann, C. & Rivoir,A.and Muri, R. (1997). Contrast-Enhanced Transcranial Color-Coded Duplex Sonography in Ischemic Cerebrovascular Disease. *Stroke*, 28(12), 2473–2478. doi: 10.1161/01.STR.28.12.2473.

Bercoff, J., Montaldo, G., Loupas, T., Savery, D., Mézière, F., Fink, M. & Tanter, M. (2011). Ultrafast compound doppler imaging: providing full blood flow characterization. *IEEE Transactions on Ultrasonics, Ferroelectrics and Frequency Control*, 58(1), 134–147. doi: 10.1109/TUFFC.2011.1780.

Besson, A., Zhang, M., Varray, F., Liebgott, H., Friboulet, D., Wiaux, Y., Thiran, J., Carrillo, R. & Bernard, O. (2016). A Sparse Reconstruction Framework for Fourier-Based Plane-Wave Imaging. *IEEE Transactions on Ultrasonics, Ferroelectrics, and Frequency Control*, 63(12), 2092-2106.

Bishop, C., Powell, S., Rutt, D. & Browse, N. (1986). Transcranial Doppler measurement of middle cerebral artery blood flow velocity: a validation study. *Stroke*, 17(5), 913–915.

Blackstock, D. T. (2000). *Fundamentals of physical acoustics*. New York: Wiley.

Blanco, P. & Abdo-Cuza, A. (2018a). Transcranial Doppler ultrasound in neurocritical care. *Journal of Ultrasound*, 21(1), 1–16. doi: 10.1007/s40477-018-0282-9.

Blanco, P. & Abdo-Cuza, A. (2018b). Transcranial Doppler ultrasound in neurocritical care. *Journal of Ultrasound*, 21(1), 1–16. doi: 10.1007/s40477-018-0282-9.

Chang, C., Cho, Y., Wang, L. & Zou, J. (2013). Micromachined silicon acoustic delay lines for ultrasound applications. *Journal of Micromechanics and Microengineering*, 23(2), 025006. doi: 10.1088/0960-1317/23/2/025006.

Chaves, J. (2008). *Introduction to nonimaging optics*. Boca Raton: CRC Press.

Cheeke, J. D. N. (2002). *Fundamentals and Application of ultrasonic waves*. CRC series in pure and applied physics.

Clement, G. & Hynynen, K. (2002). Correlation of ultrasound phase with physical skull properties. *Ultrasound in Medicine & Biology*, 28(5), 617–624. doi: 10.1016/S0301-5629(02)00503-3.

Connor, C., Clement, G. & Hynynen, K. (2002). A unified model for the speed of sound in cranial bone based on genetic algorithm optimization. *Physics in Medicine and Biology*, 47(22), 3925–3944. doi: 10.1088/0031-9155/47/22/302.

Couade, M. (2016). The advent of ultrafast ultrasound in vascular imaging: a review. *Journal of Vascular Diagnostics and Interventions*, 9. doi: 10.2147/JVD.S68045.

Couture, O., Fink, M. & Tanter, M. (2012). Ultrasound contrast plane wave imaging. *IEEE Transactions on Ultrasonics, Ferroelectrics, and Frequency Control*, 59(12), 2676-2683.

Donkor, E. S. (2018). Stroke in the 21st Century: A Snapshot of the Burden, Epidemiology, and Quality of Life. *Stroke Research and Treatment*, 2018, 1–10. doi: 10.1155/2018/3238165.

Doppler, C. (1842). *Ueber das farbige Licht der Doppelsterne und einiger anderer Gestirne des Himmels: Versuch einer das Bradley'sche Aberrations-Theorem als integrirenden Theil in sich schliessenden allgemeineren Theorie*. In Commission bei Borrosch & André.

Egghe, L. & Leydesdorff, L. (2009). The relation between Pearson's correlation coefficient *r* and Salton's cosine measure. *Journal of the American Society for Information Science and Technology*, 60(5), 1027–1036. doi: 10.1002/asi.21009.

Errico, C., Osmanski, B., Pezet, S., Couture, O., Lenkei, Z. & Tanter, M. (2016). Transcranial functional ultrasound imaging of the brain using microbubble-enhanced ultrasensitive Doppler. *NeuroImage*, 124, 752–761. doi: 10.1016/j.neuroimage.2015.09.037.

Fink, M. (1992). Time reversal of ultrasonic fields. I. Basic principles. *IEEE Transactions on Ultrasonics, Ferroelectrics and Frequency Control*, 39(5), 555–566. doi: 10.1109/58.156174.

Flax, S. & O'Donnell, M. (1988). Phase-aberration correction using signals from point reflectors and diffuse scatterers: basic principles. *IEEE Transactions on Ultrasonics, Ferroelectrics and Frequency Control*, 35(6), 758–767. doi: 10.1109/58.9333.

Fry, F. J. & Barger, J. E. (1978). Acoustical properties of the human skull. *The Journal of the Acoustical Society of America*, 63(5), 1576–1590. doi: 10.1121/1.381852.

Gahn, G., Gerber, J., Hallmeyer, S., Hahn, G., Ackerman, R. H., Reichmann, H. & von Kummer, R. (2000). Contrast-enhanced transcranial color-coded duplexsonography in stroke patients with limited bone windows. *AJNR. American journal of neuroradiology*, 21(3), 509–514.

Gauss, R. C., Trahey, G. E. & Soo, M. S. (2001). Wavefront estimation in the human breast. pp. 172–181. doi: 10.1117/12.428194.

Girault, J., Kouame, D., Ouahabi, A. & Patat, F. (2000). Micro-emboli detection: an ultrasound Doppler signal processing viewpoint. *IEEE Transactions on Biomedical Engineering*, 47(11), 1431-1439.

Glassner, A. (1989). *An Introduction to ray tracing*. Consulted at http://ebookcentral.proquest .com/lib/upf/detail.action?docID=4386913.

Gupta, S., Haiat, G., Laporte, C. & Belanger, P. (2020). *Effect of acoustic impedance mismatch as a function of frequency in transcranial ultrasound*. Manuscript submitted for publication.

Hashimoto, H., Etani, H., Naka, M., Kinoshita, N. & Nukada, T. (1992). Assessment of the Rate of Successful Transcranial Doppler Recording Trhough the Temporal Windows in Japanese with Special Reference to Aging and Sex. *Nippon Ronen Igakkai Zasshi*.

Japanese Journal of Geriatrics, 29(2), 119–122. doi: 10.3143/geriatrics.29.119.

Haworth, K. J., Fowlkes, J. B., Carson, P. L. & Kripfgans, O. D. (2008). Towards Aberration Correction of Transcranial Ultrasound Using Acoustic Droplet Vaporization. *Ultrasound in Medicine & Biology*, 34(3), 435–445. doi: 10.1016/j.ultrasmedbio.2007.08.004.

Hesselstrand, R., Scheja, A., Wildt, M. & Akesson, A. (2008). High-frequency ultrasound of skin involvement in systemic sclerosis reflects oedema, extension and severity in early disease. *Rheumatology*, 47(1), 84–87. doi: 10.1093/rheumatology/kem307.

Hill, R. & El-Dardiry, S. (1980). A theory for optimization in the use of acoustic emission transducers. *The Journal of the Acoustical Society of America*, 67(2), 673–682. doi: 10.1121/1.383893.

Hoksbergen, A. W. J., Legemate, D. A., Ubbink, D. T. & Jacobs, M. J. H. M. (1999). Success Rate of Transcranial Color-Coded Duplex Ultrasonography in Visualizing the Basal Cerebral Arteries in Vascular Patients Over 60 Years of Age. *Stroke*, 30(7), 1450–1455. doi: 10.1161/01.STR.30.7.1450.

Hopkins, D. L., Brassard, M., Neau, G. A., Noiret, J.-N., Johnson, W. V. & Le Ber, L. (2013). Surface-Adaptive Ultrasound (SAUL) for phased-array inspection of composite specimens with curved edges and complex geometry. pp. 809–816. doi: 10.1063/1.4789128.

Hoskins, P. R., Martin, K. & Thrush, A. (Eds.). (2010). *Diagnostic ultrasound: physics and equipment* (ed. 2nd ed). Cambridge, UK ; New York: Cambridge University Press.

Huthwaite, P. (2014). Accelerated finite element elastodynamic simulations using the GPU. *Journal of Computational Physics*, 257, 687–707. doi: 10.1016/j.jcp.2013.10.017.

Jensen, J. A. (1996). *Estimation of blood velocities using ultrasound: a signal processing approach* (ed. 1). New York, NY: Cambridge University Press.

Jones,R.and O'Reilly, M. & Hynynen, K. (2013). Transcranial passive acoustic mapping with hemispherical sparse arrays using CT-based skull-specific aberration corrections: a simulation study. *Physics in Medicine and Biology*, 58(14), 4981–5005. doi: 10.1088/0031-9155/58/14/4981.

Kasai, C., Namekawa, K., Koyano, A. & Omoto, R. (1985). Real-Time Two-Dimensional Blood Flow Imaging Using an Autocorrelation Technique. *IEEE Transactions on Sonics and Ultrasonics*, 32(3), 458–464. doi: 10.1109/T-SU.1985.31615.

Khalitov, R. S., Gurbatov, S. N. & Demin, I. Y. (2016). The use of the Verasonics ultrasound system to measure shear wave velocities in CIRS phantoms. *Physics of Wave Phenomena*, 24(1), 73–76. doi: 10.3103/S1541308X16010143.

Klötzsch, C., Popescu, O. & Berlit, P. (1998). A new 1-MHz probe for transcranial Doppler sonography in patients with inadequate temporal bone windows. *Ultrasound in Medicine & Biology*, 24(1), 101–103. doi: 10.1016/S0301-5629(97)00231-7.

Kohama, M., Sugiyama, S., Sato, K., Endo, H., Niizuma, K., Endo, T., Ohta, M., Matsumoto, Y., Fujimura, M. & Tominaga, T. (2016). Difference in Transcranial Doppler Velocity and Patient Age between Proximal and Distal Middle Cerebral Artery Vasospasms after Aneurysmal Subarachnoid Hemorrhage. *Cerebrovascular Diseases Extra*, 6(2), 32–39. doi: 10.1159/000447330.

Kollár, J., Schulte-Altedorneburg, G., Sikula, J., Fülesdi, B., Ringelstein, E. B., Mehta, V., Csiba, L. & Droste, D. (2004). Image Quality of the Temporal Bone Window Examined by Transcranial Doppler Sonography and Correlation with Postmortem Computed Tomography Measurements. *Cerebrovascular Diseases*, 17(1), 61–65. doi: 10.1159/000073899.

Krautkrämer, J. & Krautkrämer, H. (1990). *Ultrasonic Testing of Materials*. Berlin, Heidelberg: Springer Berlin Heidelberg. doi: 10.1007/978-3-662-10680-8.

Krejza, J., Swiat, M., Pawlak, M., Oszkinis, G., Weigele, J., Hurst, R. & Kasner, S. (2007). Suitability of Temporal Bone Acoustic Window: Conventional TCD Versus Transcranial Color-Coded Duplex Sonography. *Journal of Neuroimaging*, 17(4), 311–314. doi: 10.1111/j.1552-6569.2007.00117.x.

Krimholtz, R., Leedom, D. & Matthaei, G. (1970). New equivalent circuits for elementary piezoelectric transducers. *Electronics Letters*, 6(13), 398. doi: 10.1049/el:19700280.

Kwon, J., Kim, J., Kang, D., Bae, K. & Kwon, S. (2006). The Thickness and Texture of Temporal Bone in Brain CT Predict Acoustic Window Failure of Transcranial Doppler. *Journal of Neuroimaging*, 16(4), 347–352. doi: 10.1111/j.1552-6569.2006.00064.x.

Le Jeune, L., Robert, S., Lopez Villaverde, E. & Prada, C. (2016). Plane Wave Imaging for ultrasonic non-destructive testing: Generalization to multimodal imaging. *Ultrasonics*, 64, 128–138. doi: 10.1016/j.ultras.2015.08.008.

Lindsey, B. D., Light, E. D., Nicoletto, H. A., Bennett, E. R., Laskowitz, D. T. & Smith, S. W. (2011). The ultrasound brain helmet: new transducers and volume registration for in vivo simultaneous multi-transducer 3-D transcranial imaging. *IEEE Transactions on Ultrasonics, Ferroelectrics and Frequency Control*, 58(6), 1189–1202. doi: 10.1109/TUFFC.2011.1929.

Lindsey, B. D., Nicoletto, H. A., Bennett, E. R., Laskowitz, D. T. & Smith, S. W. (2013). Simultaneous Bilateral Real-Time 3-D Transcranial Ultrasound Imaging at 1 MHz

Through Poor Acoustic Windows. *Ultrasound in Medicine & Biology*, 39(4), 721–734. doi: 10.1016/j.ultrasmedbio.2012.11.019.

Liu, D. & Waag, R. (1994). Time-shift compensation of ultrasonic pulse focus degradation using least-mean-square error estimates of arrival time. *The Journal of the Acoustical Society of America*, 95(1), 542–555. doi: 10.1121/1.408348.

Ludwig, G. D. (1950). The Velocity of Sound through Tissues and the Acoustic Impedance of Tissues. *The Journal of the Acoustical Society of America*, 22(6), 862–866. doi: 10.1121/1.1906706.

Ludwig, R. & Levin, P. L. (1995). Analytical and numerical treatment of pulsed wave propagation into a viscous fluid. *IEEE Transactions on Ultrasonics, Ferroelectrics, and Frequency Control*, 42(4), 789-792.

Mahindra, H. & Murty, O. (2009). Variability in thickness of human skull bones and sternum – an autopsy experience. *Variability in thickness of human skull bones and sternum – an autopsy experience*, 26(2), 26-31.

Major, G., Fugate, M., Devlin, T. & Hutson, R. (2011). Use of CT Angiography and CT Perfusion Imaging in the Selection of Hyperacute Stroke Patients to Undergo Emergent Carotid Endarterectomy Versus Intra-Cranial Thrombectomy. *Journal of Vascular Surgery*, 54(6), 1860–1861. doi: 10.1016/j.jvs.2011.10.060.

Mansour, O., Poepping, T. L. & Lacefield, J. C. (2016). A beamforming method for plane wave Doppler imaging of high flow velocities. pp. 9. doi: 10.1117/12.2217226.

Marinoni, M., Ginanneschi, A., Forleo, P. & Amaducci, L. (1997). Technical limits in transcranial Doppler recording: Inadquate acoustic windows. *Ultrasound in Medicine & Biology*, 23(8), 1275–1277. doi: 10.1016/S0301-5629(97)00077-X.

Mickael Brice, D. (2008). *Efficient finite element modelling of ultrasound waves in elastic media*. (Ph.D. thesis, Imperial College London). Consulted at http://hdl.handle.net/10044/1/7974.

Montaldo, G., Tanter, M., Bercoff, J., Benech, N. & Fink, M. (2009). Coherent plane-wave compounding for very high frame rate ultrasonography and transient elastography. *IEEE Transactions on Ultrasonics, Ferroelectrics and Frequency Control*, 56(3), 489–506. doi: 10.1109/TUFFC.2009.1067.

Moorthy, R. S. (1993). DOPPLER ULTRASOUND. *Medical journal, Armed Forces India*, 58, 1-27. doi: 10.1016/S0377-1237(02)80001-6.

Papadacci, C., Pernot, M., Couade, M., Fink, M. & Tanter, M. (2014). High-contrast ultrafast imaging of the heart. *IEEE Transactions on Ultrasonics, Ferroelectrics, and Frequency Control*, 61(2), 288–301. doi: 10.1109/TUFFC.2014.6722614.

Pernot, M., Montaldo, G., Tanter, M. & Fink, M. (2006). "Ultrasonic stars" for time-reversal focusing using induced cavitation bubbles. *Applied Physics Letters*, 88(3), 034102. doi: 10.1063/1.2162700.

Pietrangelo, S. J. (2013). *An electronically steered, wearable transcranial Doppler ultrasound system*. (Master's thesis, Massachusetts Institute of Technology).

Postert, T., Federlein, J., Przuntek, H. & Büttner, T. (1997). Insufficient and absent acoustic temporal bone window: Potential and limitations of transcranial contrast-enhanced color-coded sonography and contrast-enhanced power-based sonography. *Ultrasound in Medicine & Biology*, 23(6), 857–862. doi: 10.1016/S0301-5629(97)00047-1.

Pulkkinen, A., Huang, Y., Song, J. & Hynynen, K. (2011). Simulations and measurements of transcranial low-frequency ultrasound therapy: skull-base heating and effective area of treatment. *Physics in Medicine and Biology*, 56(15), 4661–4683. doi: 10.1088/0031-9155/56/15/003.

Purkayastha, S. & Sorond, F. (2013a). Transcranial Doppler Ultrasound: Technique and Application. *Seminars in Neurology*, 32(04), 411–420. doi: 10.1055/s-0032-1331812.

Purkayastha, S. & Sorond, F. (2013b). Transcranial Doppler Ultrasound: Technique and Application. *Seminars in Neurology*, 32(04), 411–420. doi: 10.1055/s-0032-1331812.

Rajagopal, P. & Lowe, M. J. S. (2007). Short range scattering of the fundamental shear horizontal guided wave mode normally incident at a through-thickness crack in an isotropic plate. *Journal of the Acoustical Society of America*, 122(3), 1527-1538.

Randall, R. H. (2012). *Introduction to Acoustics.* [English]. Consulted at http://www.myilibrary.com?id=570456.

Robert, S., Casula, O., Roy, O. & Neau, G. (2012). Real time nondestrutive testing of composite aeronautical structures with a self-adaptive ultrasonic technique. *2012 IEEE International Conference on Imaging Systems and Techniques Proceedings*, pp. 207-212.

Robins, T., Leow, C., Chapuis, G., Chadderton, P. & Tang, M. (2017). Dual frequency transcranial ultrasound for contrast enhanced ultrafast brain functional imaging. *2017 IEEE International Ultrasonics Symposium (IUS)*, pp. 1-4.

Sadler, J., Ahmed, Z., Shapoori, K., Wydra, A., Malyarenko, E., Maeva, E. & Maev, R. G. (2013). Development of a method to image blood flow beneath the skull or tissue using ultrasonic speckle reflections. *SPIE Medical Imaging*, pp. 86720G. doi: 10.1117/12.2002104.

Sandrin, L., Catheline, S., Tanter, M., Hennequin, X. & Fink, M. (1999). Time-Resolved Pulsed Elastography with Ultrafast Ultrasonic Imaging. *Ultrasonic Imaging*, 21(4), 259–272. doi: 10.1177/016173469902100402.

Sarkar, S., Ghosh, S., Ghosh, S. K. & Collier, A. (2007). Role of transcranial Doppler ultrasonography in stroke. *Postgraduate Medical Journal*, 83(985), 683–689. doi: 10.1136/pgmj.2007.058602.

Seidel, G., Kaps, M. & Gerriets, T. (1995). Potential and Limitations of Transcranial Color-Coded Sonography in Stroke Patients. *Stroke*, 26(11), 2061–2066. doi: 10.1161/01.STR.26.11.2061.

Seidenari, S. & Giovanni, P. (1999). Variations in Facial Skin Thickness and Echogenicity with Site and Age. *Acta Dermato-Venereologica*, 79(5), 366–369. doi: 10.1080/000155599750010283.

Shankar, H. & Pagel, P. S. (2011). Potential Adverse Ultrasound-related Biological Effects: A Critical Review. *Anesthesiology*, 115(5), 1109–1124. doi: 10.1097/ALN.0b013e31822fd1f1.

Shung, K. & Zippuro, M. (1996). Ultrasonic transducers and arrays. *IEEE Engineering in Medicine and Biology Magazine*, 15(6), 20–30. doi: 10.1109/51.544509.

Smith, W. S., Roberts, H. C., Chuang, N. A., Ong, K. C., Lee, T. J., Johnston, S. C. & Dillon, W. P. (2003). Safety and feasibility of a CT protocol for acute stroke: combined CT, CT angiography, and CT perfusion imaging in 53 consecutive patients. *AJNR. American journal of neuroradiology*, 24(4), 688–690.

Szabo, T. L. (1995). Causal theories and data for acoustic attenuation obeying a frequency power law. *The Journal of the Acoustical Society of America*, 97(1), 14–24. doi: 10.1121/1.412332.

Tanter, M. & Fink, M. (2014). Ultrafast imaging in biomedical ultrasound. *IEEE Transactions on Ultrasonics, Ferroelectrics, and Frequency Control*, 61(1), 102–119. doi: 10.1109/TUFFC.2014.2882.

Thomas, D. (2017). A Novel Device for Pre-CT Assessment of LVOs: Initial Results from the EXPEDITE Study. *SVIN*.

Thomas, L. & Hall, A. (1994). An improved wall filter for flow imaging of low velocity flow. *1994 Proceedings of IEEE Ultrasonics Symposium*, 3, 1701–1704 vol.3. doi: 10.1109/ULT-

SYM.1994.401918.

Tiran, E., Deffieux, T., Correia, M., Maresca, D., Osmanski, B., Sieu, L., Bergel, A., Cohen, I., Pernot, M. & Tanter, M. (2015). Multiplane wave imaging increases signal-to-noise ratio in ultrafast ultrasound imaging. *Physics in Medicine and Biology*, 60(21), 8549–8566. doi: 10.1088/0031-9155/60/21/8549.

Tong, L., Gao, H., Choi, H. & D'hooge, J. (2012). Comparison of conventional parallel beamforming with plane wave and diverging wave imaging for cardiac applications: a simulation study. *IEEE Transactions on Ultrasonics, Ferroelectrics, and Frequency Control*, 59(8), 1654-1663.

Tretbar, S., Plinkert, P. & Federspil, P. (2009a). Accuracy of Ultrasound Measurements for Skull Bone Thickness Using Coded Signals. *IEEE Transactions on Biomedical Engineering*, 56(3), 733–740. doi: 10.1109/TBME.2008.2011058.

Tretbar, S., Plinkert, P. & Federspil, P. (2009b). Accuracy of Ultrasound Measurements for Skull Bone Thickness Using Coded Signals. *IEEE Transactions on Biomedical Engineering*, 56(3), 733–740. doi: 10.1109/TBME.2008.2011058.

U. Lok,P. Song, J. D. T. R. D. E. A. B. C. H. P. G. S. T. W. L. & Chen, S. (2020). Real time SVD-based clutter filtering using randomized singular value decomposition and spatial downsampling for micro-vessel imaging on a Verasonics ultrasound system. *Ultrasonics*, 107, 106163. doi: https://doi.org/10.1016/j.ultras.2020.106163.

Udesen, J., Gran, F., Hansen, K., Jensen, J., Thomsen, C. & Nielsen, M. (2008). High frame-rate blood vector velocity imaging using plane waves: Simulations and preliminary experiments. *IEEE Transactions on Ultrasonics, Ferroelectrics and Frequency Control*, 55(8), 1729–1743. doi: 10.1109/TUFFC.2008.858.

Ultrasound, S. V. (2012). Transcranial Doppler (TCD) Ultrasound Imaging [html].

Venkatesh, B., Shen, Q. & Lipman, J. (2002). Continuous measurement of cerebral blood flow velocity using transcranial Doppler reveals significant moment-to-moment variability of data in healthy volunteers and in patients with subarachnoid hemorrhage*:. *Critical Care Medicine*, 30(3), 563–569. doi: 10.1097/00003246-200203000-00011.

Webb, S. (1993). *The physics of medical imaging*. Bristol; Philadelphia: Institute of Physics Pub.

White, D. (1992). The early development of neurosonology: I. echoencephalography in adults. *Ultrasound in Medicine & Biology*, 18(2), 115–165. doi: 10.1016/0301-5629(92)90126-U.

White, H. & Venkatesh, B. (2006). Applications of transcranial Doppler in the ICU: a review. *Intensive Care Medicine*, 32(7), 981–994. doi: 10.1007/s00134-006-0173-y.

White, P. J., Clement, G. T. & Hynynen, K. (2006a). Local frequency dependence in transcranial ultrasound transmission. *Physics in Medicine and Biology*, 51(9), 2293–2305. doi: 10.1088/0031-9155/51/9/013.

White, P., Clement, G. & Hynynen, K. (2006b). Longitudinal and shear mode ultrasound propagation in human skull bone. *Ultrasound in Medicine & Biology*, 32(7), 1085–1096. doi: 10.1016/j.ultrasmedbio.2006.03.015.

Wijnhoud, A., Franckena, M., van der Lugt,A., P. J. & Dippel, D. (2008). Inadequate Acoustical Temporal Bone Window in Patients with a Transient Ischemic Attack or Minor Stroke: Role of Skull Thickness and Bone Density. *Ultrasound in Medicine & Biology*, 34(6), 923–929. doi: 10.1016/j.ultrasmedbio.2007.11.022.

Wydra, A. & Maev, R. G. (2013). A novel composite material specifically developed for ultrasound bone phantoms: cortical, trabecular and skull. *Physics in Medicine and Biology*, 58(22), N303–N319. doi: 10.1088/0031-9155/58/22/N303.

Yiu, B. Y. & Yu, A. C. (2013). High-Frame-Rate Ultrasound Color-Encoded Speckle Imaging of Complex Flow Dynamics. *Ultrasound in Medicine & Biology*, 39(6), 1015–1025. doi: 10.1016/j.ultrasmedbio.2012.12.016.

Yousefi, A., Goertz, D. E. & Hynynen, K. (2009). Transcranial Shear-Mode Ultrasound: Assessment of Imaging Performance and Excitation Techniques. *IEEE Transactions on Medical Imaging*, 28(5), 763-774.

Yue, Q., Liu, D., Wang, W., Di, W., Lin, D., Wang, X. & Luo, H. (2014). Fabrication of a PMN-PT Single Crystal-Based Transcranial Doppler Transducer and the Power Regulation of Its Detection System. *Sensors*, 14(12), 24462–24471. doi: 10.3390/s141224462.